HELSINKI INSTITUTE OF PHYSICS

INTERNAL REPORT
HIP - 2002 - 03

A Silicon Detector for Neutrino Physics

Jukka Kokkonen

CERN, EP Division
CH-1211 Geneva, Switzerland
and
Helsinki Institute of Physics
P.O. Box 64, FIN-00014 University of Helsinki, Finland

Dissertation for the degree of Doctor of Science in Technology to be presented with due permission of the Department of Engineering Physics and Mathematics for public examination and debate in Auditorium F1 at Helsinki University of Technology (Espoo, Finland) on the 17th of May, 2002, at 12 o'clock noon.

Helsinki 2002

ISBN 951-45-8937-8
ISSN 1455-0563
Helsinki University Press 2002

Abstract

In order to demonstrate the feasibility of conducting future $\nu_\mu \rightarrow \nu_\tau$ oscillation searches using a high-resolution, large-area silicon microstrip detector, the Silicon TARget (STAR) detector was built. STAR was installed in the NOMAD short baseline neutrino oscillation experiment at the CERN SPS neutrino beam, where it recorded approximately 10 000 neutrino interactions during the operation of the detector in the period 1997–98. It consists of five layers of silicon detectors interleaved with four layers of passive boron carbide as the target. The target mass is 45 kg, while the total silicon surface area is 1.14 m^2 and contains 32 000 readout channels. The individual modules have a length of 72 cm, the longest built to date.

The detection of τ particles, produced in ν_τ charged-current interactions, would require a tracking detector with a precision of a few tens of microns in order to measure the position of the neutrino interaction vertex as well as the impact parameter of the τ decay products. The performance of STAR was studied by reconstructing the decays of K^0_S mesons produced in ν_μ charged-current interactions.

For both the primary and secondary vertices, the resolution in the y direction was found to be approximately 20 μm, while that in the z direction was found to be approximately 100 μm. The double vertex resolution, a measure of how accurately the distance between the vertices can be measured, was found to be approximately 20 μm in the y direction and 300 μm in the z direction. The impact parameter resolution of the muons resulting from ν_μ charged-current interactions, with respect to the primary vertex, was found to be 25 μm.

The vertex resolution and impact parameter results show that a microstrip silicon detector would be well-suited to measuring $\nu_\mu \rightarrow \nu_\tau$ oscillations. The high precision of silicon detectors has several other applications within neutrino physics, such as using a silicon detector as the near-detector in a future neutrino factory facility.

Acknowledgements

This work was carried out at CERN, the European Laboratory for Particle Physics, in Geneva, Switzerland, over a period of five years from 1997 to 2002 within the CERN Doctoral Student Programme, with extensive support from the Helsinki Institute of Physics (HIP). The Helsinki University of Technology (HUT) has provided supervision for this doctoral work. The majority of the research has been carried out within the NOMAD neutrino oscillation experiment on the STAR silicon detector.

I am most grateful to Lucie Linssen for taking me on-board at CERN, for supervising my work and for constant support. Leslie Camilleri, the leader of the CERN group at NOMAD, is thanked for all his help, in particular for the work concerning K^0_S decays. At HUT, I am indebted to my supervising professor, Martti M. Salomaa, who has been of great assistance in the final stages of the work. I would also like to thank Jan Westerholm for his encouragement and for taking on the role of supervising professor at earlier stages.

I am grateful to several people at HIP. In particular Jorma Tuominiemi's pertinent interest in my work and the long discussions have been significant. The support received from the present director of the Institute, Dan-Olof Riska, and the former director, Eero Byckling, is gratefully acknowledged.

Within the STAR project, I would like to thank Eduardo do Couto e Silva for his enthusiasm and optimism and also for convincing me to join the team. Those early days working in the laboratory with him and Anselmo Cervera-Villanueva, to whom my thanks are also extended, were truly memorable.

I am grateful to Paul Soler for great help and much encouragement. He was, in many ways, a second supervisor of my work. Juan-Jose Gomez-Cadenas, the leader of the STAR project, is thanked for his driven, yet easy-going manner and for making things happen.

Particular thanks go to Malcolm "Event" Ellis for his friendship and assistance. We have worked together intensively nearly since the beginning and several have been the phone calls between CERN and Sydney University, not to mention the e-mails. Thanks also to Valentin Kouznetsov for his friendship and help. It was also a pleasure to have him as my officemate!

I want to express my gratitude also to Didier Ferrère and Gabriel Vidal-Sitjes, also officemates and members of the STAR team, as well as to Ögmundur Runolfsson who made me feel very welcome in the silicon laboratory, which was run by him. I am also grateful to the many other people contributing to STAR, including Dirk Geppert, Sylvie Geppert Soulie, Michel Gouanère, Werner Huta, Bohdan Lisowski, José Mulon, Burkhard Schmidt, Mikael Smedbäck, and David Steele.

I would like to thank at least the following people for extensive discussions on particle physics and thus improving my understanding of the topic: Andrew Godley (who is also thanked for his snappy manner!), Ari Kiiskinen and Dmitry Naumov.

Financial support from the CERN Doctoral Student Programme, the Helsinki Institute of Physics, the Academy of Finland, the CERN group at NOMAD, the Magnus Ehrnrooth Foundation, the Foundation for the Commercial and Technical Sciences (KAUTE) and the Waldemar von Frenckell Foundation is duly acknowledged. All the sources mentioned, with the exception of the ones from CERN, are from Finland.

I am also indebted to my friends in the Geneva region, Finland, and also elsewhere for their encouragement and for occasionally helping me to take my mind off my work. There was the initial Finnish "taskforce" at CERN in 1997–98, with whom I have shared many memorable moments. But there were many others too, a more international group in the later years, all of whom I would like to thank for their friendship.

Finally, I would like to thank my parents, Ritva and Olli, and my brother Tatu, for their encouragement and support throughout the years.

List of Publications

This dissertation is a review of the author's work in the field of particle detection in high-energy physics. It consists of an overview and the following selection of the author's publications in this field:

I *Performance of Long Modules of Silicon Microstrip Detectors*, J. Kokkonen in G. Baricchello *et al.*, Nuclear Instruments and Methods Phys. Res. A 413 (1998) 17-30.

II *A B_4C-Silicon Target for the Detection of Neutrino Interactions*, J. Kokkonen in G. Baricchello *et al.*, Nuclear Instruments and Methods Phys. Res. A 419 (1998) 1-15.

III *Kalman Filter Tracking and Vertexing in a Silicon Detector for Neutrino Physics*, J. Kokkonen in A. Cervera-Villanueva *et al.*, CERN-EP/2001-092 (2001). Accepted for publication in Nuclear Instruments and Methods Phys. Res. A.

IV *STAR Noise and Hit-Finding Efficiency*, J. Kokkonen, F.J.P. Soler, G. Vidal-Sitjes, Helsinki University of Technology Report HUT-F-A812, ISBN 951-22-5843-9, ISSN 1456-3320 (2002). [1]

V *Observation of K^0_S Decays in the NOMAD Silicon TARget (STAR) Detector*, J. Kokkonen, Helsinki Institute of Physics Internal Report HIP-2001-06, ISBN 951-45-8931-9, ISSN 1455-0563 (2001). [1]

VI *A Silicon Tracker for Track Extrapolation into Nuclear Emulsions*, J. Kokkonen in G. Catanesi *et al.*, Nuclear Instruments and Methods Phys. Res. A 434 (1999) 218-226.

Throughout the overview, these publications are referred to by their Roman numerals.

[1] Results to be published in a summarizing paper.

Author's Contribution

The research reported in this Thesis has been carried out during the years 1997–2002 at the European Laboratory for Particle Physics (CERN), Geneva, mainly on NOMAD, a short baseline neutrino experiment.

The author has contributed extensively to all aspects of the research work reported in this Thesis. For Papers I, II and VI, he was a member of a small team that worked full-time on the construction, testing and assembly of the silicon modules. He has an important contribution to Paper III through supplying the Monte Carlo simulation required to obtain and test the algorithms described, as well as through the optical surveying. He also participated in obtaining the impact parameter results presented. Paper IV is largely the responsibility of the author and Paper V is solely his responsibility.

The author has actively taken part in the reporting of the research work presented in this Thesis. He has minor contributions in writing up Papers I, III and VI and he wrote some sections of Paper II. Papers IV and V were written entirely by the author.

In addition to the research reported in this Thesis, the author has participated in the data collection with the NOMAD detector as well as having responsibilities for the functioning of a NOMAD subdetector, the muon chambers. He is a co-author of several papers not mentioned in this Thesis, published mainly by the NOMAD collaboration.

Contents

1 Introduction

One of the most fundamental problems currently studied in particle physics is whether the neutrinos possess a mass. The most promising way to find evidence for neutrino masses is through searches for neutrino oscillations. Massive neutrinos would also have cosmological significance as they could be an important component of the hot dark matter in the Universe.

The Neutrino Oscillation MAgnetic Detector (NOMAD), a short baseline neutrino oscillation experiment, was installed at the CERN Super Proton Synchrotron (SPS) neutrino beam. It recorded data from 1994 to 1998 and the data analysis currently continues. The experiment was primarily designed to search for $\nu_\mu \rightarrow \nu_\tau$ neutrino oscillations by identifying the ν_τ through its charged-current interactions in the detector using kinematic techniques.

An improvement of the technique employed in NOMAD can be achieved through the excellent spatial resolution of silicon detectors. This would allow the precise determination of the position of the interaction vertex and the impact parameter of the τ decay vertex. To understand the design of a large-area silicon detector for a future $\nu_\mu \rightarrow \nu_\tau$ short baseline oscillation experiment, a silicon detector, NOMAD-STAR, was built. It was installed inside the NOMAD detector and it served to record data during 1997 and 1998.

This work, together with the publications included in this Thesis, provides a comprehensive description of the NOMAD-STAR project. Section 2 briefly discusses the theory of neutrino oscillations and reviews the most important results to date, also discussing some experiments which are presently under construction. In Sec. 3, the NOMAD detector as well as the neutrino beam are described. NOMAD provides an important aid to STAR in the reconstruction of the particle tracks resulting from neutrino interactions. It also provides precise measurements of the particle momenta and yields certain information for particle identification. The main part of this work is presented in Secs. 4 and 5. Section 4 discusses the NOMAD-STAR detector and the reconstruction, and outlines the original motivation for the building of the detector. Section 5 presents the detector performance. The noise, the hit-finding efficiency, and the alignment precision of the detector are evaluated. A study on the observation of K^0_S particles with the detector is described, including the vertex resolutions obtained in this study. The impact parameter resolution is also presented. Section 6 contains a brief discussion on the prospects of silicon detectors in neutrino physics. This section is particularly timely since recent results suggest that searches for neutrino oscillations should be conducted using long baseline experiments and therefore a NOMAD-STAR-like full-scale short baseline experiment is unlikely to be built. However, the experimental concept gains relevance in the context of a neutrino factory and other experiments. Finally, a summary of the findings is presented in Sec. 7.

2 Neutrino Oscillations

Neutrinos are described by the Standard Model of elementary particles and fundamental interactions. They are neutral leptons which interact through the weak interaction, that is, through the exchange of W and Z bosons. The electrically charged W bosons mediate charged-current (CC) interactions, while the neutral Z bosons mediate neutral-current (NC) interactions. Neutrinos are known to exist in three flavors: the electron neutrino, the muon neutrino and the tau neutrino. The Standard Model assumes neutrinos to be massless.

For massless neutrinos, the helicity of a neutrino is a good quantum number. If neutrinos constitute their own antiparticles (Majorana neutrinos), the two helicity states would be spin states of the same particle. However, if neutrinos and antineutrinos are different particles (Dirac neutrinos), the only allowed physical states would be left-handed neutrinos and right-handed antineutrinos. For massive neutrinos, helicity is not a good quantum number since it depends on the frame of reference. Therefore, massive Dirac neutrinos would be allowed to exist in both helicity states.

Measuring neutrino masses directly is very difficult and only upper limits are available. These are, as quoted in Ref. [1], 3 eV for the electron neutrino, 0.19 MeV for the muon neutrino and 18.2 MeV for the tau neutrino. However, the most promising way to find evidence for massive neutrinos is through an indirect method, that is, through the quantum mechanical mechanism of neutrino oscillations, which is the topic of the present section.

Here, it should be noted that neutrinos can constitute an important component of the dark matter in the Universe, as there are approximately 110 neutrinos of each of the three flavors per cubic centimeter of the Universe. Dark matter is matter whose existence has only been inferred indirectly, through its gravitational effects. The determination of the neutrino masses would therefore provide important insight into the constituents of the Universe. Conversely, cosmological models can be used to constrain the neutrino mass. Present cosmological models suggest that the heaviest neutrino mass is in the eV range [2]. This estimate is based on the presumption of stable and light neutrinos (with masses below 1 MeV).

2.1 Theory of Neutrino Oscillations

Neutrino oscillations are a consequence of neutrino mixing. According to this hypothesis, the three known neutrino flavor states $|\nu_e\rangle$, $|\nu_\mu\rangle$ and $|\nu_\tau\rangle$ do not constitute mass eigenstates but rather quantum mechanical superpositions of the three mass eigenstates $|\nu_1\rangle$, $|\nu_2\rangle$ and $|\nu_3\rangle$ with corresponding mass eigenvalues m_1, m_2 and m_3. The flavor states may be expressed as

$$|\nu_\alpha\rangle = \sum_i U_{\alpha i} \ |\nu_i\rangle \, . \tag{2.1}$$

Here the flavor index, α, corresponds to e, μ or τ and $U_{\alpha i}$ is a unitary 3×3 matrix. The evolution in time of a neutrino created at time $t = 0$ at position $\vec{x} = (0, 0, 0)$ in the state $|\nu_\alpha\rangle$ with momentum p_i and energy E_i is described by

$$|\nu_\alpha(t)\rangle = \sum_i e^{i(\vec{p}_i \cdot \vec{x} - E_i t)} U_{\alpha i} \, |\nu_i(t=0)\rangle \, . \tag{2.2}$$

The probability for a neutrino to oscillate from the flavor α to the flavor β is then given by

$$\begin{aligned} P(\nu_\alpha \to \nu_\beta) &= |\, \langle \nu_\beta | \nu_\alpha(t) \rangle \,|^2 & (2.3) \\ &= |\sum_i e^{i(\vec{p}_i \cdot \vec{x} - E_i t)} U_{\alpha i} U^*_{i\beta}|^2 & (2.4) \\ &= \sum_i \sum_j U_{\alpha i} U^*_{\beta i} U^*_{\alpha j} U_{\beta j} \ e^{i(\vec{p}_i - \vec{p}_j)\cdot \vec{x}} e^{-i(E_i - E_j)t}. & (2.5) \end{aligned}$$

Next consider neutrinos traveling along the x axis that have been produced into a definite momentum p. Furthermore, the neutrinos are assumed to be relativistic, with $|\vec{p}| \gg m_i$ (using the natural system of units in which $\hbar = c = 1$). The following approximation is made

$$E_i = \sqrt{p^2 + m_i^2} \ \approx \ p + \frac{m_i^2}{2p} \ \approx \ p + \frac{m_i^2}{2E}. \tag{2.6}$$

Inserting this into Eq. (2.5), the oscillation probability

$$P(\nu_\alpha \to \nu_\beta) \ = \ \sum_i \sum_j U_{\alpha i} U^*_{\beta i} U^*_{\alpha j} U_{\beta j} \ e^{-i \frac{\Delta m^2_{ij}}{2E} t} \tag{2.7}$$

is obtained, where $\Delta m^2_{ij} = m_i^2 - m_j^2$ is the difference between the squares of the mass eigenvalues of two mass eigenstates. For the real part of the oscillation probability, one finds

$$P(\nu_\alpha \to \nu_\beta) \ = \ \sum_i \sum_j U_{\alpha i} U^*_{\beta i} U^*_{\alpha j} U_{\beta j} \cos\left(\frac{\Delta m^2_{ij}}{2E} t \right). \tag{2.8}$$

A periodic behaviour of the transition probability, i.e., neutrino oscillations, is only possible provided that there exist nondegenerate mass eigenstates. This implies the existence of massive neutrinos since at least one mass eigenstate would have to possess a nonzero mass for a mass difference to occur.

The case of two-neutrino mixing is a useful example. In this case, the unitary matrix U is described using a single parameter θ and it may be expressed as

$$U = U^* = \begin{pmatrix} \cos\theta & \sin\theta \\ -\sin\theta & \cos\theta \end{pmatrix}. \tag{2.9}$$

Inserting this into Eq. (2.7) yields

$$P(\nu_\alpha \rightarrow \nu_\beta) = \sin^2(2\theta)\ \sin^2\left(\frac{\Delta m^2_{21} t}{4E}\right). \tag{2.10}$$

The distance the neutrino has traveled is defined as $L = ct$. The distance at which the argument of the cosine-term in Eq. (2.8) becomes 2π is defined as the oscillation length

$$L_{\rm osc} \equiv \frac{4\pi E}{\Delta m^2_{21}} = \frac{2.48(E/\text{GeV})}{(\Delta m^2_{21}/\text{eV}^2)}[\text{km}]. \tag{2.11}$$

The oscillation probability is now expressed as

$$P(\nu_\alpha \rightarrow \nu_\beta) = \sin^2(2\theta)\ \sin^2\left(\frac{\pi L}{L_{\rm osc}}\right) \tag{2.12}$$

in terms of the distance traveled. If the distance L traveled by the neutrino is much larger than the oscillation length $L_{\rm osc}$, the $\sin^2\left(\frac{\pi L}{L_{\rm osc}}\right)$-term averages to one half and the oscillatory behaviour is absent.

2.2 Neutrino Oscillation Searches

The results of searches for neutrino oscillations are summarized in this section. There are four main sources of neutrinos for oscillation searches: neutrinos produced in the nuclear reactions of the Sun, neutrinos produced due to cosmic ray interactions in the Earth's atmosphere, neutrinos produced due to the beta decay of fission fragments in nuclear reactors, and neutrinos produced in accelerators, mainly through pion decay.

Most experimental searches are carried out under the assumption of two-flavor oscillations. The most important exclusion limits as well as the preferred parameter regions are indicated in Fig. 2.1. The figure shows the Δm^2 for the appropriate mass eigenstates as functions of the mixing angle, expressed as $\sin^2(2\theta)$, with a logarithmic scale used for both axes. It is important to note that the oscillation modes for different pairs of neutrinos are shown simultaneously. The main neutrino sources and the principal oscillation modes for the experiments covered in this section are shown in Table 2.1.

2.2.1 Solar Neutrinos

The processes in the Sun are modeled by the Standard Solar Model (SSM). For a review see, for example, Ref. [2]. The main reactions for neutrino yield are:

$$p + p \rightarrow d + e^+ + \nu_e : E_\nu < 0.42\ \text{MeV}, \tag{2.13}$$

$$^7\text{Be} + e^- \rightarrow\ ^7\text{Li} + \nu_e : E_\nu = 0.384\ \text{MeV}, E_\nu = 0.862\ \text{MeV}, \tag{2.14}$$

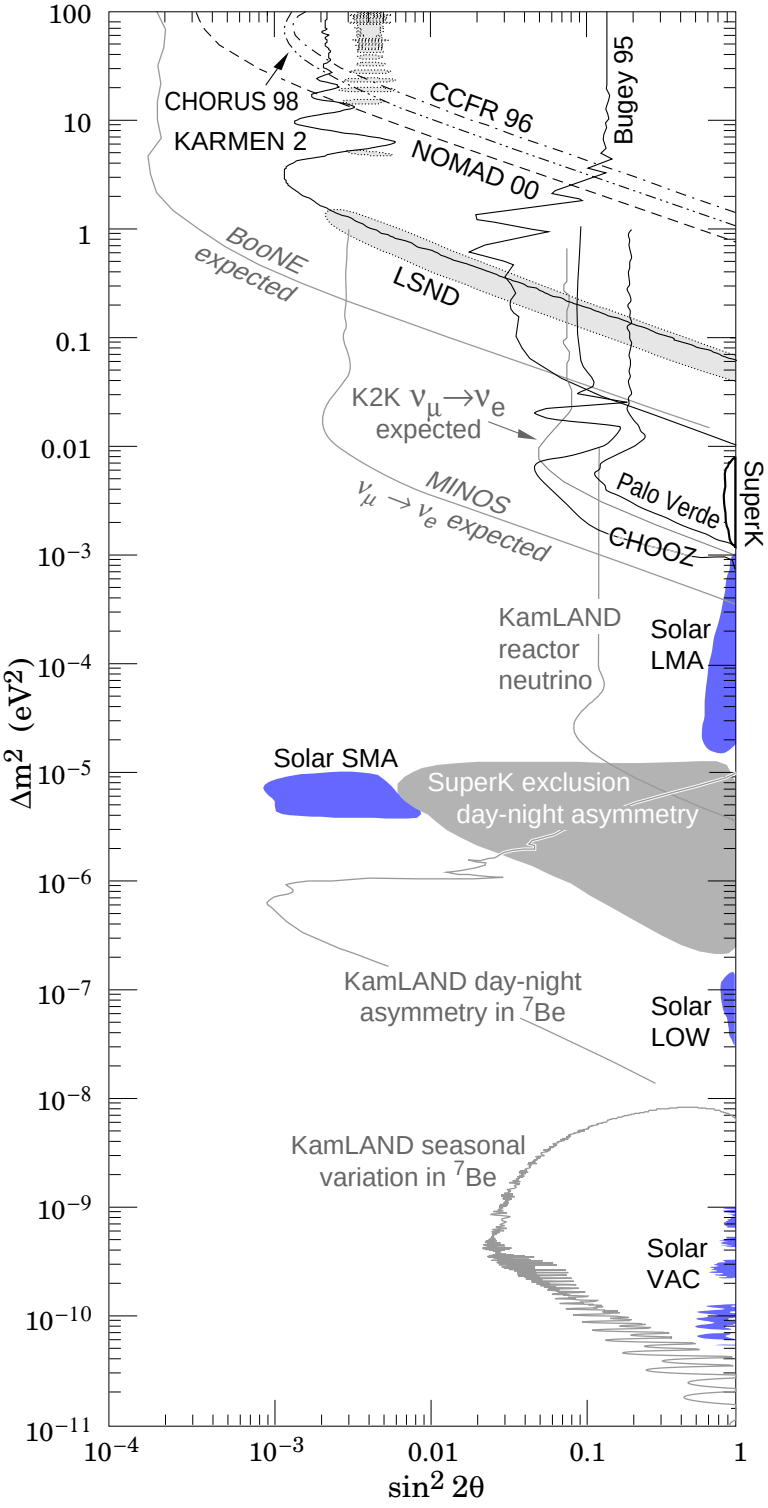

Figure 2.1: Two-flavor oscillation parameters and limits. Oscillation modes of different pairs of neutrinos are shown simultaneously. All limits are for 90 % confidence level, except for the solar LMA, SMA, LOW and VAC regions as well as the Super-Kamiokande day-night asymmetry region, which are for 99 % confidence level. Figure taken from Ref. [1].

Experiment	Full name	Neutrino source	Main search
Borexino	Borexino	Solar	$\nu_e \rightarrow \nu_x$
Bugey	Bugey	Reactor	$\overline{\nu}_e \rightarrow \overline{\nu}_x$
CCFR	Chicago Columbia Fermilab Rochester	Accelerator	$\nu_\mu \rightarrow \nu_e$
CHOOZ	CHOOZ	Reactor	$\overline{\nu}_e \rightarrow \overline{\nu}_x$
CHORUS	CERN Hybrid Oscillation Research apparatUS	Accelerator	$\nu_\mu \rightarrow \nu_\tau$
GALLEX	GALLium EXperiment	Solar	$\nu_e \rightarrow \nu_x$
Homestake	Homestake	Solar	$\nu_e \rightarrow \nu_x$
ICARUS	Imaging Cosmic And Rare Underground Signals	Accelerator Atmospheric Solar	$\nu_\mu \rightarrow \nu_\tau$ $\overset{(-)}{\nu}_\mu \rightarrow \overset{(-)}{\nu}_\tau$ $\nu_e \rightarrow \nu_x$
K2K	KEK to Kamioka	Accelerator	$\nu_\mu \rightarrow \nu_{\tau,e}$
Kamiokande	Kamioka Nucleon Decay Experiment	Atmospheric Solar	$\overset{(-)}{\nu}_\mu \rightarrow \overset{(-)}{\nu}_{\tau,s}$ $\nu_e \rightarrow \nu_x$
KamLAND	Kamioka Liquid scintillator Anti-Neutrino Detector	Reactor	$\overline{\nu}_e \rightarrow \overline{\nu}_x$
KARMEN	KArlsruhe-Rutherford Medium Energy Neutrino experiment	Accelerator	$\overline{\nu}_\mu \rightarrow \overline{\nu}_e$
LSND	Liquid Scintillator Neutrino Detector	Accelerator	$\overline{\nu}_\mu \rightarrow \overline{\nu}_e$
MiniBooNE	Mini Booster Neutrino Experiment	Accelerator	$\nu_\mu \rightarrow \nu_e$
MINOS	Main Injector Neutrino Oscillation Search	Accelerator	$\nu_\mu \rightarrow \nu_{\tau,e}$
NOMAD	Neutrino Oscillation MAgnetic Detector	Accelerator	$\nu_\mu \rightarrow \nu_\tau$
OPERA	Oscillation Project with Emulsion-tRacking Apparatus	Accelerator	$\nu_\mu \rightarrow \nu_\tau$
Palo Verde	Palo Verde	Reactor	$\overline{\nu}_e \rightarrow \overline{\nu}_x$
SAGE	Soviet-American Gallium Experiment	Solar	$\nu_e \rightarrow \nu_x$
SNO	Sudbury Neutrino Observatory	Solar	$\nu_e \rightarrow \nu_x$
SuperK	Super-Kamiokande	Atmospheric Solar	$\overset{(-)}{\nu}_\mu \rightarrow \overset{(-)}{\nu}_{\tau,s}$ $\nu_e \rightarrow \nu_x$

Table 2.1: Neutrino oscillation experiments. The main neutrino source and the principal oscillation mode for the searches are indicated. When otherwise unavailable, acronym meanings have been obtained from Ref. [3].

$$^8\mathrm{B} \rightarrow\ ^8\mathrm{Be} + e^+ + \nu_e : E_\nu < 14.06 \text{ MeV}. \tag{2.15}$$

The energy spectra for the so-called *pp* and ^{8}B neutrinos in Eqs. (2.13) and (2.15) are continuous, while those for the ^{7}Be neutrinos in Eq. (2.14) are monoenergetic due to the two-body final state. The reaction produces ^{7}Li in the ground state 90 % of the time, resulting in 0.862 MeV neutrinos. For 10 % of the reactions, the ^{7}Li is produced in an excited state, resulting in 0.384 MeV neutrinos. In terms of flux, the dominant reaction is Eq. (2.13). The SSM can be used, together with the measured luminosity of the Sun, to estimate the flux of solar neutrinos on Earth.

The first solar neutrino experiment was called Homestake [4], located in the Homestake Gold Mine in South Dakota. It started measurements on the flux of ν_e's from the decay of ^{7}Be and ^{8}B in 1970. A chlorine experiment, it used a tank filled with 615 tons of perchloroethylene (C_2Cl_4) to detect ^{37}Ar resulting from the reaction

$$\nu_e +\ ^{37}\mathrm{Cl} \rightarrow e^- +\ ^{37}\mathrm{Ar}. \tag{2.16}$$

The reaction has a threshold of 0.814 MeV and is therefore not sensitive to the *pp* neutrinos.

GALLEX [5, 6] and SAGE [7], two gallium experiments, measure the rate of the reaction

$$\nu_e +\ ^{71}\mathrm{Ga} \rightarrow e^- +\ ^{71}\mathrm{Ge}. \tag{2.17}$$

This has a threshold of 0.233 MeV. Therefore, these experiments are sensitive to the *pp*, ^{7}Be and ^{8}B neutrinos. GALLEX, at the Gran Sasso Underground Laboratory in Italy, contains 30 tons of gallium dissolved in hydrochloric acid (HCl). SAGE, at the Baksan Neutrino Observatory in the Northern Caucasus Mountains, uses 57 tons of metallic gallium, kept liquid at just over the melting point of gallium, 29.8 °C. Both the ^{37}Ar and ^{71}Ge that are produced are radioactive. At regular intervals, these reaction products are extracted and their decays are counted to determine the exponentially decaying signal. This is then used to estimate the number of neutrino capture reactions occurring in the detector.

Kamiokande [8], and its larger replacement Super-Kamiokande [9] (also known as SuperK), measure ν_e scattering in a large water-Čerenkov tank through the reaction

$$\nu_e + e^- \rightarrow \nu_e + e^-. \tag{2.18}$$

Čerenkov light is produced if the velocity of a charged particle passing through matter is greater than the velocity of light in that medium. When this occurs for the out-going electron, the Čerenkov light from the electron is detected using photomultiplier tubes. The Kamiokande threshold is 7 MeV while that of Super-Kamiokande is 6.5 MeV. Therefore, these experiments are sensitive to only the ^{8}B neutrinos. The fiducial mass of Super-Kamiokande is 22.5 ktons (total mass 50 ktons), compared to 680 tons (total mass 2 140 tons) for Kamiokande. These experiments are capable of measuring the direction of the scattered electron to distinguish between solar neutrinos and the

background signal. Super-Kamiokande is placed 1000 m underground at the Kamioka mine in Japan.

The combined results from the experiments mentioned above indicate a significantly smaller neutrino flux than that expected from the SSM calculations. The disappearance of the ν_e's is taken as an indication of neutrino oscillations to an unknown flavor state, ν_x. The following four solutions have been obtained by Bahcall *et al.* for these oscillations [10]: the small mixing angle (SMA) solution, the large mixing angle (LMA) solution, the low mass solution (LOW), and the vacuum (VAC) solution, all shown in Fig. 2.1.

The first three allowed solutions arise from the theory of neutrino oscillations in matter. Both neutral-current and charged-current interactions contribute to the amplitude of elastic $\nu_e - e$ scattering, while only neutral-current interactions contribute to elastic $\nu_\mu - e$ and $\nu_\tau - e$ scattering. Thus for electron neutrinos propagating through matter, the phase factor in Eq. (2.2) is changed from $i\vec{p}_i \cdot \vec{x}$ to $in\vec{p}_i \cdot \vec{x}$ due to the electrons contained in matter. Here n is the refractive index for the neutrino in matter, analogous to the refractive index for light in a medium. This results in a change in the oscillation probability in matter between the ν_e and other neutrino flavors. The transition probability of a ν_e to the other flavors is greatly enhanced under the condition

$$\Delta m^2 \cos 2\theta = 2\sqrt{2}\, G_{\rm F} \rho_e E, \tag{2.19}$$

where $G_{\rm F}$ is the Fermi coupling constant and ρ_e is the number density of electrons. This is known as the Mikheyev-Smirnov-Wolfenstein (MSW) effect and it predicts enhanced oscillations in the Sun (for a thorough discussion see, for example, Ref. [2]). The MSW effect also predicts a possible day-night variation of the solar neutrino rate, with a higher rate at night due to the neutrinos traversing the Earth. Some of the ν_e's which have converted to ν_μ's when traversing the Sun reconvert to ν_e's as they traverse the Earth. However, Super-Kamiokande does not observe a significant day-night variation [11] and yields the exclusion region shown in Fig. 2.1.

The fourth allowed solution is vacuum oscillation, VAC. It can be explained by oscillation parameters which strongly suppress the ^{7}Be neutrinos. This is also called the "just-so" solution as it requires a precise mathematical relation between three unrelated physical quantities: the Δm^2, the distance between the Earth and the Sun, and the energy of the ^{7}Be neutrinos. For the VAC solution, a seasonal variation of the measured solar flux that is greater than the effect caused by the variation in the Sun's solid angle (due to the eccentricity of the Earth's orbit) is expected. It is also characterized by an energy-dependent suppression of the solar neutrino flux.

SNO [12, 13], the Sudbury Neutrino Observatory, in Ontario, Canada, started observation in 1999. It uses 1 000 tons of heavy water to measure the solar neutrino flux, although the fiducial mass is smaller. Preliminary measurements have been performed using electron-scattering reactions, see Eq. (2.18), and charged-current reactions, which are represented as:

$$\nu_e + d \rightarrow p + p + e^-. \tag{2.20}$$

The experiment has an energy threshold of 6.75 MeV and is sensitive to the ^{8}B neutrinos. The electron-scattering reactions are sensitive to all neutrino flavors, albeit with a reduced sensitivity to the ν_μ's and ν_τ's, while the charged-current reactions are sensitive only to the ν_e's. Comparing the two fluxes, and also taking into account the electron-scattering flux measured by Super-Kamiokande, yields indications of the oscillation of ν_e's to an active neutrino of another flavor. This strengthens the case for oscillations of active neutrinos at large mixing angles for the solution of the solar neutrino problem [14]. In addition, the total flux of active ^{8}B neutrinos is in good agreement with the SSM. Further measurements with neutral-current interactions, sensitive to neutrinos of all flavors, are expected to significantly reduce the allowed neutrino oscillation parameter space.

Borexino [15], at Gran Sasso, is under construction and is expected to be completed in early 2002. The detector is composed of 300 tons of ultrapure liquid scintillator, with a fiducial mass of 100 tons. It will aim to bring down the detection threshold significantly from current experiments, even down to 0.25 MeV. It would then be able to measure the solar ^{7}Be neutrino flux at 0.862 MeV through electron-scattering reactions. A strongly reduced flux compared to the SSM prediction would be a strong indication of the neutrino oscillations.

KamLAND [16], which started taking data in early 2002, is a multipurpose neutrino experiment, composed of 1 000 tons of ultrapure liquid scintillator. The fiducial mass is approximately 600 tons. KamLAND is located undeground in the Kamioka mine. Although it will also attempt to detect the solar ^{7}Be neutrinos, its primary purpose is to detect $\overline{\nu}_e$'s from five nuclear reactors located 140 to 210 km from the detector. Owing to the large distance and the low energy of the neutrinos (on average 4 MeV when weighted by cross-section), KamLAND is sensitive to the solar LMA solution and can thus prove or exclude it. Using the ^{7}Be solar neutrinos, KamLAND will also be able to exclude the solar LOW solution through the day-night effect and the solar VAC solution through the seasonal effect, assuming the LOW and VAC solutions are incorrect.

2.2.2 Atmospheric Neutrinos

The interactions of cosmic rays in the upper layers of the Earth's atmosphere result in massive showers of hadronic particles. This leads to a flux of neutrinos from charged pion and muon decays through the reactions [17]:

$$\pi^\pm \rightarrow \mu^\pm + \overset{(-)}{\nu}_\mu \tag{2.21}$$

and

$$\mu^\pm \rightarrow e^\pm + \overset{(-)}{\nu}_\mu + \overset{(-)}{\nu}_e \,. \tag{2.22}$$

As a $\overset{(-)}{\nu}_{\mu}$ is produced in both reactions and additionally a $\overset{(-)}{\nu}_{e}$ is produced in the latter reaction, one naïvely expects the ratio of the muon neutrino flux to the electron neutrino flux to be two on the Earth's surface. This is in fact a good approximation for neutrinos with energies lower than 3 GeV. However, at higher energies this ratio increases as not all the muons decay before reaching the Earth. Using the ratio of the two fluxes is advantageous as the calculations of absolute atmospheric neutrino fluxes are affected by uncertainties estimated to be of the order of 20 %, while due to common systematic errors the error on the ratio is of the order of 5 %.

In addition to measuring solar neutrinos, Super-Kamiokande (as well as Kamiokande), is also capable of measuring atmospheric neutrinos [18]. It detects the neutrinos mainly through their quasi-elastic charged-current interactions:

$$\nu_{\mu}(\nu_{e}) + n \rightarrow \mu^{-}(e^{-}) + p, \tag{2.23}$$

$$\overline{\nu}_{\mu}(\overline{\nu}_{e}) + p \rightarrow \mu^{+}(e^{+}) + n, \tag{2.24}$$

or quasi-elastic-like events resulting in a single Čerenkov ring. In the case of muons, these events are characterized by a single penetrating track with the Čerenkov ring having a sharp outer edge. For the case of electrons there occurs an electromagnetic shower giving a more diffuse Čerenkov ring. These and other experiments clearly show a deficit in the measured ratio of the muon neutrino flux to the electron neutrino flux, compared to the predicted ratio.

Super-Kamiokande also measures the zenith angle distribution. The distance of flight L of neutrinos produced in the atmosphere varies as a function of the zenith angle Θ_{Z}. For example, downward neutrinos ($\cos\Theta_{\mathrm{Z}} = 1$) impinging the detector are produced in the atmosphere approximately 10 km above the detector, while upward neutrinos ($\cos\Theta_{\mathrm{Z}} = -1$) have traversed the Earth and have therefore traveled some 13000 km. Because of the directionality of the Čerenkov light, the zenith angle can be measured and the value of L can be obtained. The results of the measurements show that there are less upward muon events than expected, while the number of downward muon events is consistent with the expectations. For electrons, the number of events in both the upward and downward directions agrees with the expectations. This suggests that the deficit cannot be explained by $\overset{(-)}{\nu}_{\mu} \rightarrow \overset{(-)}{\nu}_{e}$ oscillations. Rather, the $\overset{(-)}{\nu}_{\mu}$'s oscillate either to $\overset{(-)}{\nu}_{\tau}$'s or sterile neutrinos, $\overset{(-)}{\nu}_{s}$'s, which do not undergo charged- or neutral-current interactions. The Super-Kamiokande favored region assuming $\overset{(-)}{\nu}_{\mu} \rightarrow \overset{(-)}{\nu}_{\tau}$ oscillations is shown in Fig. 2.1. Oscillations involving sterile neutrinos, although not favored, would yield oscillation parameters similar to the $\overset{(-)}{\nu}_{\mu} \rightarrow \overset{(-)}{\nu}_{\tau}$ case.

2.2.3 Reactor Neutrinos

Nuclear reactors are a well-understood and abundant source of $\overline{\nu}_{e}$'s. The neutrinos result from the beta decay of fission fragments produced in nuclear reactors and have

an average energy of a few MeV. In addition to the KamLAND experiment described in Sec. 2.2.1, there are two recent reactor experiments: CHOOZ [19, 20] and Palo Verde [21, 22]. They are similar in design and are located approximately 1 km away from the nuclear reactors. CHOOZ uses a target of 5 tons of gadolinium-doped liquid scintillator as the target for $\overline{\nu}_e$, while Palo Verde uses 11 tons. CHOOZ is located in the Ardennes region in France, while the Palo Verde experiment is in Arizona.

The experiments attempt to observe the $\overline{\nu}_e$ inverse beta decay reaction of Eq. (2.24). They do this by detecting the prompt positron signal when it annihilates to produce two photons, followed by a delayed photon signal due to the neutron being captured in the gadolinium:

$$n + p \rightarrow d + \gamma. \tag{2.25}$$

The experiments see no deficit of $\overline{\nu}_e$. The exclusion regions are shown in Fig. 2.1, providing further evidence that the Super-Kamiokande result is not due to $\nu_\mu \rightarrow \nu_e$ oscillations.

The exclusion region from Bugey [23, 24], an earlier nuclear reactor experiment located in France, is also shown Fig. 2.1. It consisted of three modules of liquid scintillator of 600 l volume (approx. 550 kg) at distances of 15 m, 40 m and 95 m from the source.

2.2.4 Accelerator Neutrinos

The advantage of using accelerators to produce neutrinos is that the flux of incident neutrinos and their energy distributions are well known. The neutrinos are the decay products of pions and kaons produced as a result of proton-target interactions.

CCFR [25], at the Fermi National Accelerator Laboratory (Fermilab) in Batavia, Illinois, attempts to detect ν_e's produced in $\nu_\mu \rightarrow \nu_e$ oscillations through their charged-current interactions:

$$\nu_e + N \rightarrow e^- + X. \tag{2.26}$$

The exclusion limits of CCFR are shown in Fig. 2.1. The detector is located at approximately 1 400 m from the neutrino source. It is composed of iron plates interleaved with liquid scintillator counters, followed by drift chambers. The iron serves as the target for the neutrino interactions while the scintillators and drift chambers track the resulting charged particles. The detector has a mass of 690 tons. CCFR has already stopped taking data.

LSND [26, 27] is designed to search for $\overline{\nu}_\mu \rightarrow \overline{\nu}_e$ oscillations. It is located at the Los Alamos Meson Physics Facility in New Mexico. The beam is composed of $\overline{\nu}_\mu$'s, ν_e's and ν_μ's, with very little contamination from $\overline{\nu}_e$'s. The neutrinos are mainly produced through the decay of positive pions and muons, Eqs. (2.21) and (2.22), and have an energy of up to some tens of MeV.

The experiment consists of 167 tons of liquid scintillator and photomultiplier tubes to detect Čerenkov light. The detector is located some 30 m from the neutrino source.

LSND searches for $\overline{\nu}_e$'s through their charged-current interaction, Eq. (2.24). This reaction is followed by a gamma ray of 2.2 MeV resulting from neutron capture, Eq. (2.25). The signature is therefore a prompt positron, which is detected through the emitted Čerenkov light, followed by a delayed (within a few hundred μs) gamma ray. LSND detects more $\overline{\nu}_e$'s particles than expected on the basis of known background. Interpreting this as oscillations, the allowed parameter region is shown in Fig. 2.1.

KARMEN [28,27], at the Rutherford Appleton Laboratory in the United Kingdom, searches for $\overline{\nu}_\mu \rightarrow \overline{\nu}_e$ oscillations using a method similar to that of LSND and it can probe most of the LSND allowed parameter space. KARMEN is composed of 56 tons of liquid scintillator, located approximately 20 m from the neutrino source. The beam, with energies similar to that used for LSND, has a time structure in which two 100 ns pulses of protons separated by 325 ns are delivered on the target with a repetition rate of 50 Hz. The time structure of the beam is an important property for the separation of background. KARMEN has observed no signal above the expected background and excludes part of the LSND allowed region, as shown in Fig. 2.1.

MiniBooNE [29], located at Fermilab, has been designed to conclusively check the LSND result. It will become operational in 2002. The detector features 800 tons of liquid scintillator in the form of mineral oil, surrounded by photomultiplier tubes. The detector is located approximately 500 m from the decay region. The beam is mainly composed of ν_μ's with a contamination of less than 0.3 % of ν_e's. Typical beam energies are in the range from 0.5 to 1.0 GeV. MiniBooNE will attempt to observe $\nu_\mu \rightarrow \nu_e$ oscillations (in particular, by detecting an excess of ν_e's) through the reactions

$$\nu_\mu + {}^{12}\mathrm{C} \rightarrow \mu^- + X \tag{2.27}$$

and

$$\nu_e + {}^{12}\mathrm{C} \rightarrow e^- + X, \tag{2.28}$$

where X represents a hadron shower (hadrons are particles composed of quarks). The expected exclusion region for the case of no oscillations is shown in Fig. 2.1, labeled "BooNE". As can be seen, it fully covers the LSND allowed region. If an unambigious oscillation signal is observed, a second identical detector would be placed in a new position.

The two experiments at CERN, CHORUS and NOMAD, search mainly for $\nu_\mu \rightarrow \nu_\tau$ oscillations. They are installed one after the other some 800 m from the proton target. The beam is composed mainly of ν_μ's, with essentially no contamination from ν_τ's. The average energy is 24 GeV. The ν_τ's are detected through charged-current interactions

$$\nu_\tau + N \rightarrow \tau^- + X, \tag{2.29}$$

followed by τ decay.

CHORUS [30, 31] uses 770 kg of emulsions in attempting to directly view the resulting τ particle and the charged tracks produced in the τ decay. The emulsion needs to be removed from the detector to be scanned using microscopes to find the neutrino interactions. NOMAD, on the other hand, is an electronic detector using drift chambers with a fiducial mass of 2.7 tons. It uses kinematic criteria to infer the occurrence of the τ decay. Neither experiment has seen signs of neutrino oscillations and the exclusion limits are shown in Fig. 2.1. NOMAD will be further discussed in Sec. 3.

Several long baseline experiments to search for the oscillation of muon neutrinos to neutrinos of another flavor are starting up or being planned. The main goal of these experiments is to verify the atmospheric neutrino results and to measure the oscillation parameters.

The K2K project [32] began operating in 1999. It uses a neutrino beam aimed at the Super-Kamiokande detector at a distance of 250 km. The beam consists mainly of ν_μ's with 4 % and 1 % contaminations of $\overline{\nu}_\mu$'s and ν_e's, respectively. The average energy of the beam is 1.3 GeV. As the beam energy is below the threshold required for τ production, a search for the appearance of ν_τ's in the beam is not possible and, instead, a deficit of ν_μ's is searched for. To better understand the beam, a 1 000 ton water-Čerenkov detector is placed at a distance of only 300 m from the neutrino source. This near-detector uses the same technology and analysis algorithms as the Super-Kamiokande detector (the far-detector). In addition, several other detectors are used at the near position to provide further information on the neutrino interactions occurring there. The expected exclusion plot for the case of no $\nu_\mu \rightarrow \nu_e$ oscillations is shown in Fig. 2.1.

MINOS [33], which is expected to start taking data in late 2003, is to be located at a distance of some 730 km from the neutrino source at Fermilab. The experiment has been designed to be able to explore the full area of parameter space suggested by Super-Kamiokande. The energy of the beam, consisting primarily of ν_μ's, can be modified during the experiment. The average energies of the different configurations range from a few GeV to tens of GeV. The main detector, with 5 400 tons, will consist of iron plates, serving as the target for the neutrino interactions, and of interleaved scintillators for particle tracking purposes. Just like for K2K, a near-detector a few hundred meters from the neutrino source is planned. It is designed to be as identical as possible to the far-detector in its performance characteristics and it will have a mass of 980 tons. The primary aim of the experiment will be to verify the $\nu_\mu \rightarrow \nu_\tau$ oscillation hypothesis by detecting a deficit of ν_μ's in charged-current interactions, without a simultaneous loss in neutral-current events.

The CERN Neutrino Beam to Gran Sasso (CNGS) project [34] is due to be operational in 2005. It will use a new neutrino beam from the CERN SPS, with a mean energy of a few tens of GeV. It will be aimed towards detectors some 730 km away at the Gran Sasso laboratories in Italy. The importance of the experiment is that it would search for the appearance of ν_τ's from the predominantly ν_μ beam. Two detector concepts are being considered. One is ICARUS [35], to be composed of several

modules of liquid argon time-projection chambers. A 600 ton module is currently being tested. Further modules are to be built to reach the 5 000 ton sensitive mass required for the final phase of the project. ICARUS will also perform atmospheric and solar neutrino measurements. The other detector concept is OPERA [36]. It would be composed of modules of passive material plates interleaved with sheets of emulsion, with a total mass of up to 2000 tons. This target would be complemented by electronic trackers and a magnetized iron spectrometer to identify muons and to reconstruct their tracks.

3 The NOMAD Experiment

The STAR detector was installed in the NOMAD experiment for the period 1997–98 for the purpose of testing the detector concept using neutrino interactions. However, the mass of STAR is too low for an oscillation search of reasonable sensitivity. STAR relies on the NOMAD magnet and subdetectors as aids in the reconstruction. This section first discusses the neutrino beam and then introduces NOMAD and its subdetectors and discusses the triggering system. Some of the methods employed in the analysis of events by NOMAD are also briefly mentioned and they serve as a comparison to those employed by STAR. STAR itself is discussed in detail in Sec. 4.

Figure 3.1 shows the general layout of NOMAD, described in detail in Ref. [37]. NOMAD consists of several subdetectors, most of which are located in a dipole magnet with a field volume of $7.5 \times 3.5 \times 3.5$ m^3. Going downstream along the beam, there are the front calorimeter, STAR, the drift chambers, the transition radiation detector, the preshower detector, the electromagnetic calorimeter, the hadronic calorimeter and an iron filter, followed by the muon chambers. The veto planes, forming part of the triggering system, are on either side of the front calorimeter. The two trigger planes sandwich the transition radiation detector. In addition, STAR has its own veto and trigger planes. The NOMAD coordinate system has its x axis pointing perpendicularly into the plane of the figure, the y axis pointing towards the top of the detector and the z axis horizontal, approximately along the direction of the neutrino beam (the beam in fact points upwards at an angle of 42 mrad with respect to the z axis). The strength of the magnetic field is 0.4 T and it is orientated parallel to the x axis. STAR is located in front of the drift chambers within the magnet.

3.1 The Neutrino Beam

The neutrino beam is produced from the decay of pion and kaon mesons resulting from the interactions of 450 GeV protons from the CERN Super Proton Synchrotron (SPS) impinging on a beryllium target. The accelerator works in cycles of 14.4 s, during which the protons are extracted twice at 2.4 s intervals and directed onto the target (this is also known as a neutrino spill). Each spill lasts for 4 ms. A typical proton extraction contains some 10^{13} protons. A measure for the flux of the beam is the number of protons impinging on the target (POT), which was $1.7 \cdot 10^{19}$ in 1997 and $1.8 \cdot 10^{19}$ in 1998.

The pions and kaons produced in the proton-target interactions are focused by a pair of coaxial magnetic lenses after which they are allowed to decay in a vacuum tunnel of 290 m length. This is followed by several hundred meters of iron and earth shielding to range out the muons and absorb the hadrons to ensure that only neutrinos and some of the highest-energy muons reach NOMAD. NOMAD is located 835 m from the beryllium target and the average distance between the meson decay

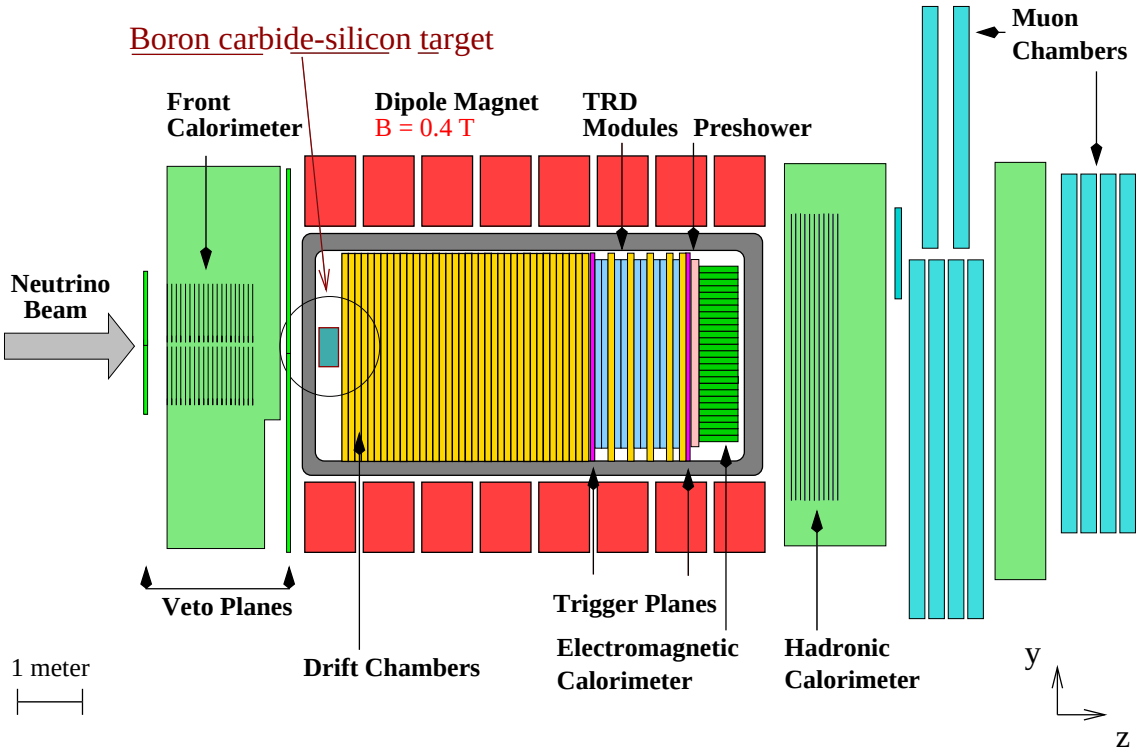

Figure 3.1: Side view of the NOMAD detector. Going downstream along the beam, there are the front calorimeter, STAR, the drift chambers, the transition radiation detector, the preshower, the electromagnetic calorimeter, the hadronic calorimeter and the muon chambers. The veto planes (**V**), forming part of the triggering system, are on either side of the front calorimeter, while the two trigger planes ($\mathbf{T_1}$, $\mathbf{T_2}$) sandwich the transition radiation detector.

point and NOMAD is 620 m.

In addition to the ν_μ's, which is the primary component of the beam, there appear low contaminations of $\overline{\nu}_\mu$'s, ν_e's and $\overline{\nu}_e$'s. The contamination from tau neutrinos produced in the beam or along the beam line has been estimated to be negligible. The predicted composition and average energy of the beam at the position of STAR is shown in Table 3.1. Although similar to those of NOMAD, there are slight differences due to STAR being located in the center of the beam. The full width at half maximum (FWHM) of the neutrino flux is approximately 2.5 m. The neutrino energy spectrum at the position of STAR is shown in Fig. 3.2. During 1998, there was a period of a few weeks when data was recorded using a beam composed primarily of antineutrinos. The antineutrino beam was produced by changing the polarity of the magnetic lenses to focus negative pions and kaons instead of positive pions and kaons.

Neutrino	Average energy (GeV)	Concentration (%)
ν_μ	30.60	94.12
$\overline{\nu}_\mu$	19.83	5.02
ν_e	42.18	0.69
$\overline{\nu}_e$	31.11	0.17

Table 3.1: Predicted composition and average energy of the beam at the position of STAR.

In addition to neutrinos, muons, which are used for detector calibration, are sent to NOMAD. This is done during the 2 s gap between the two proton extractions in the SPS.

3.2 NOMAD Subdetectors

The purpose of the front calorimeter (FCAL) is to study multimuon physics and to search for neutral heavy particles produced in the neutrino interactions. It is composed of iron plates interleaved with scintillators and has a total mass of about 17.7 tons. The iron functions as the target for the neutrino interactions while the scintillators record the positions of the charged particles produced in the neutrino interactions. The charged particles traversing the scintillators generate optical photons, which can be read out by photomultipliers. The photomultipliers convert the photons to photoelectrons, which are then accelerated to form an electron cascade and read out as an output signal.

The drift chambers (DC) form the principal subdetector of NOMAD, providing both the target material for the neutrino interactions and the tracking of the particles. The chambers are built of panels of aramid fibers in a honeycomb structure. The panels are sandwiched between kevlar-epoxy resin skins, which serve as the target. The chambers are filled with a gas mixture of 40 % argon and 60 % ethane. Charged particles traversing the chambers ionize the gas. The chambers contain potential wires

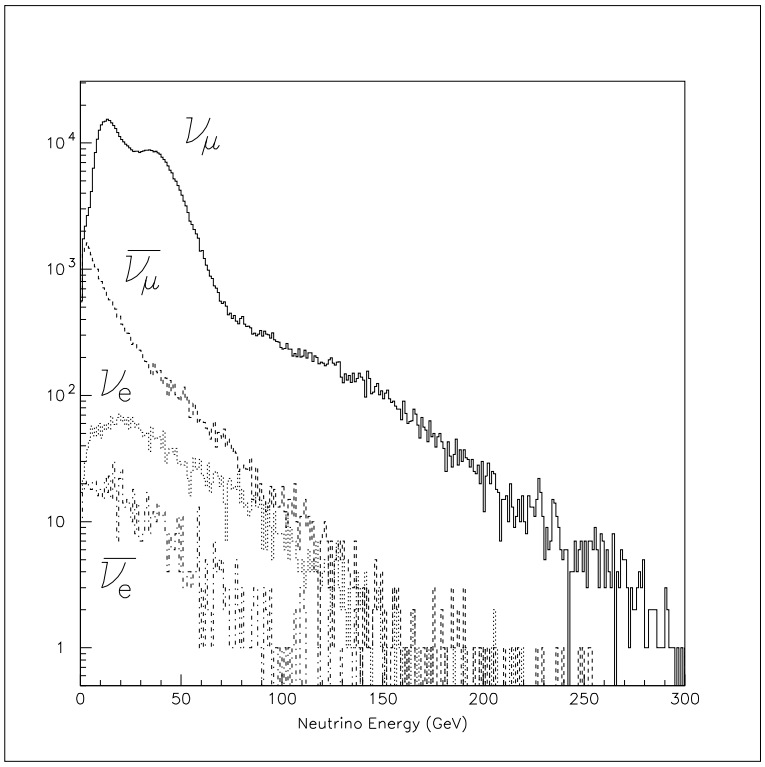

Figure 3.2: Predicted neutrino energy spectrum at the position of STAR.

at -3200 V (cathode) and sense wires at 1750 V (anode) as well as field-shaping strips to produce an electric field of 1 kV/cm. With this electric field and gas mixture, the ionization electrons drift at 50 mm/μs. Each chamber consists of three planes, with the sense wires in the xy plane. The central plane has the sense wires in the direction of the magnetic field, while the other two planes have the sense wires at angles of -5° and +5° with respect to the magnetic field. By using timing information from the trigger planes in conjunction with the information provided from the sense wires, track positions can be determined with a resolution of 1.5 mm in the x direction and approximately 150 μm in the y direction. For charged hadrons and muons traveling normal to the plane of the chambers, the momentum resolution has been empirically parametrized as

$$\frac{\sigma_p}{p} \approx \frac{0.05}{\sqrt{L}} \oplus \frac{0.008p}{\sqrt{L^5}}, \tag{3.1}$$

where $\oplus$ implies adding in quadrature, the momentum p is in GeV (the natural system of units is retained) and the track length L is in m. There are a total of 41 target chambers (44 prior to the installation of STAR), with an additional five chambers interleaved with the transition radiation detector to improve the lever-arm for tracking. The total fiducial mass of the chambers is 2.7 tons over a cross-sectional area of 2.6 $\times$ 2.6 m^2.

The purpose of the transition radiation detector (TRD) is to identify the electrons

amongst the pions (or other strongly interacting particles). The pion rejection factor is higher than 10^3 for a 90 % electron detection efficiency in the momentum range from 1 to 50 GeV. The TRD is composed of nine modules, each of which has a radiator followed by a detection plane. The area covered is 2.85×2.85 m^2. The radiator consists of 315 polypropylene foils of 15 μm thickness separated by 250 μm air gaps. The detection planes are composed of 176 vertical proportional tubes which are circular with a diameter of 16 mm. They are filled with a gas mixture of 80 % xenon and 20 % methane. When a charged particle crosses the interface between two media of different optical properties, electromagnetic radiation is emitted. The amount of radiated energy depends on the medium being traversed and is proportional to the Lorentz factor $\gamma = E/m$, where E is the particle energy and m the mass. For charged particles with a sufficient γ, X-rays are emitted, with the typical emission angle being $1/\gamma$. Electron identification in the TRD is based on the difference in total energy deposited in the straw tubes by particles with different Lorentz factors. All charged particles deposit energy in the straw tubes through ionization and for approximately $\gamma > 500$ (mainly electrons in NOMAD), enough energy is deposited by X-rays to enable the discrimination between electrons and pions.

The preshower (PRS) is composed of a lead-antimony (96 %-4 %) converter, which is 1.6 radiation lengths thick. This is followed by two planes of proportional tubes filled with a mixture of 80 % argon and 20 % carbon dioxide. The tubes have a square cross-section of 9×9 mm^2. The converter initiates photon conversions and electron showering. The PRS has a higher spatial resolution than the electromagnetic calorimeter (ECAL) which follows it. This can be used to separate adjacent particles in the electromagnetic calorimeter. The PRS is also used in conjunction with the TRD and the electromagnetic calorimeter for electron identification.

The purpose of the ECAL, in addition to providing information for electron identification, is to measure electron and photon energies in the range of 100 MeV to 100 GeV. It is composed of 875 lead-glass blocks with a cross-sectional area of 79×112 mm^2 and a depth of 19 radiation lengths. The lead-glass blocks are equipped with photomultiplier tubes for the readout. Electrons and photons traversing the lead-glass blocks form electromagnetic showers through bremsstrahlung and pair production. It is by measuring the amount of Čerenkov light produced that the energy of the original electron or photon is determined. The energy resolution of the ECAL is

$$\frac{\sigma_E}{E} \approx \frac{0.032}{\sqrt{E}} \oplus 0.01, \tag{3.2}$$

where the energy E is expressed in GeV.

The hadronic calorimeter (HCAL) is an iron-scintillator sampling calorimeter, intended to detect neutral hadrons and to identify charged hadrons (particles composed of quarks). It is 3.1 interaction lengths deep. The HCAL is part of the NOMAD support structure which has been instrumented with scintillators. It forms a wall 1.5 m thick, which acts as a filter for the muon chambers, located farther downstream. The combined hadron shower energy resolution of the electromagnetic and hadronic calorimeters, from Ref. [38], is

$$\frac{\sigma_E}{E} = \frac{0.97}{\sqrt{p}} + 0.14, \tag{3.3}$$

where the momentum p is expressed in GeV.

The muon chambers consist of 10 drift chambers arranged in pairs. In addition, several scintillators are used to cover gaps between the muon chambers. Only muons and energetic hadrons are expected to reach the muon chambers due to the absorption of hadrons in the HCAL. There is an additional iron filter between some of the chambers. The energy deposited in the HCAL can be used to distinguish between muons and energetic hadrons, as muons, being minimally ionizing particles, only leave small amounts of energy in the HCAL compared to hadrons, which produce hadronic showers. The muon chambers are of a different design to the NOMAD drift chambers, although they use the same gas mixture of 40 % argon and 60 % ethane. The position resolution for hits is approximately 500 μm, depending on the track angle. The efficiency to reconstruct track segments is 97 %.

In order for an event to be recorded, certain triggering conditions have to be fulfilled. This is to keep the total stored event rate low. Typically, a triggering condition requires a combination of signal (trigger) and no signal (antiveto) from the various elements of the triggering system within a specified time window. The main elements of the NOMAD triggering system are the veto planes and two trigger planes. The veto planes consist of 59 scintillators, covering an area of 5×5 m^2. The purpose of the veto counter is to reject charged particles produced upstream of NOMAD. The veto planes ($\mathbf{V}$) are located in the front of NOMAD on either side of the FCAL. Of the two trigger planes in NOMAD, $\mathbf{T_1}$ is located just after the DC and $\mathbf{T_2}$ is positioned behind the TRD. They each consist of 32 scintillators with a fiducial area of 280×286 cm^2. The triggering condition required for a charged-current or neutral-current neutrino interaction in the drift chambers is that the veto planes must not have fired and there must have been a coincidence between the two trigger planes ($\overline{\mathbf{V}}\mathbf{T_1}\mathbf{T_2}$). Other triggering conditions can also be formed, for example by using some of the NOMAD subdetectors.

3.3 The NOMAD Detection Technique

The main aim of NOMAD is to detect $\nu_\mu \rightarrow \nu_\tau$ through the appearance of ν_τ's in the neutrino beam. The ν_τ can be searched for through its charged-current interaction, Eq. (2.29). This interaction in turn is identified through the decay of the τ^-. NOMAD can search for all the principal τ decay channels, such as $\tau^- \rightarrow e^- \, \overline{\nu}_e \, \nu_\tau$, $\tau^- \rightarrow \mu^- \, \overline{\nu}_\mu \, \nu_\tau$, $\tau^- \rightarrow \pi^- \pi^0 \, \nu_\tau$ and $\tau^- \rightarrow \pi^- \, \pi^+ \, \pi^- \, \nu_\tau$. The smallness of the ν_e component in the beam makes the search using the electron channel particularly sensitive as few ν_e CC background events are produced. The searches mainly consider deep inelastic scattering (DIS) events, which, in addition to the outgoing lepton, result in a hadronic jet. The jet is formed as a result of the break-up of the nucleus, giving rise to hadrons. The various NOMAD analyses select DIS events by requiring

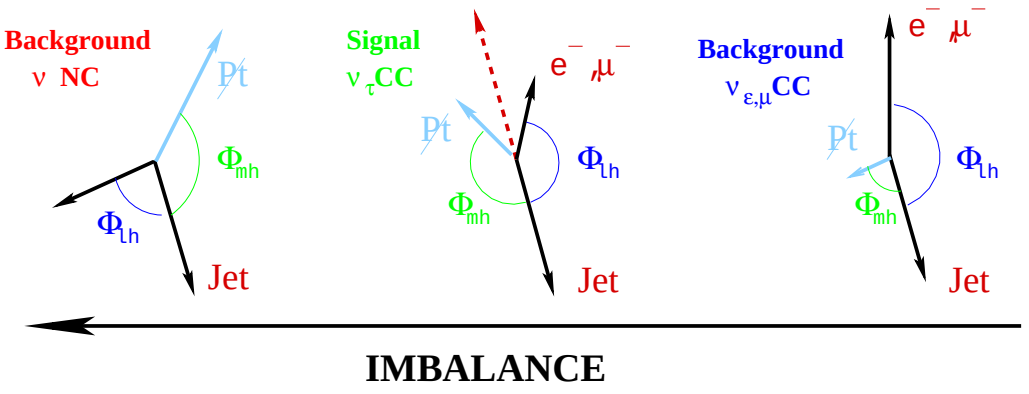

Figure 3.3: Momentum imbalances for τ decay signal events as well as neutral-current and charged-current backgrounds. The missing transverse momentum is denoted by $\not{P}t$ and the angle it forms with the jet transverse momentum is denoted by $\Phi_{\rm mh}$. The angle formed by the transverse momentum vectors of the jet and the τ decay product (a lepton in this case) is denoted by $\Phi_{\rm lh}$.

the momentum of the jet to be at least 1.5 GeV.

Given the lifetime of the τ^- and the beam energy, the decay distance of the τ^- is approximately 1 mm. The spatial resolution of NOMAD is not good enough to detect the τ^- directly, either through the impact parameter in the case of a single-prong decay or by measuring the vertex separation for multiprong decays. Instead, NOMAD uses kinematic criteria, based on the precise measurement of the missing transverse momentum in the final state. The direction and magnitude of this momentum imbalance are used as criteria in selecting candidate events. In τ decays, the missing transverse momentum arises from the new neutrinos produced in the decay. These signal events are characterized by a large missing transverse momentum which is nearly opposite in direction to the hadronic jet, see Fig. 3.3.

Both neutral-current and charged-current interactions contribute to the background. In neutral-current events, one or more of the particles in the hadronic jet may be mistakenly identified as products of the τ decay (depending on the decay channel under consideration). The events are characterized by a missing transverse momentum typically larger than that for the ν_τ CC signal events due to the outgoing neutrino. The orientation of the missing transverse momentum is opposite to that of the hadronic jet. Charged-current interactions of ν_e's or ν_μ's can also contribute to the background. Typically, these are due to neutral hadrons escaping the detector without being detected or due to poor reconstruction, such that the momentum is incorrectly measured. These events are characterized by a small missing transverse momentum with a random orientation with respect to the hadronic jet.

The NOMAD oscillation analyses and their results are presented in detail in Refs. [39–42]. The results of these analyses also allow interpretation in terms of a search for $\nu_e \rightarrow \nu_\tau$ oscillations. Another important search conducted by NOMAD is for $\nu_\mu \rightarrow \nu_e$ oscillations. In addition to neutrino oscillations, NOMAD

addresses several other neutrino physics topics as well. Neutrinos make good probes of hadronic matter as they are structureless and their weak interactions are well understood. This invites studies on the production of strange and charmed particles (particles containing strange and charm quarks, respectively) as well as the polarization of lambda particles, allowing the testing of different models of the nucleon spin content. Searches have been conducted for particles such as new gauge bosons, light scalar or pseudoscalar particles, and neutral heavy leptons.

4 The Silicon TARget - STAR

The STAR detector was built in order to better understand how silicon detectors can be used for neutrino physics, in particular in the context of a short baseline $\nu_\mu \rightarrow \nu_\tau$ oscillation experiment. The excellent spatial resolution of silicon detectors allows for a precise determination of the position of the interaction vertex and the impact parameter of the τ decay vertex resulting from the charged-current interaction of the ν_τ. STAR is used to show that a proposal for such a silicon detector-based experiment, called NAUSICAA, is viable.

In this section, the general operating principles of silicon detectors are first presented. Next, the NAUSICAA proposal for a short baseline neutrino oscillation experiment using silicon technology is discussed. This proposal provides the motivation for STAR. The main content of this section provides a description of STAR itself and the algorithms used for event reconstruction. The implementation of the Monte Carlo simulation is also given.

4.1 Silicon Detectors

One of the principal advantages of a silicon detector compared to other types of detectors is its good energy resolution. One electron-hole pair is produced for every 3.6 eV of energy deposited in the silicon detector by a particle, compared to approximately 30 eV needed to ionize a gas molecule in a gaseous detector. For a typical detector thickness of 300 μm, a minimum-ionizing particle (m.i.p.) produces approximately 20 000 electron-hole pairs. A reconstructable signal is defined a hit. Other advantages of silicon detectors include their compact size and fast timing characteristics.

Silicon is a group IV element, having four valence electrons. The excitation of an electron to the conduction band leaves a hole in the valence band. The hole behaves essentially like a positively charged particle. To improve conductivity, the silicon can be doped with materials which increase the charge carrier density. Doping with a group III element, which has three electrons in the valence band, forms a p type material. It is called an acceptor as it can easily attach electrons from the silicon atoms, therefore leaving holes as the majority carriers. Similarly, silicon can be doped with a group V material, containing five valence electrons, to produce an n type material. The group V elements contain five valence electrons, leaving one surplus electron after the covalent bonds have been formed. They are called donors, with electrons being the majority carriers.

Silicon detectors are simply reverse-biased $p-n$ junctions. When the p type and n type materials are combined, the different charge-carrier concentrations favor the diffusion of holes from the p side to the n side while electrons migrate from the n side to the p side. Due to the presence of the remaining ionized atoms, an electric field is created that diminishes the tendency for further diffusion. This sets up a region which

is depleted of free charge carriers. The depletion region extends into the two regions in inverse proportion to the concentrations of the dopant impurities. Doping the silicon in such a way that the acceptor density is much higher than the donor density results in a deep depletion region for the n type material and a shallow one for the p type material. Therefore, a particle detector typically consists of a highly doped p type material, called p^+, and an n type material containing a low concentration of donors. In this case, the n type material serves as the active volume for the detector and the p^+ type layer can be made thin. The detectors are reverse-biased to fully deplete the detector of charge carriers. The resulting electric field drifts the holes and electrons liberated by traversing particles to the electrodes, where the resulting charge can be collected. It should be noted that electron-hole pairs are continuously formed in the depletion region due to thermal processes, giving rise to a leakage current. This forms an important source of noise for the silicon detectors.

In order to improve the resolution, the p side can be divided into an array of parallel narrow strips to form microstrip detectors. This is in effect a series of $p-n$ junctions sharing a common n type substrate. For a discussion of (non-radiation hard) silicon microstrip detectors used in high-energy physics, see Ref. [43].

4.2 Motivation for STAR - NAUSICAA

A proposal for a new short baseline $\nu_\mu(\nu_e) \rightarrow \nu_\tau$ oscillation experiment, which could be placed at the CERN SPS neutrino beam, was made in Refs. [44,45]. The Neutrino ApparatUS with Improved CApAbilities (NAUSICAA) combines the kinematic techniques used by NOMAD and the vertexing techniques used by CHORUS to improve on their sensitivity by approximately an order of magnitude.

The heart of the NAUSICAA detector is a finely instrumented target. It consists of a sandwich of a target material, such as boron carbide, and an active part of silicon detectors. Downstream of the instrumented target, there are tracking detectors for momentum measurement, a calorimeter, and a muon identification system. In an alternative design, the silicon detectors are replaced by glass capillaries filled with a scintillating liquid.

NAUSICAA aims to simultaneously measure the two signatures of the τ decay. Excellent tracking and calorimetry, as in NOMAD, are required to measure the missing transverse momentum resulting from τ decays. In order to measure the signature arising from the short decay length of the τ, the vertices and tracks have to be measured with a precision of a few tens of microns. Here the nonzero impact parameters of tracks produced in τ decays are exploited. The impact parameter d is defined as the closest signed (positive or negative) distance of a track or its extrapolation to the primary vertex, as shown in Fig. 4.1. The figure shows a ν_τ CC event with the decay $\tau^- \rightarrow \mu^- \, \overline{\nu}_\mu \, \nu_\tau$, where the neutrinos are invisible and cause the "kink" in the muon track. The main background to this process is due to ν_μ CC interactions, also shown in the figure. The expected root-mean-square (RMS) value for the impact parameter for the ν_τ CC events is 62 μm. The ν_μ CC events, due to measurement errors,

have an expected RMS impact parameter of 28 μm. These distributions are shown in Fig. 4.2. Also shown are the impact parameter significance distributions. The impact parameter significance is the impact parameter divided by the calculated uncertainty. For ν_μ CC events, a Gaussian distribution with a mean of zero and a width of one is expected. A selection efficiency of 10 % is expected for the $\tau^- \rightarrow \mu^- \overline{\nu}_\mu \nu_\tau$ decays.

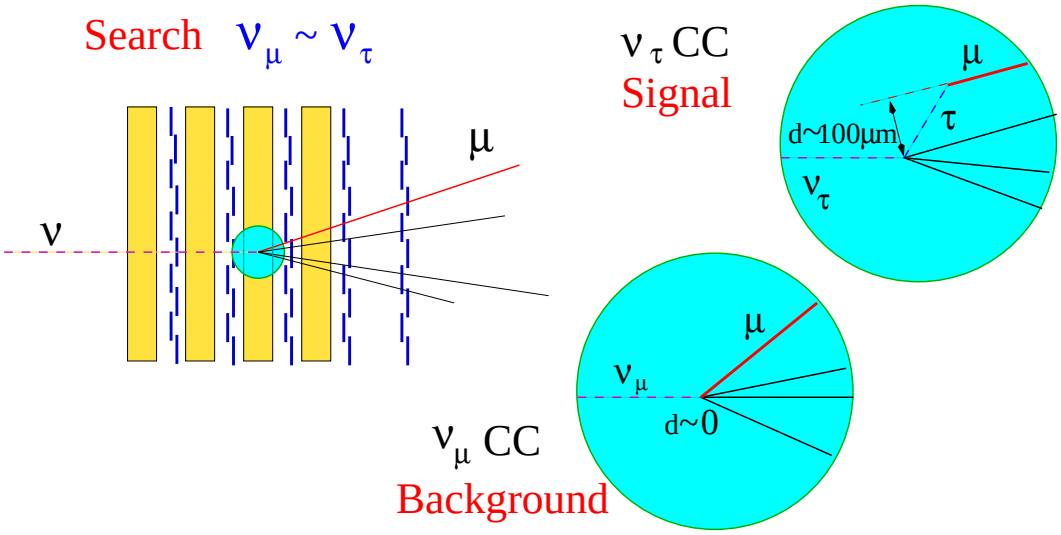

Figure 4.1: Illustration of impact parameters resulting from perfectly reconstructed ν_τ CC and ν_μ CC interactions.

The second signature measured by NAUSICAA is based on two vertices. If the τ particle decays into three or more charged particles, a secondary vertex can be reconstructed, allowing an alternative method to the impact parameter measurement to be used. In the NAUSICAA simulation the distance between the two vertices, representing the τ decay length, is measured with an estimated resolution of approximately 100 μm. The expected selection efficiency for $\tau^- \rightarrow \pi^- \pi^+ \pi^- \nu_\tau$ decays is 23 %.

A variant of the NAUSICAA design uses an emulsion instead of a passive target. In this design, the good resolution of silicon detectors would be used as an aid in selecting and locating events in the emulsion. It was estimated that this could reduce the load of background events to be scanned by up to two orders of magnitude.

STAR was built to provide improved understanding on the use of silicon in a large-scale instrumented target and, in particular, to test the techniques involved in measuring the impact parameter and measuring secondary vertices.

4.3 Description of STAR

STAR consists of five layers of silicon detectors interleaved with four layers of passive boron carbide (B_4C) target, as shown in Fig. 4.3. Each plate of (B_4C) is followed by a layer of silicon with an additional layer of silicon downstream for better track

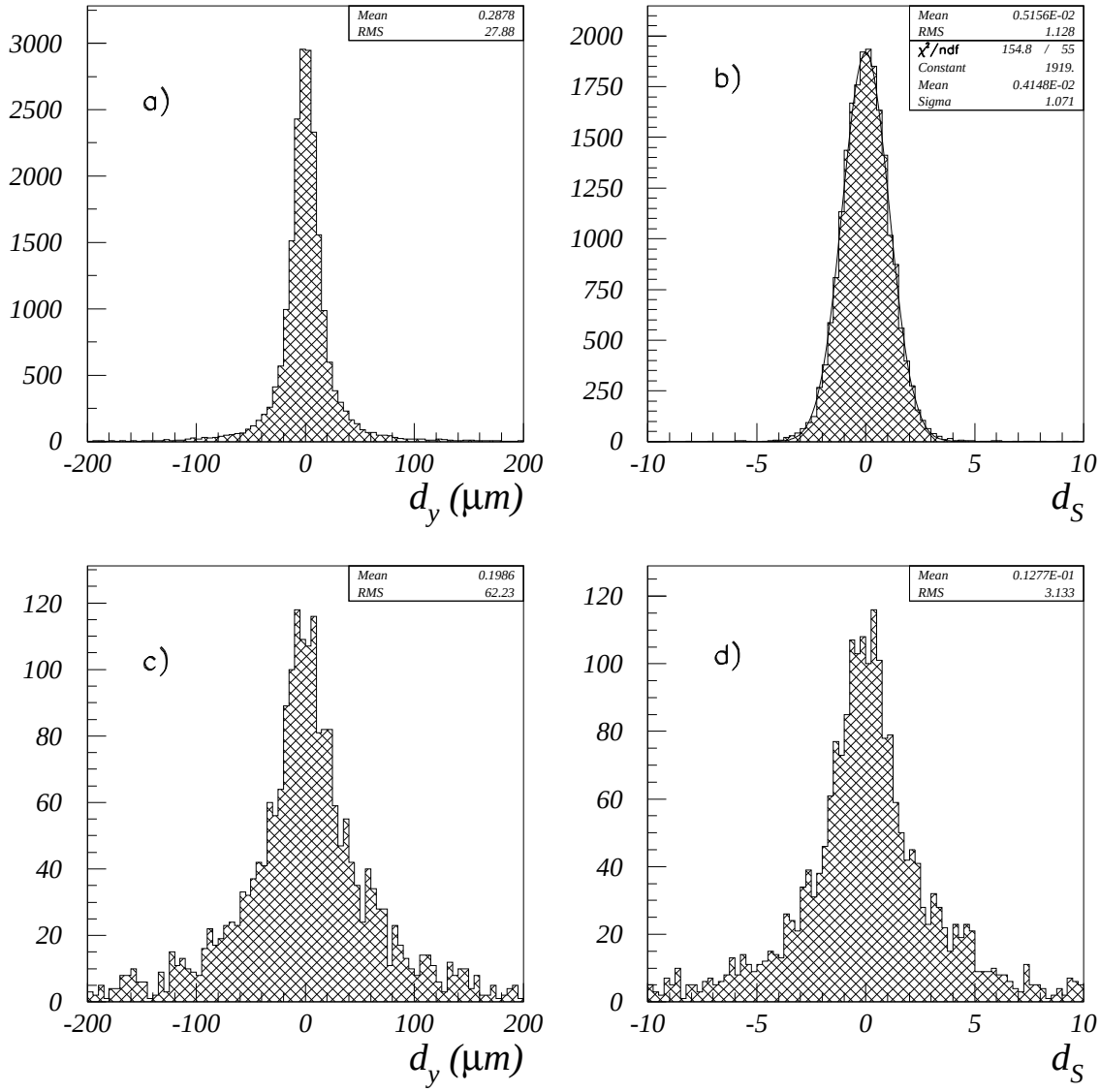

Figure 4.2: Impact parameter, d_y, and impact parameter significance, d_s, for ν_μ CC interactions (a and b) and ν_τ CC interactions (c and d). Figure taken from the NAUSICAA detector simulations in Ref. [44].

reconstruction. The B_4C and silicon layers are spaced at 3.6 cm intervals. A silicon layer consists of 10 overlapping modules (ladders) of silicon detectors, each module consisting of 12 daisy-chained microstrip silicon detectors on a supporting carbon-fiber backbone. The B_4C plates each have dimensions $72 \times 31 \times 2$ cm^3 and a density of 2.5 g/cm^3. The total mass of the target is 45 kg, with a total depth of 0.37 radiation lengths (X_0) and 0.25 interaction lengths (λ_I). The material in the silicon planes contribute a further 0.18 radiation lengths on average and 0.23 at maximum, depending on the path followed within the detector.

The individual detectors, manufactured by Hamamatsu Photonics, Japan, have dimensions of 6.00 cm $\times$ 3.35 cm^2 and they are 300 μm thick. The silicon detectors are not active throughout their whole area, but have dead areas along the edges. A particle passing through a dead area does not record a signal. The strip pitch is 25 μm and the readout pitch is 50 μm, with a total of 641 readout strips. The strips between the readout strips are allowed to float electrically. Capacitive coupling increases the lateral spread of the signal and, therefore, the floating strips enhance the resolution. The strips are highly doped p type material, also known as p^+ type. They are implanted into a high-resistivity n type substrate and the readout strips, which are metallized, are AC coupled to the readout electronics by a silicon oxide layer. The biasing of the detectors is done via the FOXFET mechanism using a biasing resistor, see for example Ref. [46]. The reverse-bias voltage is 60 V. The individual detectors were visually scanned for defects under a microscope and the leakage current was measured. Out of 623 detectors tested in this way, 19 were considered to be defective.

A silicon module is shown in Fig. 4.4. The silicon detectors are glued onto a thin kapton foil which insulates them electrically from a carbon-fiber support. The support consists of four rods of carbon-fiber and has a maximum thickness of 0.5 cm. Aluminium and brass supports with fixing and alignment holes are attached to the ends of the carbon-fiber structure. The detectors are bonded in series to provide an active length of 72 cm and are the longest built to date. They are read out at one end, with the readout performed with five VA1 chips manufactured by IDE AS, Norway. The chips are mounted on a printed hybrid circuit board, which is attached to a ceramic plate and then glued to the aluminium support. The chips consist of 128 charge-sensitive, low-power (1.2 mW per channel) and low-noise preamplifiers, followed by CR-RC shapers, track-and-hold circuitry, output multiplexing and a multiplexing calibration circuit. The five chips on each module result in 640 channels per module. The 1280 channels on two modules are read out sequentially using a clock operating at a frequency of 1 MHz. The output signals are amplified on a repeater card, shared by two modules. A shaping time of approximately 3 μs is used. The repeater card also drives the clock signals and allows control of the operation of the readout chips. The sequential signal from 1280 channels is finally passed to a 10 bit analog-to-digital converter (ADC).

The silicon modules were extensively tested during production. The response of the VA1 chips on the hybrids was tested before assembly, with chips having more than two defective channels rejected. After assembly, the leakage currents of the

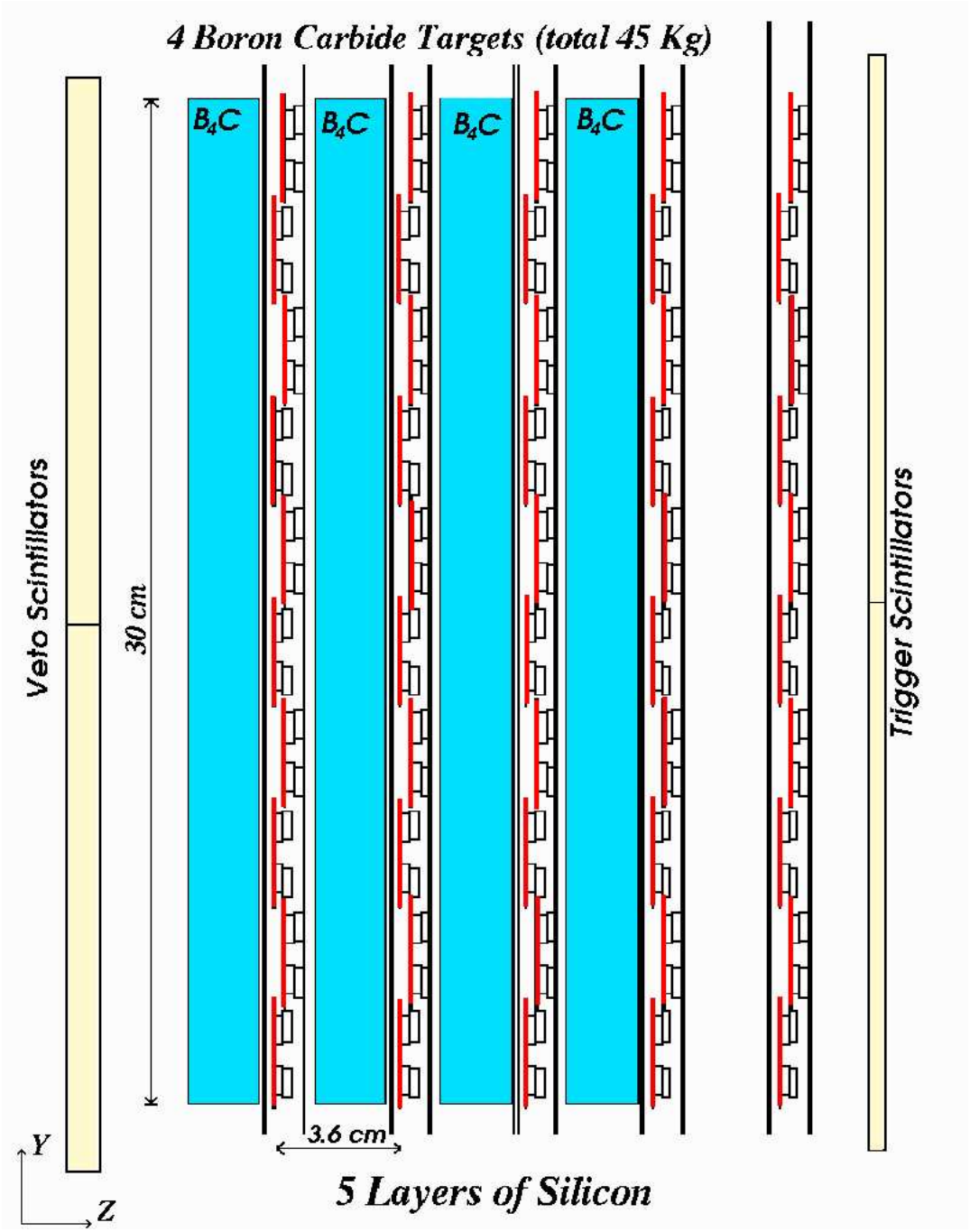

Figure 4.3: Side view of STAR, showing the four boron carbide and five silicon layers, along with the veto and trigger scintillators. The neutrino beam enters from the left. The staggered layout of the 10 silicon modules forming each silicon layer can be seen, as can the four carbon-fiber rods forming the supporting backbone of each module. The aluminium covers in front of and behind each silicon layer are also shown.

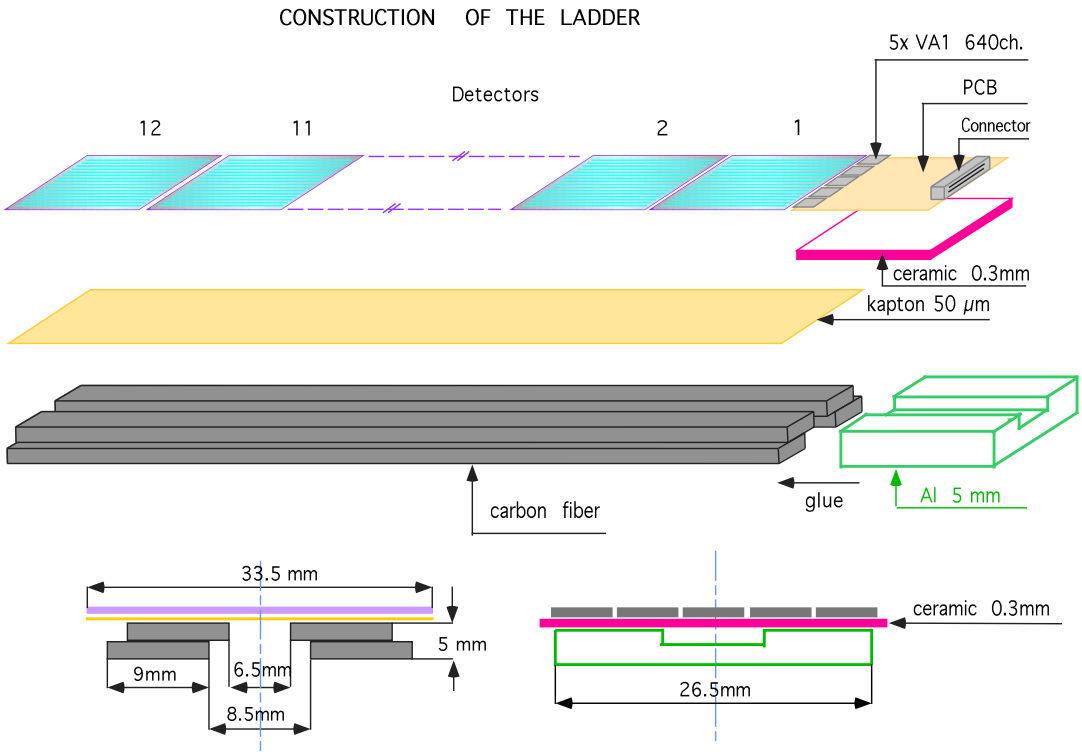

Figure 4.4: STAR module. At the top of the figure, a view of a module showing the individual silicon detectors, kapton foil and the carbon-fiber rods comprising the backbone of the modules can be seen. Also shown are the printed hybrid circuit board with the VA1 chips, along with the ceramic plate and aluminium support they are mounted on. In the bottom of the figure, cross-sectional views of the silicon modules are shown.

completed modules were measured to determine the temporal stability. Also, a radioactive ruthenium source was used to measure the signal-to-noise ratio (S/N) at different bias voltages to define the operational bias voltage. The S/N improves with increasing bias voltage until the detector is fully depleted, after which the S/N stays constant. Furthermore, the noise in all the channels of the completed modules was measured with the noisy channels being identified. A charge pulse applied on the backplane allowed measuring the electrical response of each strip and therefore the identification of short-circuits and interruptions. Finally, as a cross-check, a high-powered, pulsed diode laser was used to scan the modules. The beam was focused to a spot of about 20 μm on the detector surface. As only the strip being hit and the two neighboring ones gave a signal (along with some noisy strips), the response of each individual channel could be measured. The results of these tests occasionally resulted in a readout chip or silicon detector being replaced on a module, or other repairs. The testing procedures are covered extensively in Papers I and II. The construction methods, testing, and quality assurance of silicon detectors are further discussed in Ref. [47]. Many of the methods discussed therein were also used for the NOMAD-STAR modules.

A silicon layer, which is composed of 10 silicon modules, is shown in Fig. 4.5. The silicon modules are alternately staggered, allowing an overlap of neighboring modules, thus providing coverage of the dead areas at the edges of the detectors. The strips are orientated horizontally in the x direction. Each silicon layer has an active area of 72×32 cm^2, giving a total active silicon area of 1.14 m^2 for the five layers. Each silicon layer is mounted in an aluminium frame with protective front and back covers of thickness 1.0 mm and 0.5 mm, that also serve as Faraday cages for grounding purposes. In order to perform an optical surveying, 143 holes of 1.4 cm diameter were cut into the front cover and later covered with a black plastic to ensure light-tightness. As the power dissipation of each layer is approximately 20 W, the layers need to be water-cooled. Cooling pipes run around the supporting frame of each layer and along the electronics to keep the detector at its normal operating temperature of 22 °C. The layers were also fitted with a laser-alignment system, which however proved unnecessary.

The five silicon and four B_4C layers are placed in a supporting basket. The basket is supported by an arch-shaped aluminium structure hanging from the drift chamber support beam.

Directly in front of STAR, covering the active area, there are two scintillators, each having the dimensions of $90.0 \times 17.0 \times 1.0$ cm^3, forming the veto $\mathbf{V_S}$. The separation between the veto and the first silicon layer is 4.9 cm. Similarly, there are two scintillators directly behind STAR, of dimensions $90.0 \times 17.0 \times 0.5$ cm^3, forming the trigger $\mathbf{T_S}$. In addition, STAR uses the central part of the NOMAD veto, called $\mathbf{V_8}$, and the NOMAD $\mathbf{T_1}$ trigger plane. The STAR triggering condition for neutrino interactions requires that the veto planes do not fire while the trigger planes produce a coincidence, giving $\overline{\mathbf{V}}_8\overline{\mathbf{V}}_S\mathbf{T_S}\mathbf{T_1}$ as the trigger condition. For muon events, a coincidence between all four scintillator planes is required ($\mathbf{V_8}\mathbf{V_S}\mathbf{T_S}\mathbf{T_1}$).

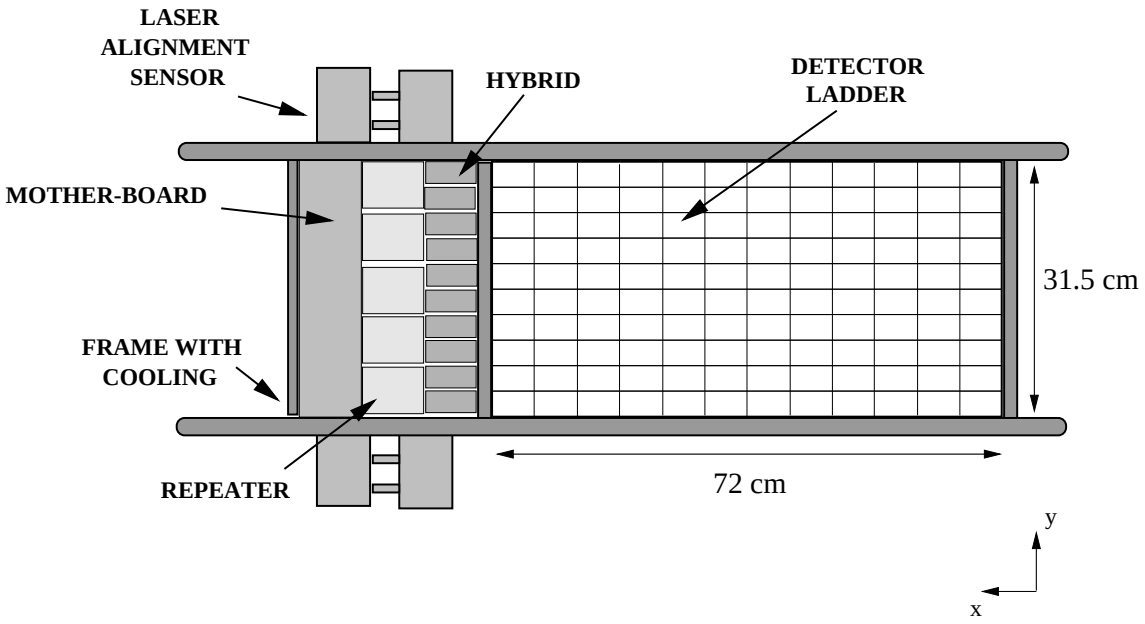

Figure 4.5: STAR silicon layer, comprised of 10 horizontally placed silicon modules or ladders, seen from the front. The neutrino beam goes into the plane of the figure.

A full description of the STAR detector can be found in Paper II.

4.4 Hit, Track and Vertex Reconstruction Methods

In this section, the methods and algorithms for the hit, track and vertex reconstruction are discussed, with the results concerning the performance of the detector being presented in Sec. 5.

The STAR configuration only allows for measurements in two dimensions, namely in the y (vertical) and z (along the beam) directions. Furthermore, tracks are built using information from a maximum of five layers if the primary neutrino interaction occurs in the first B_4C layer, while if the interaction occurs in the fourth B_4C layer, only two silicon planes are available for track reconstruction. Further difficulties are introduced by the multiple scattering and energy loss occurring in the large amount of material traversed by each particle, due to both the B_4C plates and the STAR support structures, such as the carbon-fiber rods.

In order to perform the hit reconstruction, the noise of each individual channel has to be established. First the base level, or pedestal, of each channel is obtained. The pedestals are the average readout values in the channels when there are no hits in that region of the detector. For an individual measurement of the pedestals, however, it is assumed that there is a common change in the readout values of all the channels on a readout chip. The average jump in the signal level for the channels on the chip in an individual event is referred to as the common-mode noise. The noise is now defined as the fluctuation of the channel readout value (in the absence of hits) around

the pedestal value after subtraction of the common-mode noise.

The position of each hit is calculated using the charge-sharing model "Algorithm C", described in detail in Paper I. The charge-sharing model assumes interstrip and backplane capacitances. Instead of a strip retaining all the charge deposited on it, some of it is passed to the neighboring strips or the backplane through capacitive coupling. Eight readout strips and the adjacent floating strips are considered. It is further assumed that for the readout strips the capacitive coupling to the amplifiers is much larger than that to the backplane and that the floating strips do not retain any charge.

The cluster of strips sharing the charge resulting from a charged particle traversing the detector has to be identified. The readout strip that has the highest charge is taken as the seed strip, provided its signal is greater than a given multiple of its noise. This is the seed cut. Neighboring strips are added to the cluster if their signals are beyond a second threshold value, the neighbor cut. Finally, the hit is formed if the sum of the S/N values of the strips in the cluster exceeds a third threshold value, the cluster cut. The S/N of the hit is then defined as the sum of the S/N values of the strips in the cluster. The cluster-forming algorithm is shown in Fig. 4.6.

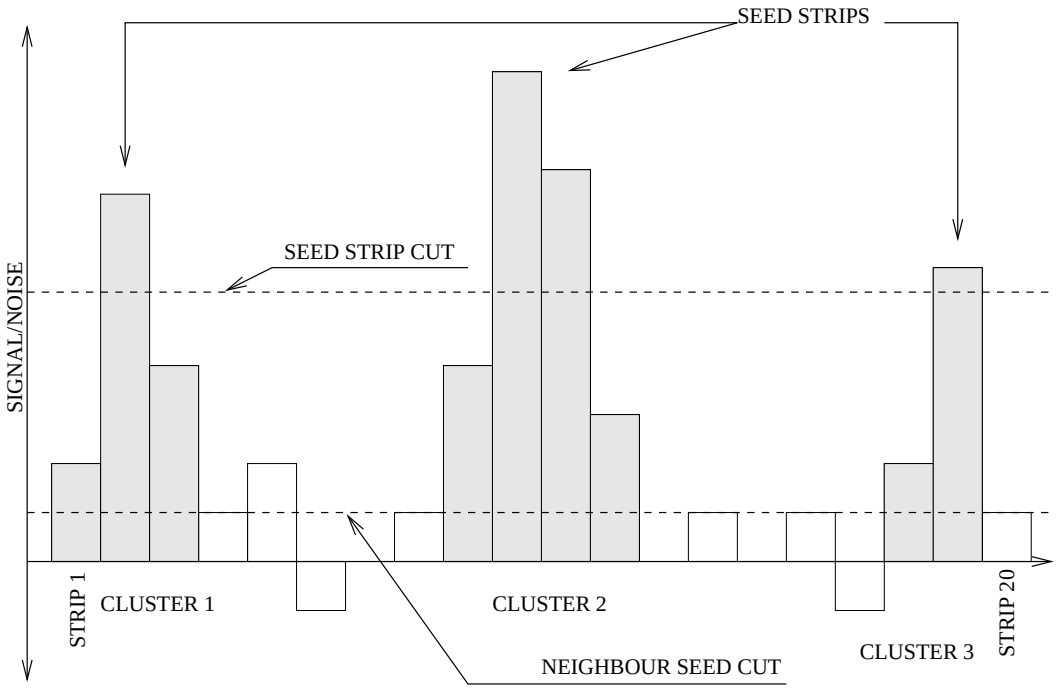

Figure 4.6: Illustration of the cluster search algorithm.

The hits are assigned to tracks in STAR by extrapolating a DC track backwards into STAR. The DC track is required to have a reconstructed momentum of at least 150 MeV (in the system of natural units). Hits within a certain roadwidth, which depends on the track momentum, are selected for the track. A STAR track is built if there are at least two hits along the path of the track and at most one silicon

plane not containing a hit (a gap). However, further gaps are allowed if a track passes through or close to inactive areas in the detector. Each hit can be attached to only one track. Apart from using the total momentum provided by the DC, the STAR track is reconstructed using only the assigned STAR hits. Some further information on the STAR track can be obtained from its corresponding DC track. These include its approximate x position or information on the particle type. The x position information is important as it allows the identification of the individual detector that the track passes through. The hit position can then be refined by using the alignment information of the individual detector concerned. The alignment is described in Sec. 5.2.

A Kalman filtering technique is used for the track fitting. A Kalman filter [48] is an iterative fitting procedure which is mathematically equivalent to a least-squares fit with the advantage that it is computationally less intensive. The Kalman filter takes as input measurements the hit positions and accounts for multiple scattering and energy loss. In the absence of material, the trajectory of a particle in the yz plane of STAR is circular due to the magnetic field. The trajectory is approximated with a Taylor expansion, in which the cubic term is retained to ensure that the tracking accuracy remains better than the intrinsic silicon resolution of approximately 5 μm. The track reconstruction uses general NOMAD reconstruction packages as a basis. However, these have been modified for use by STAR.

Once the STAR tracks have been reconstructed, a primary vertex is built. For neutrino events (as opposed to antineutrino events), the highest-momentum negative muon is selected as the seed track. If there are none, the highest-momentum negative track is used. If there are no negative tracks at all, the highest-momentum positive track is used. The procedure for antineutrino runs is the same except that tracks of the opposite charge are considered. Next, the crossing points of the seed track and the other tracks are found. The impact parameters for all the other tracks relative to each of these vertex position estimates are then found. The combination of tracks that gives the highest number of tracks within 250 μm is used to build the primary vertex. The primary vertex position is determined using a variant of the track fitting Kalman filter in which the track parameters, instead of the hit positions, are the input measurements.

The procedure for track and vertex reconstruction is described in detail in Paper III.

4.5 The STAR Monte Carlo Simulation

The detector was simulated using the GENOM program [49], which is based on the general purpose simulation package GEANT [50]. GENOM is the implementation of the NOMAD detector in GEANT and was modified to include STAR.

The fiducial volume of STAR as well as the regions directly in front of or behind the fiducial volume are implemented in detail in the Monte Carlo simulation. The B_4C targets and the 600 silicon detectors are positioned individually. Each of the

carbon-fiber supports for the modules are implemented as four separate pieces, following their actual geometry. The aluminium covers, located in front of and behind each silicon layer, have been implemented without the holes which were used for the optical alignment survey. The scintillators for the veto and trigger systems have been included. However, some of the support structure has not been included.

All the individual pieces are placed in their nominal positions relative to each other. The global position of STAR within NOMAD, as found by an optical survey, is used in the simulation. Although no uncertainty in the positions of the individual silicon detectors has been directly implemented into the simulation, the same effect is achieved by smearing the positions of the silicon detectors for the reconstruction, using the distributions of the residuals found in the alignment procedure.

The positions of tracks passing through only the active areas in the silicon are considered. The detector response to these "raw hits" is simulated next in a process called "digitization". For STAR, the charge recorded by the analog-to-digital converters (ADC's) for each strip is simulated. The charge is expressed in ADC units, with one ADC unit corresponding to approximately 250 e^-. Specifically, the pedestal-subtracted and noise-smeared ADC values for each strip are given.

The digitization algorithm is based on data obtained from test beam experiments of silicon module prototypes, see Paper I, and from muons passing through STAR during the data-taking. Charged particles traversing the detector deposit charge according to a Landau distribution with a peak value of approximately 100 ADC counts. The charge is shared among several readout strips, taking into account the interstrip and backplane capacitances. The noise is assumed to have a Gaussian distribution, which is centered at zero and has a standard deviation of 6 ADC counts. The common-mode noise is not simulated.

The charge-sharing model is based on two parameters: the interstrip and backplane capacitances. In the first step, the total charge deposited is shared between the nearest readout and floating strips, with the charge split in proportion to the distance of the hit from the strips. In the next step, 70 % of the charge on the readout strip is stored, while 15 % is passed to each of the neighboring floating strips. Of the charge on the floating strips, 5 % is passed to the backplane and is lost, while the rest of the charge is distributed evenly between the two neighboring readout strips. This is then repeated iteratively eight times, which is when the contribution to the readout charge is deemed negligible. The total charge which is read out for a strip is the total charge which is stored on the strip.

In order to produce events in STAR, the neutrino beam has to be simulated and the neutrino interactions have to be generated. The beam was simulated using GEANT based programs called NUBEAM (developed by the NOMAD and CHORUS collaborations) and FLUKA [51]. NUBEAM is responsible for the particle transport while FLUKA simulates proton collisions. The events in NOMAD are generated using NEGLIB [52]. NEGLIB is based on the LEPTO [53] and JETSET [54] packages. LEPTO simulates lepton-nucleon scattering events while JETSET simulates the fragmentation, which is the process by which the partons (gluons and quarks) form

bound states following an interaction. Some 70 000 ν_μ charged-current and 20 400 neutral-current Monte Carlo events were produced.

5 STAR Performance

This section describes the performance of the STAR detector. First the noise performance and hit-finding efficiency are discussed, followed by a description of the alignment procedure for the detector. Next, a search for K^0_S particles is presented. This search is then used to obtain the primary, secondary, and double vertex resolutions of the detector. Finally, the impact parameter resolution is obtained. It should be noted that the results have been obtained using the 1998 data. Most of the data for 1997 was lost due to a triggering error. When the relative timing of the trigger planes was established, cosmic particles traversing opposite to the direction of the beam (backward-going) were inadvertently used and the trigger timing-window did not accomodate most forward-going particles in the beam.

5.1 Noise Performance and Hit-finding Efficiency

Paper I discusses the various noise sources of the STAR modules, as described by a simple mathematical model. Some of the associated measurements are discussed in Papers I and II. The most dominant noise contribution was found to arise from the resistance of the metal strip. The noise contribution due to the readout chip was also found to be significant. Less significant was the noise due to the polarization resistors (detector bias resistors and preamplifier feedback resistors). With leakage currents below 100 nA for most individual detectors, the theoretical prediction for the noise level due to the leakage current was found to be the least significant of the noise sources considered.

The noise is defined as the root-mean-square fluctuation of the readout signal around the base value, or pedestal, after common-mode noise subtraction when there is no signal due to hits. The various definitions for the noise have already been discussed in Sec. 4.4. The production of the noise files necessary for the hit reconstruction is discussed in detail in Paper IV. The files are produced offline on a day-by-day basis for the 1998 data set for each of the 32 000 channels using muon events. Muon events are convenient as typically thousands were recorded each day and they contained few tracks that would interfere with the noise calculations.

The strips on a chip tend to show similar noise behaviour, thus justifying the study of the noise behavior on the chip level. Chips on the same ladder also exhibit similar behaviour. The chip noise is defined as $\sqrt{\frac{\sum_{i=1}^{128} N_i^2}{128}}$, where N_i is the noise of the ith strip on the chip. The distribution of the average chip noise for 1998 is shown on the left-hand side of Fig. 5.1. The distribution is centered at approximately 6 ADC counts (approximately 1 500 e^-). However, 49 chips have a noise level in excess of 8 ADC counts, corresponding to chips displaying unstable noise behaviour. Finally the ladder noise, defined in a manner similar to the chip noise, is shown on the right-hand

side of Fig. 5.1. In particular, layers 3 and 4 have ladders with high noise.

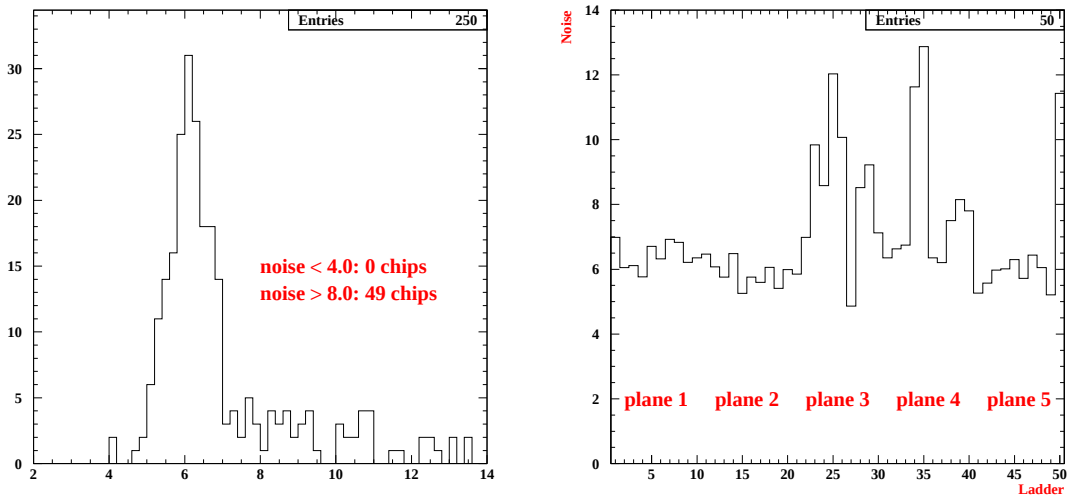

Figure 5.1: Left: the distribution of average chip noise. Right: the average noise is shown ladder-by-ladder.

The studies on the hit-finding efficiency are performed using the reconstructed muon events and they are calculated on a ladder-by-ladder basis. The tracks are required to pass through the active region of the same corresponding ladder in each layer, e.g., the third ladder of each layer. This implies that the muon tracks should be rectilinear and, therefore, only muons with a momentum larger than 10 GeV are selected. When the muon track is reconstructed, a hit is required in each of the four ladders which are not under study. For example, if the third ladder of the first plane is under study, a hit is required in the third ladder of the planes 2, 3, 4 and 5. The area within 1 mm of the extrapolated (or interpolated) hit position of the muon track to the ladder under study is considered for hits. The hit-finding efficiency is defined as the ratio of the number of times at least one hit is found to the total number of muon tracks considered.

The efficiency is maximized by optimizing the S/N cuts, which were discussed in Sec. 4.4. This is done by first maximizing the single-hit efficiency for the seed cut, while setting the neighbor cut to 0.5 and ignoring the cluster cut. This means that for every ladder, the seed cut was optimized such that the efficiency to find exactly one strip passing the seed cut within the 1 mm roadwidth was maximized. Next, the seed cut and the fixed neighbor cut of 0.5 were retained and the efficiency is maximized by varying the cluster cut. This resulted in seed cuts for the ladders which varied from 3.4 to 4.4, with a median value of 3.9, while the cluster cuts varied from 3.8 to 6.1, with a median value of 4.8. The seed and cluster cuts are shown ladderwise on the left-hand side of Fig. 5.2.

The overall efficiency resulting from the optimized cuts is shown on the right-hand

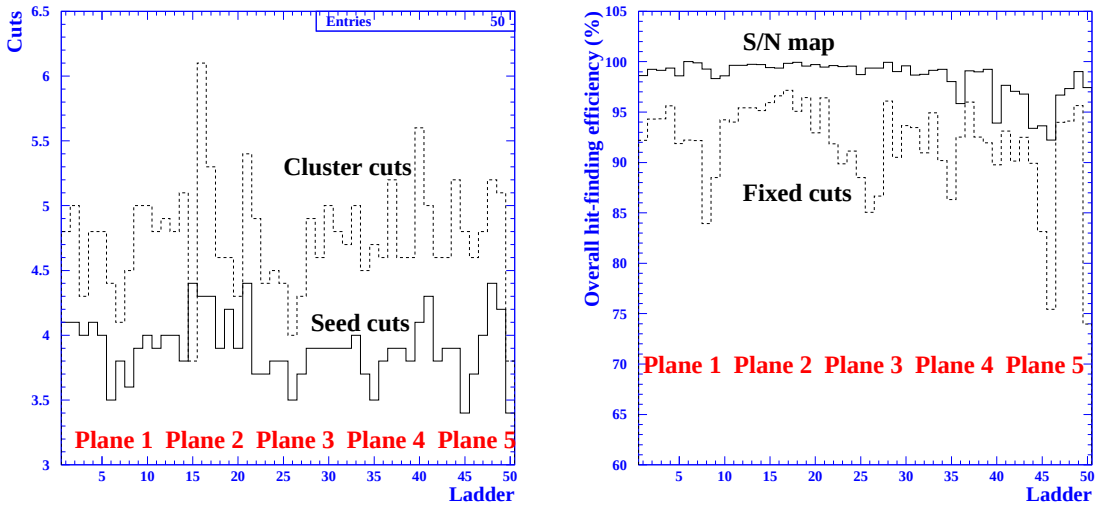

Figure 5.2: Left: the seed and cluster cuts by ladder, where the solid line corresponds to the seed cut and the dashed line to the cluster cut. Right: the overall hit-finding efficiency by ladder for optimized and fixed S/N cuts, where the solid line corresponds to the optimized cuts and the dashed line to fixed cuts.

side of Fig. 5.2. Planes 2 and 3 attain a level of nearly 100 %, with plane 1 nearly at this level. The performance of the ladders in planes 4 and 5 is somewhat weaker, with efficiencies dropping below 95 % for four ladders. It is not surprising that plane 1 does not show optimum performance as this is where the *a priori* poorest ladders were placed during the construction. The weaker performance of some of the ladders can be traced to calibration errors of the electronics, as further discussed in Paper IV. As a comparison, the overall efficiency is also shown with all ladders using fixed cuts of 4.0, 0.5 and 7.5 for the seed, neighbor and cluster cuts, respectively (these were the default cut values suggested by laboratory trials before it was decided to perform the ladderwise optimization). The efficiencies for these are considerably lower, and more importantly, there are considerable fluctuations. The fluctuations suggest different gains of the amplifiers on the ladder, justifying the approach of optimizing the cuts individually for each ladder.

5.2 Detector Alignment

The alignment of STAR is crucial in order to achieve high spatial resolution. As the first step, the positions of each of the 600 individual silicon detectors were surveyed optically in the laboratory. This information served as an input for the next step in the alignment procedure, which was performed using energetic muons traversing the detector. This constitutes a software alignment of the detector. The muons were obtained from the SPS and selected using the muon trigger.

The optical survey was performed using a CCD camera with magnifying optics mounted on a measuring table. The camera could be moved independently along the three axial directions. Initially, the survey was performed separately for each layer of silicon, with four points on each individual detector being measured. The systematic uncertainties of the detector positions in the x, y and z positions were found to have tolerances of 6 μm, 7 μm and 14 μm. The survey was performed again after installing each layer into the supporting basket. This degraded the resolution in the z position to 31 μm, keeping the uncertainties in the x and y positions unaltered. The optical survey is described in Papers II and III and a full description can be found in Ref. [55].

The alignment using the muons was performed independently for the xy projection and the projection involving the z coordinate. The xy alignment was accomplished using high-momentum muons at small angles. The momenta were larger than 50 GeV (in the natural system of units), with the angles being within 0.5° of the horizontal direction (along the z axis). For the purposes of the alignment, the silicon detectors were assumed to be contained in the xy plane and the muons were assumed to be perpendicular to that plane. The error incurred due to these assumptions is negligible compared to the intrinsic silicon resolution of approximately 5 μm. The three parameters which describe the position of the detector are the x and y position of the detector and the rotation of the detector within the xy plane.

As the muons that are available for the alignment are mostly perpendicular to the silicon planes, the information on the z position of the detectors is minimal. Therefore, large-angle muons (pointing downwards from the horizontal direction between 2.5° and 10°) were used, which implies low momenta (below 40 GeV). The parameters now considered are two angles describing the rotation of the detector and a spatial coordinate describing the shift along the z axis from its nominal position.

The alignment was performed by minimizing the residuals in the positions of the ladders. Here the residual is defined as the difference between the predicted position of a hit and the measured position as given by the response of the detector. The predicted position of the hit is the extrapolation of the muon track to the silicon plane under study without including the hit in that plane, as obtained from the Kalman filter. Figure 5.3 shows the residuals after the alignment.

The error in the residuals is 9 μm for the three inner planes (planes 2–4) and 12 μm for the two outer planes (planes 1 and 5). This difference is an effect of the Kalman filter, since for the inner planes there is information from both sides to predict the positions of the hits. However, for the outermost planes, information is only available from one side. The error is mainly due to multiple scattering. A description of the alignment using muons is found in Paper III with a full description in Ref. [56].

5.3 Observation of K^0_S Decays

A search in STAR for K^0_S particles through their decay into $\pi^+\pi^-$ was conducted. A full description can be found in Paper V. The branching ratio for this decay is 68.68 $\pm$ 0.28 %. In addition, there are $\pi^0\pi^0$ decays with a branching ratio of

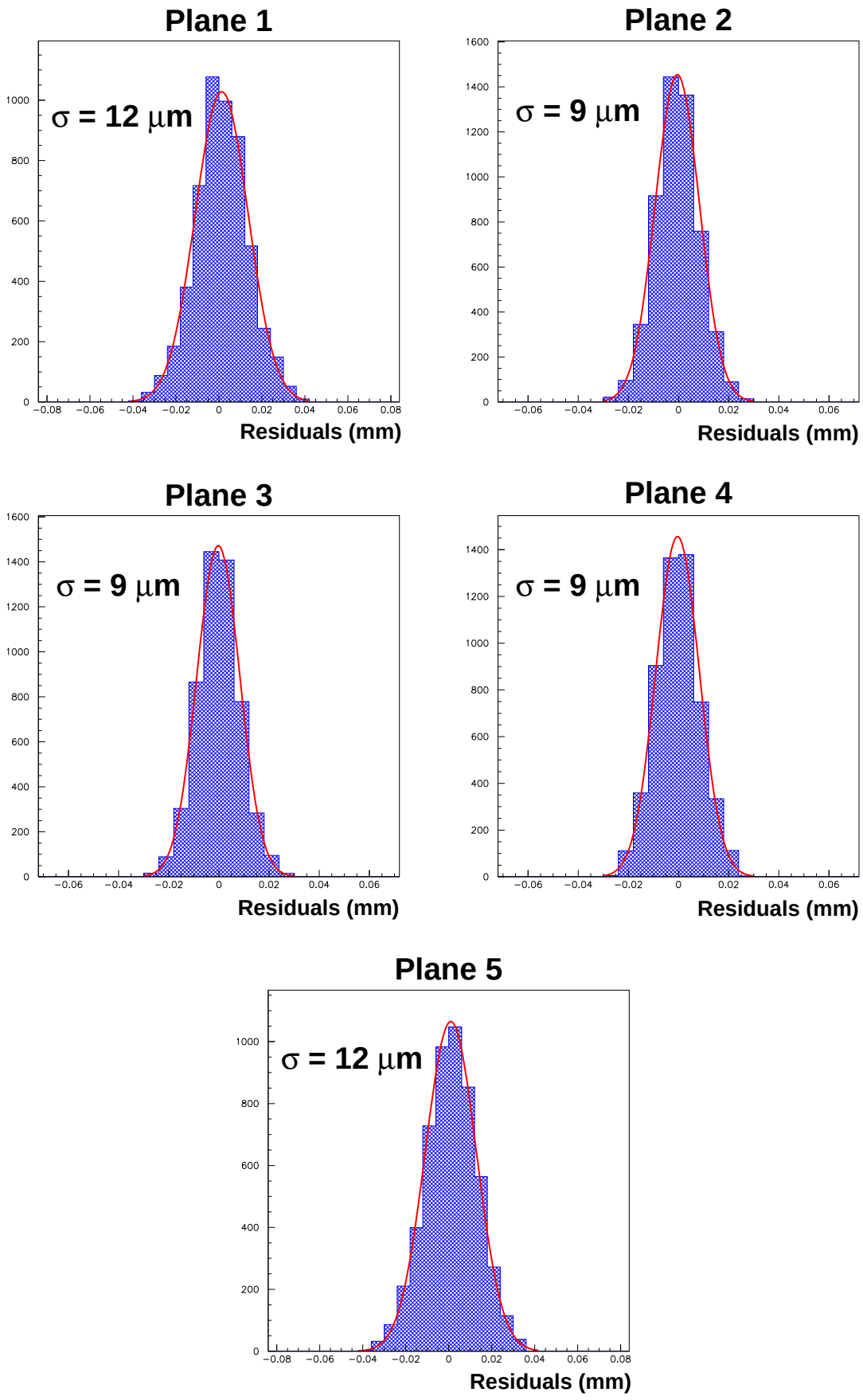

Figure 5.3: Distribution of muon track residuals after the alignment.

$31.39 \pm 0.28\,\%$, as well as some rarely occurring decays [1]. It should be noted that searches in STAR are limited to short-lived particles, as the particles have to be produced and they also have to decay within STAR. In the z direction (along the beam), the fiducial volume spans from the first B_4C layer up to the fourth silicon layer, a distance of 14 cm. Hits in at least two planes are required for track-building, hence interactions occurring after the fourth silicon plane cannot be used.

For this analysis, only those tracks reconstructed by STAR which are not attached to the primary vertex are used. These are called free tracks. Initially, every pairing of a positive and negative free track is considered as a potential K^0_S decay candidate and is termed a track pair. Only events containing a reconstructed primary vertex (with at least two reconstructed STAR tracks) and at least one free positive and one free negative reconstructed STAR track can yield data on reconstructed K^0_S particles. These events are refered to as "2+1+1"-events even if there are more than the minimum required number of tracks in the primary vertex or more than the minimum required number of free tracks.

In the Monte Carlo simulation, a free track originating from a K^0_S decay is considered a signal track, while all the other free tracks are background. A track pair is defined as signal if both of the tracks originate from the same K^0_S. The combinations of a signal track and a background track, or even two signal tracks from different K^0_S particles, form a background pair.

5.3.1 Experimental and Simulated Data Samples

The experimental data sample consists of the entire 1998 data set of 11 527 filtered events. The filter sifted through more than 400 000 events recording a STAR neutrino trigger, requiring a primary vertex reconstructed by STAR. Of these, 10 942 occurred within the STAR fiducial volume, while 2 604 were of the "2+1+1"-configuration. The Monte Carlo sample is composed of ν_μ charged-current and neutral-current events. As the predicted fluxes of ν_e's and antineutrinos for all flavors in the beam are small, as discussed in Sec. 3.1, these were considered negligible in this study and were not included in the Monte Carlo sample. Likewise, quasi-elastic events were not simulated, given their low probability of generating events of the required "2+1+1"-configuration. Normalizing the CC and NC samples in the correct ratio gives a total of 81 965 simulated events. Of these, 71 698 contain a reconstructed primary vertex, of which 24 096 are "2+1+1"-events. The number of events in the experimental and simulated data samples are shown in Table 5.1.

The ratio of experimental to simulated data events is 0.153 when comparing events with a reconstructed primary vertex and 0.108 for the events of the "2+1+1"-configuration. This suggests a difference in the track multiplicities between the experimental and simulated data. The 4 592 positive and 3 696 negative free tracks in the experimental data give an average free track multiplicity of 3.2 per event for the "2+1+1"-configuration. The Monte Carlo data contains 47 901 positive and 38 486 negative free tracks, yielding an average free track multiplicity of 3.6 for the "2+1+1"-configuration. Furthermore, the Monte Carlo sample contains 3.3 track

Selection criterion	Data	MC	Data:MC
Total events	11 527	81 965	0.141
Reconstructed primary	10 942	71 698	0.153
"2+1+1"	2 604	24 096	0.108
Total + / - free tracks	4 592 / 3 696	47 901 / 38 486	0.096 / 0.096
+ / - signal tracks	-	764 / 806	-
+ / - background tracks	-	47 137 / 37 680	-
Total track pairs	6 714	80 180	0.084
Signal track pairs	-	342	-
Background track pairs	-	79 838	-

Table 5.1: Simulated and experimental data samples.

pairs per event, while the experimental sample only contains 2.6 pairs. The discrepancies between the simulated and experimental data point to differences in the track reconstruction, although it is well-known in NOMAD that the hadronization is not accurately simulated. The fine-tuning of the hadronization is a laborious process which is still going on in NOMAD. The fact that there are approximately 20 % less free negative tracks than positive tracks simply reflects the ratio of positive to negative tracks in the hadron shower for ν_μ CC events.

The analysis of the Monte Carlo sample is performed separately for the signal and background samples due to difficulties in the normalization, arising from the different track multiplicities. The total number of surviving signal track pairs in the Monte Carlo simulation is 342, compared to 79 838 background track pairs.

5.3.2 Reconstruction of K^0_S Particles

In order to better understand the reconstruction of K^0_S particles in STAR, the reconstruction efficiency before the application of selection cuts is studied using the Monte Carlo signal sample. Of the 8 503 K^0_S particles decaying into charged pions, only 2 241 do so within the STAR fiducial volume, as shown in Table 5.2. The efficiency is calculated relative to this number as only these decays are detectable by STAR. Of the resulting decay tracks, 58 % are reconstructed by the drift chambers. As shown in Fig. 5.4, the lost tracks mostly have a momentum below 0.8 GeV. This is explained by the particles having to traverse several centimeters of boron carbide before reaching the drift chambers. It is important to remember that the loss of a DC track implies the loss of a STAR track as the STAR tracks are built using the DC tracks.

Of the reconstructed DC decay tracks, approximately 80 % have corresponding STAR tracks. However, to reconstruct a K^0_S vertex, both the positive and the negative decay pions have to be reconstructed. This requirement reduces the K^0_S sample to 547, yielding a reconstruction efficiency of 24 %. The sample is further reduced to 291 K^0_S particles when both decay tracks are required to be free, i.e., not attached to the primary vertex. Free tracks typically have an impact parameter in excess of

Selection criterion	MC	Efficiency (%)
Total $K^0_S \rightarrow \pi^+\pi^-$	8 503	-
Decay in fiducial volume	2 241	100.0
+ / - DC tracks	1 286 / 1 296	57.4 / 57.8
+ / - STAR tracks	1 032 / 1 038	46.1 / 46.3
Both STAR tracks	547	24.4
+ / - free STAR tracks	739 / 667	33.0 / 29.8
Both STAR tracks free	291	13.0
STAR reconstructed K^0_S	342	-

Table 5.2: Reconstruction efficiency of K^0_S particles in the Monte Carlo simulation.

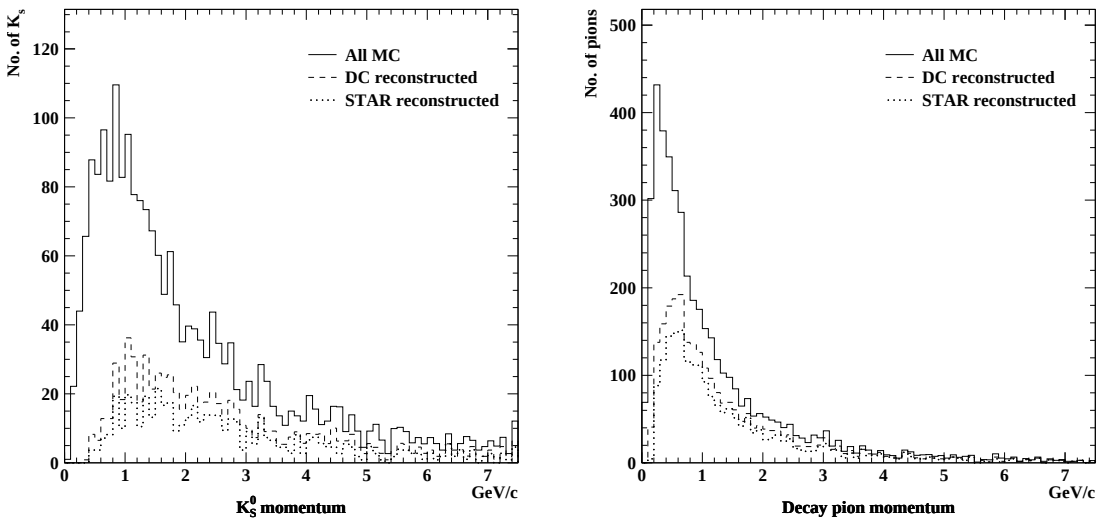

Figure 5.4: Momenta of the K^0_S particles and decay pions. The solid line corresponds to the full simulated MC sample, the dashed line to the particles reconstructed in the DC and the dotted line to particles reconstructed in STAR.

250 μm, see Sec. 4.4 for the details of the vertex reconstruction. These considerations finally result in a reconstruction efficiency of 13 %. It should be noted that as the reconstruction is performed in the yz plane, only information of the decay as a projection onto this plane is available. Therefore, decays occurring in the horizontal plane or close to it would be indistinguishable from the hadron shower and a secondary vertex cannot be built. Furthermore, for events with low multiplicity, the K^0_S decay tracks can mistakenly be used to form the primary vertex, irrespective of the decay plane.

Finally, it should be pointed out that although the normalized Monte Carlo sample has 291 fully reconstructed K^0_S particles, a further 51 decays are reconstructed when the requirement of the decay fiducial volume is lifted on the generated K^0_S position (there were 342 reconstructed decays obtained in the previous section). This was found to be due to hits being incorrectly attached to some tracks. This resulted in the reconstruction of decays actually occurring outside the fiducial volume to be incorrectly reconstructed within the fiducial volume.

5.3.3 The K^0_S Particle Sample

The next aim is to reject background events without rejecting signal events in order to observe a K^0_S signal and to try to extract as pure a sample as possible. Therefore, a number of selection cuts are applied to track pairs and to the individual tracks. Some of the cuts aid in selecting V^0's (neutral particles decaying into two charged particles) in general, while others specifically target K^0_S particles. Some of the selection cuts are quality cuts, in which tracks or track pairs are rejected if the quality of the reconstruction does not pass certain criteria. The Monte Carlo sample is used to ascertain the effect of the cuts on the signal and background.

An important requirement is that for signal decay tracks, there should be no hits upstream of the crossing point of the track pair. However, tracks are sometimes misreconstructed using hits actually belonging to other tracks (or using hits due to noise) in the vicinity of the primary vertex. Therefore, the tracks in a pair are reconstructed again using only the hits downstream from the crossing point. This is done separately for every pairing of tracks, meaning that the same track, depending on which other track it is paired with, could be reconstructed several times with different numbers of hits. A further implication is that some decay track candidates are no longer reconstructed since tracks require at least two hits to be reconstructed. This second reconstruction of the tracks also acts as a fiducial volume cut, as no candidates can be reconstructed downstream of STAR.

In addition to the second reconstruction of the tracks, one of the most important selection cuts is to require the secondary vertex candidate to occur downstream from the primary vertex. Another is checking that the momentum vector of the candidate pair (the vector sum of the momenta of the two tracks forming the pair) appears to come from the direction of the primary vertex. An important cut is performed on the transverse momentum of the positive track with respect to the momentum vector of the track pair candidate, as in a K^0_S decay it is kinematically restricted to 0.206 GeV.

The other cuts on the track pair are on the momentum and lifetime of the candidate K^0_S particle. One of the cuts on the individual tracks use the particle identification of NOMAD to reject electron and muon tracks. Also, tracks are rejected if they appear to come from the primary vertex. Although STAR itself does not measure the x position of tracks, the DC provides some information on this matter. Thus the difference in the x positions of the two decay track candidates at their intersection point in the yz plane is used as a cut. There is also a cut on the momentum ratio of the two tracks as a large asymmetry in the momentum is not expected. Finally, there is a requirement on the quality of the reconstruction of the DC tracks used to build the STAR tracks.

After application of the selection cuts, 97 % of background pairs in the Monte Carlo sample are rejected, leaving 2418 of the original 79838 events. Of the signal pairs, 49 % of the 342 events are retained, leaving 169 events. In the experimental data sample, 2 %, or 141 events, of all pairs remain, from the total number of 6714 events. A full discussion on selecting K^0_S candidates can be found in Paper V.

The invariant mass distributions for the candidates under the pion decay hypothesis before the cuts are shown in Fig. 5.5. There is a difference between the simulated and the experimental data for low invariant masses. This is due to the reconstruction efficiency of low opening angle track pairs in the experimental data being lower than that for the Monte Carlo sample. The invariant mass distribution for the candidates after the selection cuts are shown on the right-hand side of the figure. It displays a distinct mass peak between 0.46 GeV and 0.54 GeV. For the normalization of the Monte Carlo background to the experimental data background, the region from 0.44 GeV to 0.56 GeV was excluded in order to ensure that no K^0_S signal was used in the normalization. The resulting raw normalization factor, obtained by normalizing by area, or track pairs, is 0.043 for the MC background. This may be compared to the normalization factor of 0.108 for the "2+1+1"-events, as shown in Table 5.1. This discrepancy is a result of the different track multiplicities.

In order to verify that the observed mass peak corresponds to K^0_S particles, a Gaussian fit is performed to the peak to obtain the average value and width. The width is a measure of the mass resolution of the detector for this measurement. The fit for the Monte Carlo sample is performed only on signal events passing the selection cuts. For the experimental data, the background has to be taken into account as well. The procedure is to directly fit the data to the shape of the Monte Carlo background which was multiplied by a free scale factor, and a Gaussian for the mass peak. The fits are shown in Fig. 5.6. The mean of the Gaussian for the Monte Carlo signal sample is 0.497 ± 0.001 GeV, while the sigma for the same distribution is 0.018 ± 0.001 GeV. For the experimental data, the values are 0.490 ± 0.006 GeV and 0.021 ± 0.006 GeV, respectively. The scale factor was found to be 0.042 ± 0.005, agreeing very well with the raw normalization factor for the MC background of 0.043 found earlier in this section. The background was also estimated using fourth-order polynomial and spline functions, which produced results nearly identical to the one already quoted. There is close agreement between the MC and experimental data samples. The mass of the

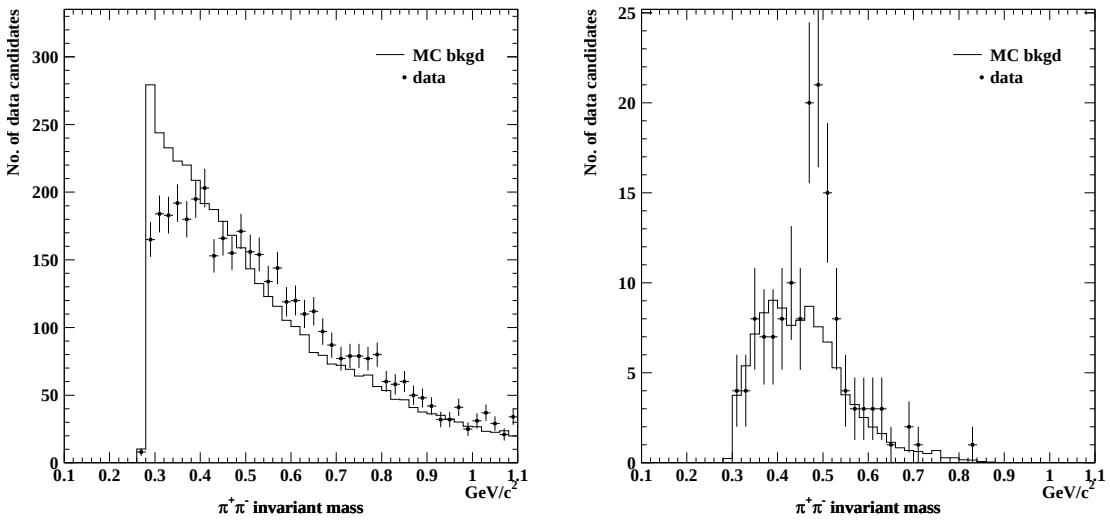

Figure 5.5: Invariant mass for all fully reconstructable track pairs under the pion decay hypothesis. The experimental data is compared to Monte Carlo background before cuts on the left and after cuts on the right.

K^0_S is quoted as 0.497672 ± 0.000031 GeV in Ref. [1].

To find the number of signal decays in the mass peak, the normalized Monte Carlo background sample is used to estimate the background in the experimental data in the mass peak region from 0.46 GeV to 0.54 GeV. The mass peak contains a total of 64 decay candidates, while the estimate for the background gives 29 track pairs. After the evaluation of the statistical error (using the error on the Monte Carlo sample and the error on the normalization), 35 ± 9 K^0_S decays are estimated to be in the experimental sample.

5.4 Vertex and Double Vertex Resolutions

The vertex resolutions of the NOMAD-STAR detector are presented in this section. They are based on Paper V. As the Monte Carlo simulation is used to obtain these results, the first aim is to show that quantities related to the vertex resolutions are accurately simulated. Then the simulated data can be used to obtain the vertex resolutions. These are obtained only for the y and z positions as STAR can only measure in these two directions. The two directions are treated separately.

Comparisons of several variables related to the selection of the K^0_S particles in the simulated and experimental data samples which are not discussed in this section can be found in Paper V. Their close agreement gives further support to the results in this section.

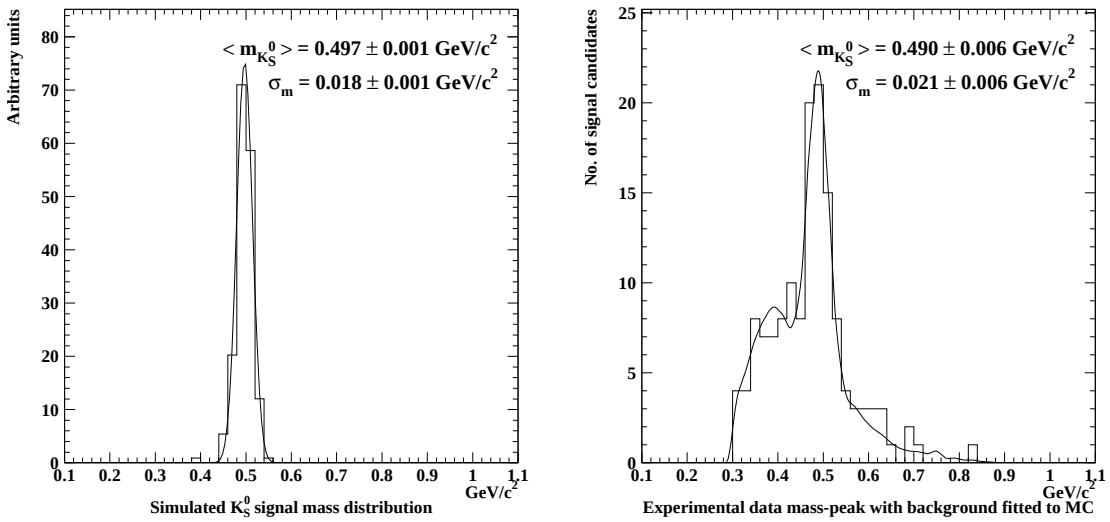

Figure 5.6: Gaussian fits to the peaks in the invariant mass distributions after cuts. On the left, the fit is performed on the K_S^0 signal decays. On the right, the fit is to the mass peak in the experimental data, with an additional fit for the background.

5.4.1 Primary Vertex Resolution

First, the primary vertex is examined. The events are required to be of the "2+1+1"-configuration, i.e., to contain a reconstructed primary vertex, composed of a minimum of two tracks, and also to have at least one positive and one negative free track. The uncertainty in the reconstructed vertex position is defined as the square-root of the covariance matrix element in the position of the vertex as obtained from the vertex fit, see Paper III. This is obtained for both the simulated and experimental data. The results are shown in Fig. 5.7. There is close agreement, providing confidence in the accuracy of the Monte Carlo simulation. The rise in the distribution of the z position uncertainty towards the 500 μm mark is mainly due to poorly reconstructed two-track primary vertices. The abrupt cut-off at 500 μm is a consequence of the initial value of the uncertainty used in the iterative Kalman filtering procedure being too optimistic for the poorly reconstructed vertices. This results in the vertex fit not converging properly.

The error in the reconstructed primary vertex is defined as the distance between the reconstructed and simulated positions for the primary vertex. The error can only be obtained from the simulated data. The distributions for the y and z positions are shown in Fig. 5.8, with the fits to double Gaussian distributions. The principal error distribution is assumed to be Gaussian with an underlying background which is also Gaussian. This background can be seen at the ends of the distributions (the "tails") in the figure. Many of the tracks in these events have low momenta, leading to errors in the track reconstruction due to multiple scattering. These events are further characterized by low track multiplicities and low opening angle primary vertices,

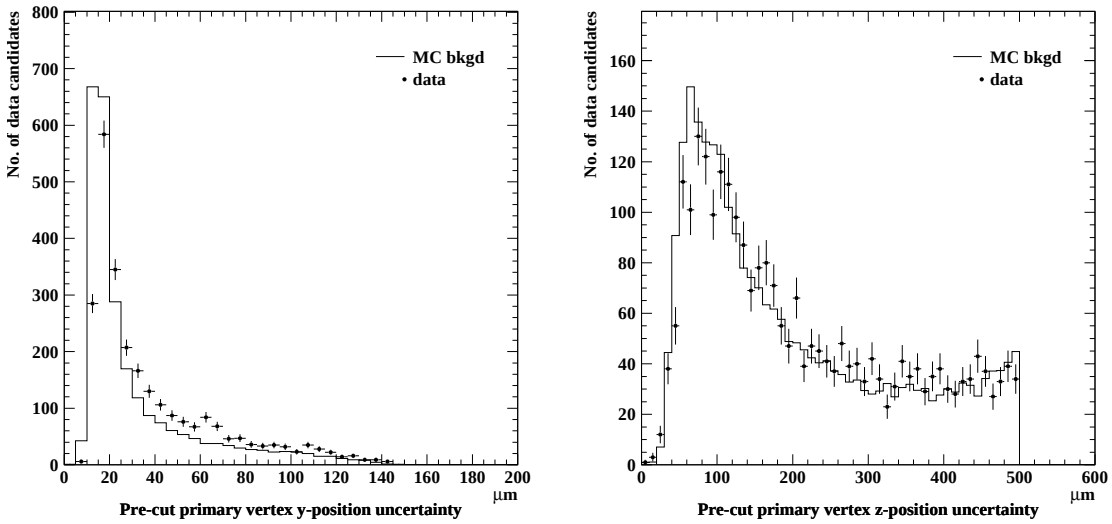

Figure 5.7: Uncertainty in the reconstructed primary vertex position of the "2+1+1"-events for Monte Carlo and experimental data before cuts. The results for the y position are shown on the left and those for the z position on the right.

again leading to inaccuracies in the reconstruction. The fits indicate a resolution of 20.5 ± 0.3 μm for the y position and 108 ± 3 μm for the z position. The errors are statistical. This is in good agreement with the distributions for the uncertainty in the vertex position.

5.4.2 Secondary Vertex Resolution

In this section the secondary vertex resolution is presented. First, the agreement between the simulated and experimental data is ascertained by comparing the uncertainty distributions for track pairs, in a manner similar to the one that was used for the primary vertex. This is done for all decay candidates before selection cuts are applied as otherwise the number of events in both the experimental and simulated data samples is too low for a meaningful comparison. Therefore, as most candidates are not true K^0_S decays, the uncertainty distributions do not directly yield information on the error distributions, as was the case for the primary vertex. Once the agreement between the simulated and experimental data is ascertained, the simulated K^0_S decays which pass the selection cuts are used to obtain the error on the vertex position.

The uncertainties in the y and z positions for track pairs (i.e., secondary vertex candidates) before cuts are shown in Fig. 5.9. The agreement between the y position distributions is very close. The slight discrepancy between the z position distributions is due to the difference in the reconstruction efficiency for track pairs with a low opening angle. As was the case for the primary vertex, the abrupt cut-off at 500 μm in the z position uncertainty is a consequence of the vertexing algorithm.

The distributions for the error on the secondary vertex positions for signal track

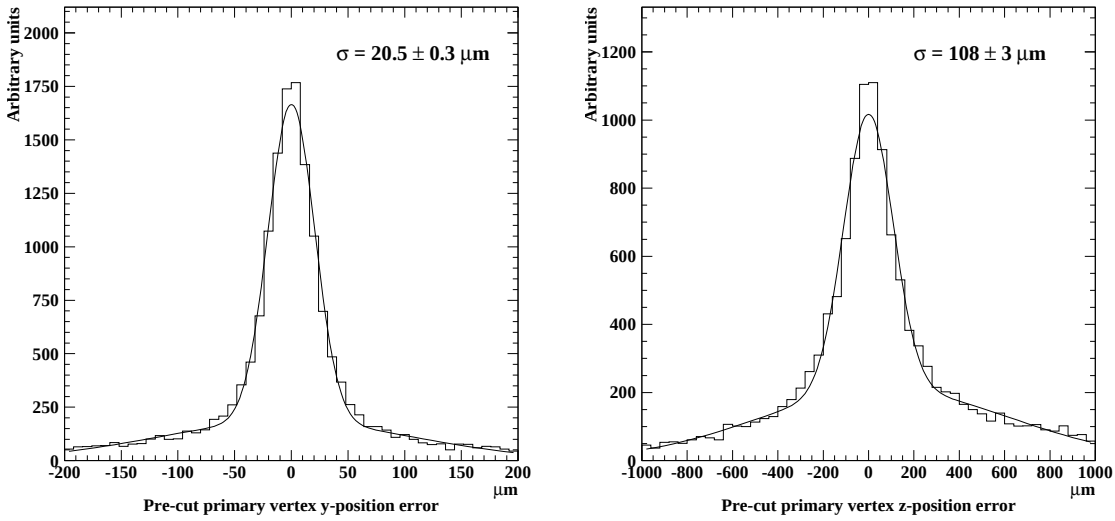

Figure 5.8: Error in reconstructed primary vertex position for "2+1+1"-events for Monte Carlo events before cuts. The fit is to a double Gaussian distribution, with the y position shown on the left and the z position on the right.

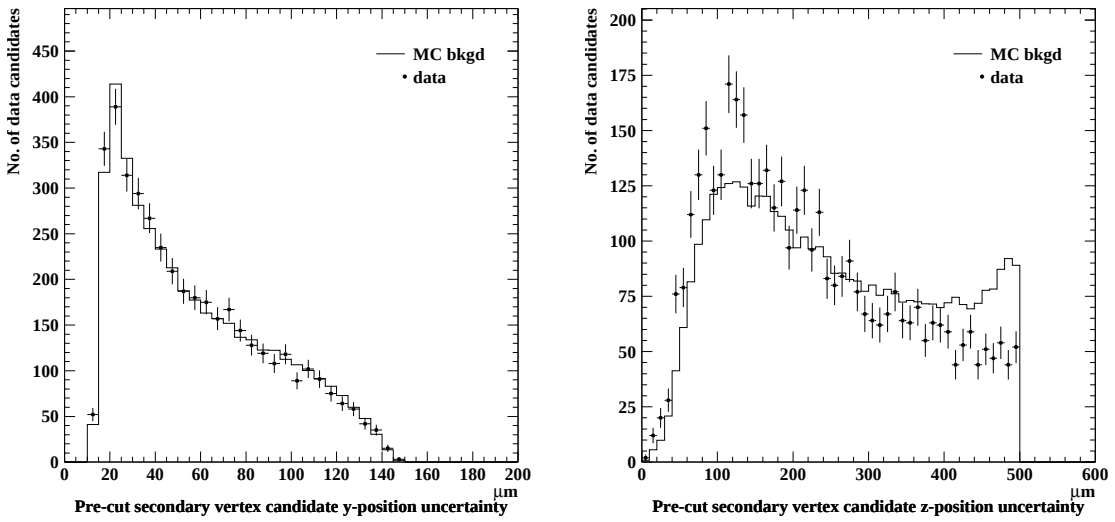

Figure 5.9: Uncertainty in the position for reconstructed secondary vertex candidates before cuts for the y position (lhs) and the z position (rhs).

pairs passing the selection cuts are shown in Fig. 5.10. The fits are to a double Gaussian distribution and they indicate a y position secondary vertex resolution of 19 $\pm$ 6 μm and a z position resolution of 60 $\pm$ 10 μm. These values are slightly improved with respect to those obtained for the primary vertex. This is to be expected as, when reconstructing the K^0_S decays, the information from the Monte Carlo simulation is used to select the correct decay tracks while this is not done when reconstructing the primary vertex. Therefore tracks not originating from the primary interaction may be attached to the primary vertex, decreasing the vertex resolution. The larger statistical errors are a result of the lower number of events available for reconstructing secondary vertices than for primary vertices. It should also be noted, that for all the error resolutions shown, a significant number of entries are at the ends of the distributions. This is true in particular for the secondary z resolution, where over half the events are outside the central Gaussian distribution.

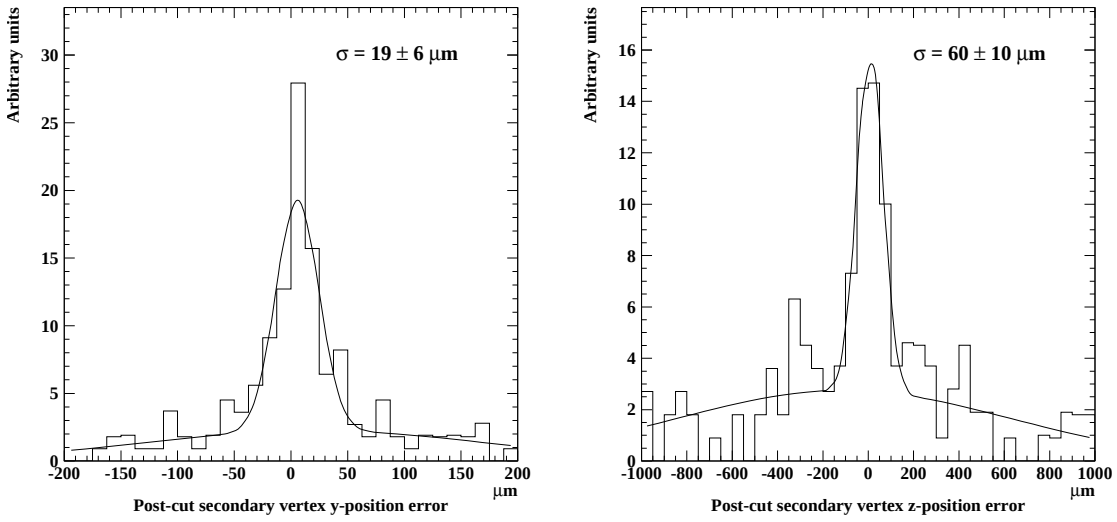

Figure 5.10: Error in position after cuts for reconstructed secondary vertices identified as signal from the Monte Carlo simulation for the y position (lhs) and the z position (rhs). The fits are to double Gaussian distributions.

5.4.3 Double Vertex Resolution

One measure of the STAR vertex resolutions is the accuracy of the reconstructed distance between the primary and secondary vertex (the particle decay distance). The error in the decay distance is the difference between the simulated and reconstructed distances for the simulated events. The double vertex resolution is the sigma of the distribution of the error in the decay distance.

The distribution for the double vertex resolution obtained using the simulated K^0_S decays passing the selection cuts is shown in Fig. 5.11. A fit to a double Gaussian

distribution gives a y resolution of 18 $\pm$ 4 μm and a z resolution of 280 $\pm$ 40 μm. A better result would have been expected for the z resolution based on the primary and secondary vertex resolutions. The discrepancy indicates systematic errors, which are, however, difficult to investigate due to the low number of events in the sample. Also, the central Gaussian peak now contains more events than that for the secondary vertex resolution and therefore the sample used to obtain the double vertex resolution contains more poorly reconstructed events. The anticipated NAUSICAA resolution for the decay length measurement is approximately 100 μm, as discussed in Sec. 4.2. This is better than the STAR double vertex resolution and in agreement with the STAR results based on the primary and secondary vertex resolutions (i.e., their quadratic sum).

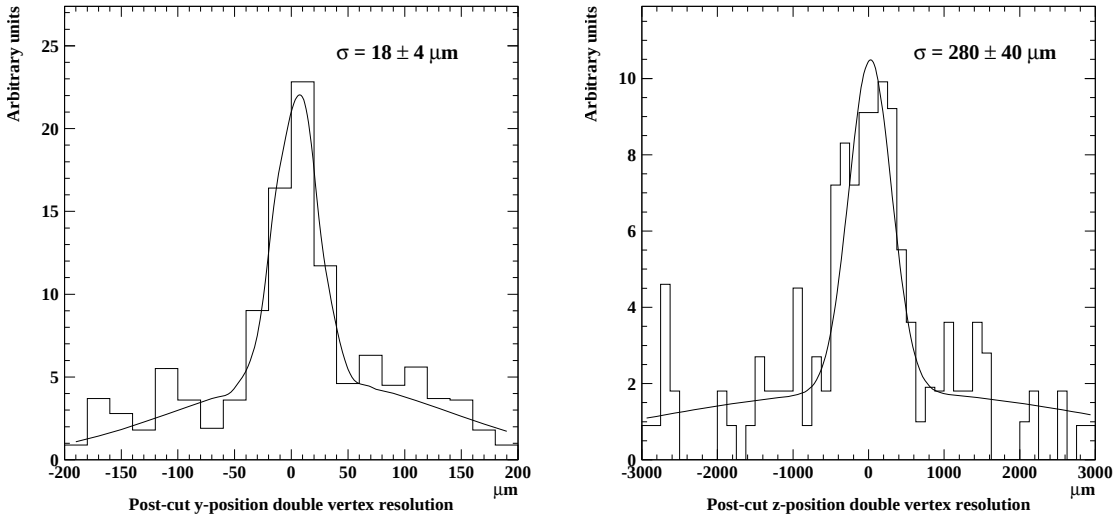

Figure 5.11: Error in the decay distance after cuts for the signal decays obtained from the Monte Carlo simulation for the y position (lhs) and the z position (rhs). The fits are to double Gaussian distributions.

5.5 Impact Parameter

One of the main aims of the STAR project has been to find the impact parameter of the μ^- resulting from a ν_μ CC interaction with respect to the primary vertex. This is discussed in detail in Paper III. In a ν_μ CC interaction, the resulting μ^- and the hadronic jet originate from the same point in space. Ideally, if the μ^- track is removed from the vertex fit, it should still appear to originate from the primary vertex, which is now composed only of the hadronic jet. The impact parameter, already discussed in Sec. 4.2, is here defined as the projected signed distance of closest approach in the yz plane of the μ^- to the primary vertex produced by the remaining hadronic jet.

The first stage in calculating the impact parameter is to construct the primary

interaction vertex. If there is an identified μ^- and two other tracks in the vertex, the μ^- is then removed from the vertex and the vertex is refitted. The μ^- track is then extrapolated to the new vertex position and the impact parameter is determined. To check that the impact parameter and the associated uncertainties have been correctly estimated, the impact parameter significance is used. This is the impact parameter divided by the calculated uncertainty. For ν_μ CC events, a Gaussian distribution with a mean of zero and a width of one is expected.

The results obtained for the impact parameter and impact parameter significance of the ν_μ CC interactions obtained from the STAR 1998 data are shown in Fig. 5.12. The comparison of the data and the ν_μ CC Monte Carlo distributions are in fair agreement. A double Gaussian fit gives an impact parameter of 25 ± 2 μm, while the RMS value is approximately 52 μm. A Gaussian distribution is fitted to the impact parameter significance. It has a mean close to zero and a width of 1.2. The tail of the distribution is attributed to events with two tracks in the primary vertex which have a small opening angle. Imposing that the two tracks have an opening angle of more than 0.2 rad yields the bottom distributions shown in Fig. 5.12. The double Gaussian fit now yields 25 ± 1 μm for the impact parameter. The RMS of the impact parameter is 36 μm and the impact parameter significance is Gaussian with a width of 1.0, which indicates that the errors are being taken into account properly. The RMS of 36 μm is close to the NAUSICAA-value of 28 μm described in Sec. 4.2. The muon momentum spectra for the two cases are comparable as the NAUSICAA neutrino beam is modelled on the same CERN SPS beam used by STAR. Any further remaining differences are probably also due to the limited lever arm of STAR. With only five silicon layers, it often occurs that there are only two or three hits that define a track, while the NAUSICAA design has 10 silicon layers and therefore more hits define a track than in STAR.

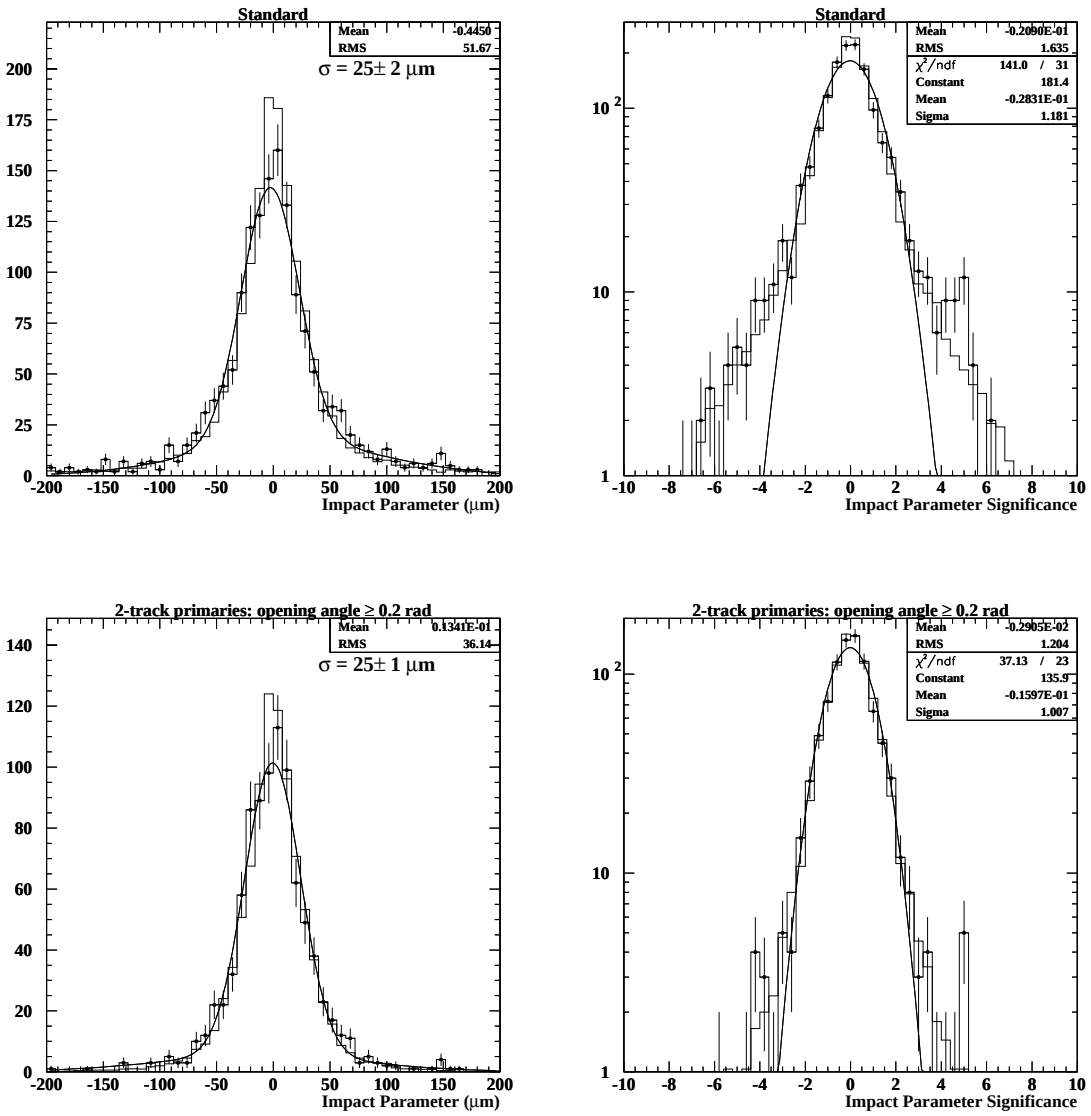

Figure 5.12: Impact parameter distribution (left) and impact parameter significance (right) of ν_μ CC data (points) and Monte Carlo (histogram). The top figures are for all events with two or more tracks in the primary vertex and the bottom figures are cutting out those events with two track primary vertices having an opening angle of less than 0.2 rad. The fits to the impact parameter are to double Gaussian distributions, while those to the impact parameter significance are to Gaussian distributions.

6 Discussion

In the previous section, the performance of STAR has been shown to fulfill the expectations and to make a large-scale silicon detector a viable alternative for a short baseline $\nu_\mu \rightarrow \nu_\tau$ neutrino oscillation experiment. The STAR impact parameter measurement of the μ^- resulting from a ν_μ CC interaction was found to be very close to the value obtained in the NAUSICAA study. The primary and secondary vertex resolutions were similarly encouraging. Only the double vertex resolution along the beam direction was larger than expected, although this measurement was hampered by low statistics.

However, the results of the Super-Kamiokande experiment, shown in Sec. 2.2, suggest that long baseline (hundreds of kilometers) experiments should be used to search for $\nu_\mu \rightarrow \nu_\tau$ oscillations. Therefore, it is unlikely that a detector similar to STAR or NAUSICAA (see Sec. 4.2) will be built for short baseline neutrino experiments. In this section, some of the other prospects for STAR and STAR-like detectors in neutrino physics and related phenomena are considered.

First, a study of charm production by neutrinos in STAR has been carried out, see Ref. [57] for a full account. Charm quarks can be produced in deep inelastic charged-current neutrino interactions. They are mainly bound to D mesons (mesons are composed of a quark-antiquark pair) and have a typical decay length of a few hundred microns in STAR. The study searched for D^0, D^+ and D_S^+ mesons. When a D^0 or a D^+ was found, then an additional search for the excited states D^{0*} and D^{+*} was performed. Taking advantage of the precise tracking and vertex information of STAR, the events were selected based on a constrained topological and kinematical fit. A total of 45 events were found to pass the selection cuts for a reconstructed charmed meson, of which 22 were estimated to be background. Using the Monte Carlo simulation, the reconstruction efficiency for these charmed mesons was found to be close to 4 %. The total production rate was determined to be 7.2 ± 2.4 % in deep inelastic ν_μ CC interactions, in agreement with previous experiments. The results are significant as they show that using the high spatial precision of STAR provides a viable method for studying charmed mesons produced in neutrino interactions.

Considering another use of STAR, an experiment probing $\mu \rightarrow \tau$ conversions on nucleons has been proposed in Ref [58]. In this experiment, STAR could be the instrumented target for the incoming muon beam. As in the case of $\nu_\mu \rightarrow \nu_\tau$ oscillation experiments, the high resolution of silicon detectors is crucial as the resulting τ particle would be observed through its decay.

Using silicon technology to help find and reconstruct tracks in a nuclear emulsion has been tentatively considered, although mainly in conjunction with a short baseline neutrino oscillation experiment. A silicon detector for extrapolating the tracks into a nuclear emulsion was built directly after STAR. The construction of the tracker, the components that were used and the testing and alignment procedures were similar to

those of STAR, with a full discussion available in Paper VI. The tracker consists of 72 of the same single-sided silicon detectors as were used in STAR, yielding a total surface area of 0.13 m^2. It was installed in a pion beam produced by the CERN Proton Synchrotron (PS). The detectors are distributed over four layers, perpendicular to the beam, with the beam coinciding with the z axis. The layers provide two x and two y coordinate measurements, thus allowing three-dimensional tracking for each charged particle. Each layer consists of six modules similar in design to those of STAR, however consisting of only three detectors, to give a length of 18 cm. For these short modules, the dominant noise source was determined to be the readout chips. The results of the silicon-emulsion experiment proved inconclusive as whenever there were multiple tracks or spurious noise, the combinatorial possibilities in assigning hits to tracks made extrapolating the silicon tracks into the emulsion difficult. However, the performance of the silicon modules themselves represents a clear improvement over that of the STAR modules through the experience gained in constructing STAR. There were less defective channels (0.2 % compared to 1.4 %) due to better trouble-shooting. The optical alignment was more accurate as the setup was better understood, with the tolerances of 6 μm in the x direction and 7 μm in the y direction for STAR approximately halved. The readout electronics were improved, resulting in better noise performance and a signal-to-noise ratio of 60 for a typical module, compared to 16 for STAR (although the improvement in the S/N is mainly ascribed to the shorter length of the tracker modules).

The possibility of using the decays of muons in a storage ring (an accelerator which stores particles instead of colliding them) as a high-flux source of neutrinos has been widely discussed. Such a neutrino source, or "factory", would be ideal for the long baseline neutrino oscillation experiments suggested by the Super-Kamiokande results. Such experiments would also provide an opportunity for a near-detector for high-rate studies of neutrino interactions, as outlined in Ref. [59]. In this context, a near-detector using silicon technology would be a viable prospect and the experience obtained with STAR could be useful. If STAR were part of the near-detector for a neutrino factory, approximately one million charm events could be reconstructed per year, as calculated in Ref. [57]. Such a sample would allow for the precise determination of the charm production cross-section and an improvement in the determination of the V_{cd} parameter of the quark mixing matrix. The V_{cd} parameter is a measure of the strength of the coupling between the W boson, charm quark and down quark participating in the interaction. The neutrino factory and a STAR-like detector could also serve to search for $D^0 - \overline{D}^0$ mixing, and CP violation (which implies an asymmetry in interactions under simultaneous particle-antiparticle interchange and space inversion) with charmed mesons.

7 Summary

The work covered in this Thesis mainly concerns the NOMAD-STAR prototype silicon microstrip detector, which was built to demonstrate the capabilities of a large-area silicon detector for a future $\nu_\mu \rightarrow \nu_\tau$ short baseline neutrino oscillation experiment. STAR was installed into the NOMAD experiment at the CERN SPS neutrino beam for the period 1997–98, recording approximately 10 000 neutrino interactions. STAR consists of 50 modules of silicon detectors arranged in five layers and interleaved by four layers of passive B_4C. With a length of 72 cm, the modules are the longest built to date. The total sensitive silicon surface layer is 1.14 m^2 and contains 32 000 readout channels.

Most modules displayed stable noise behaviour, with an equivalent noise charge of approximately 1500 e^-. The hit-finding efficiency of the modules was maximized by optimizing the clusterization cuts module-by-module. In this way most modules obtained a hit-finding efficiency of close to 100 %, with four modules showing an efficiency below 95 %. The detector was aligned in a two-step process: first, an optical survey was performed, followed by a software alignment using energetic muons. This resulted in alignment residuals of between 9 and 12 μm.

A search for K^0_S particles in STAR was performed to demonstrate the capabilities of the detector. The search yielded 64 K^0_S candidates, with an estimated background of 29. After the evaluation of the statistical error, 35 ± 9 K^0_S decays were estimated to have been observed in the experimental sample. The K^0_S mass was measured to be 0.490 ± 0.006 GeV, in agreement with the world average of 0.498 GeV.

The K^0_S analysis was used to obtain the vertex resolutions of STAR. For the primary vertex, a resolution of 20.5 ± 0.3 μm for the y position and 108 ± 3 μm for the z position was found. The secondary vertex resolutions were found to be 19 ± 6 μm and 60 ± 10 μm for the y and z positions, respectively. The double vertex resolution was 18 ± 4 μm for the y position and 280 ± 40 μm for the z position.

The impact parameter resolution of the μ^- resulting from a ν_μ CC interaction with respect to the primary vertex was found to be 25 ± 1 μm, with close agreement between the experimental and simulated data.

The vertex resolution and impact parameter results show that a STAR-like detector would be well-suited to reconstructing the decays of τ particles. This demonstrates the ability of a silicon detector to measure $\nu_\mu \rightarrow \nu_\tau$ neutrino oscillations.

Finally, it has been shown that silicon technology has several other applications within neutrino physics, such as using a silicon tracker to extrapolate tracks into a nuclear emulsion. Another possibility is to use a silicon detector as the near-detector in a future neutrino factory facility.

Appendix: STAR Event Displays

In this section, graphical views of events (event displays) are shown for both experimental and simulated data. An event from the experimental data is shown at four different magnification levels. The event shows a K_S^0 decay candidate,with the decay occurring approximately 2 cm downstream from the primary neutrino interaction. This is very likely a ν_μ CC event as a track can be seen reaching the muon chambers. A ν_μ CC from the simulated data is also shown at four different magnification levels. Here the K_S^0 decay occurs approximately 3 cm downstream from the primary vertex.

In the event displays, the dashed lines represent neutral particles. If these particles are detected by the electromagnetic calorimeter, they are assigned automatically to the primary vertex. In the magnified STAR views, the dashed line represents the vector between the primary and secondary vertex. The unmatched reconstructed hits in the drift chambers are drawn very large. Therefore the event from the experimental data is not as difficult to reconstruct as may initially seem. The crosses in STAR indicate reconstructed hits matched to tracks, while circles indicate unmatched hits (some of which could be due to spurious noise). In the highly magnified views, the bars shown in conjunction with the STAR hits indicate the reconstructed charge for each strip in the hit cluster.

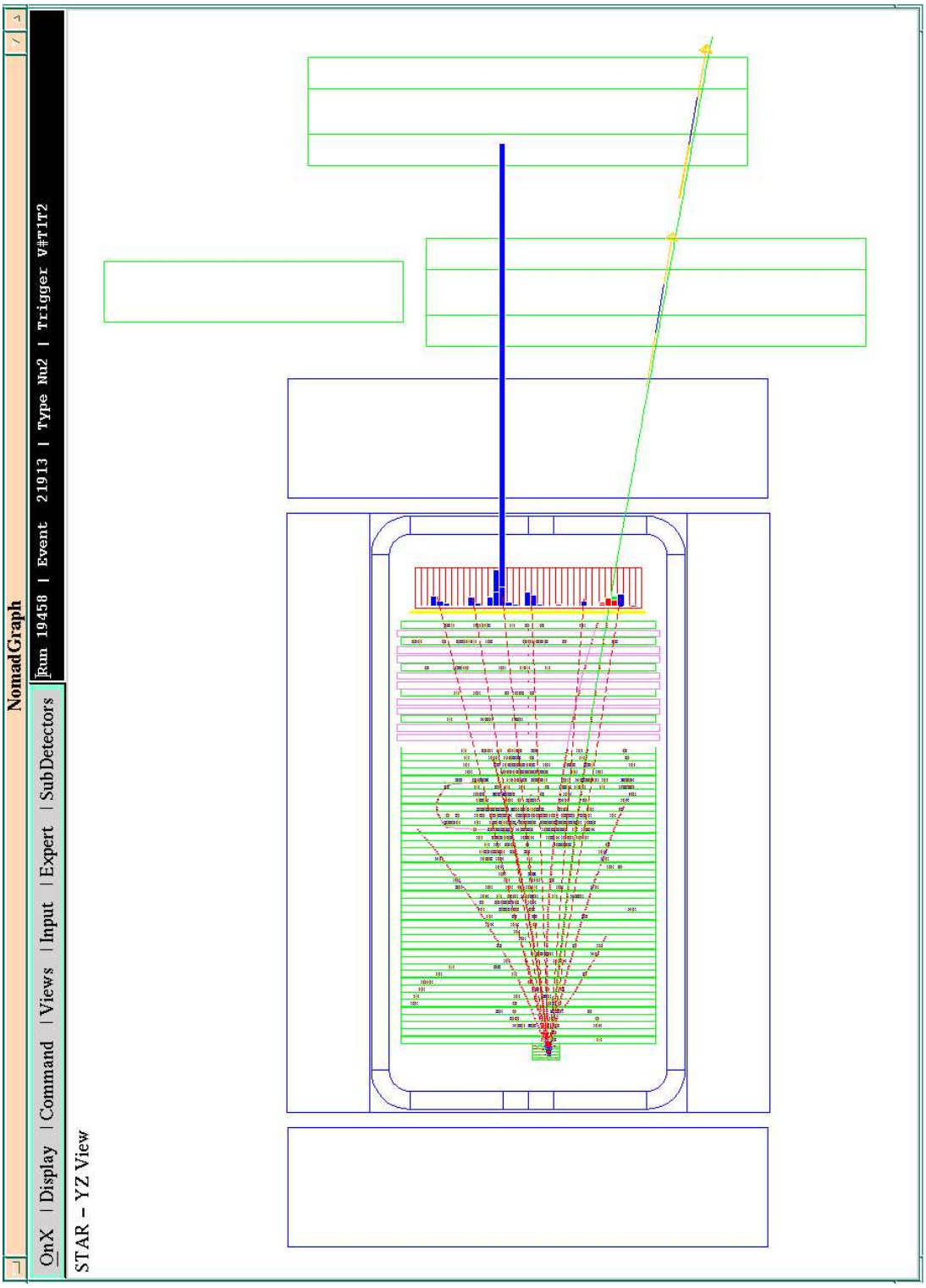

Figure 7.1: A K^0_S decay candidate from the experimental data. The whole NOMAD detector is shown.

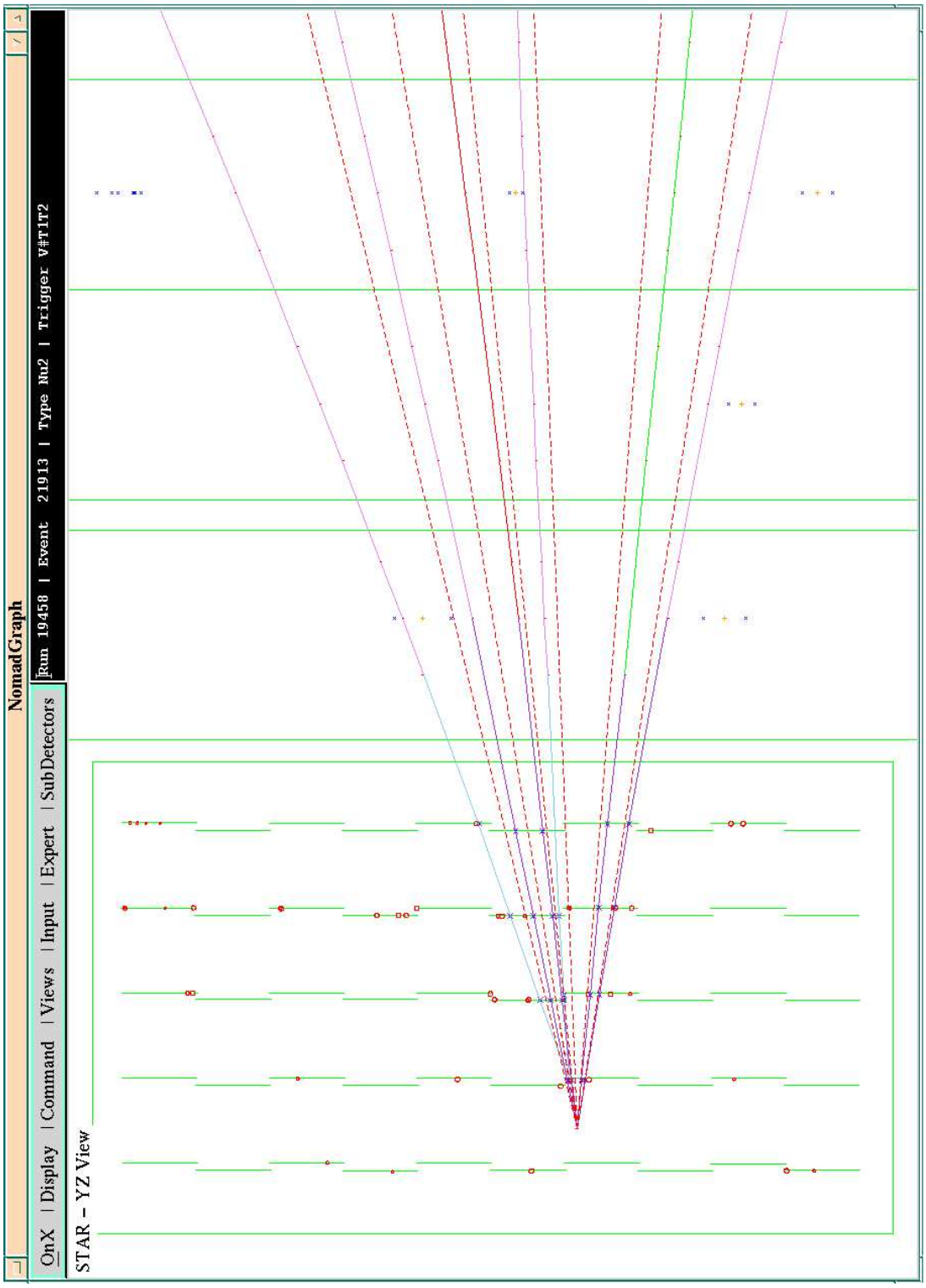

Figure 7.2: A K^0_S decay candidate from the experimental data. The whole of STAR is shown as well as some of the drift chambers.

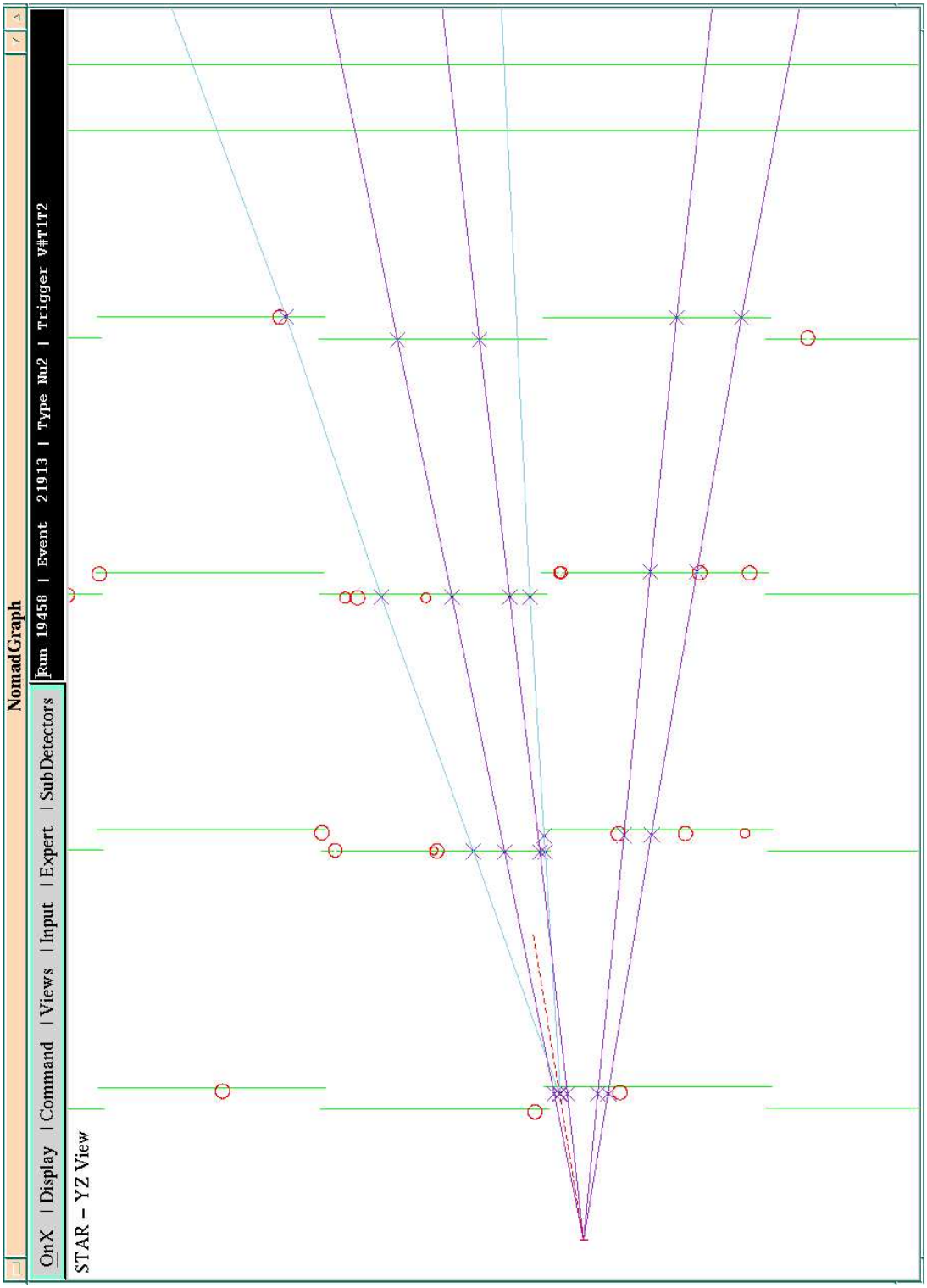

Figure 7.3: A K^0_S decay candidate from the experimental data. The primary and secondary vertices are shown as well as several layers of silicon and the start of the drift chambers.

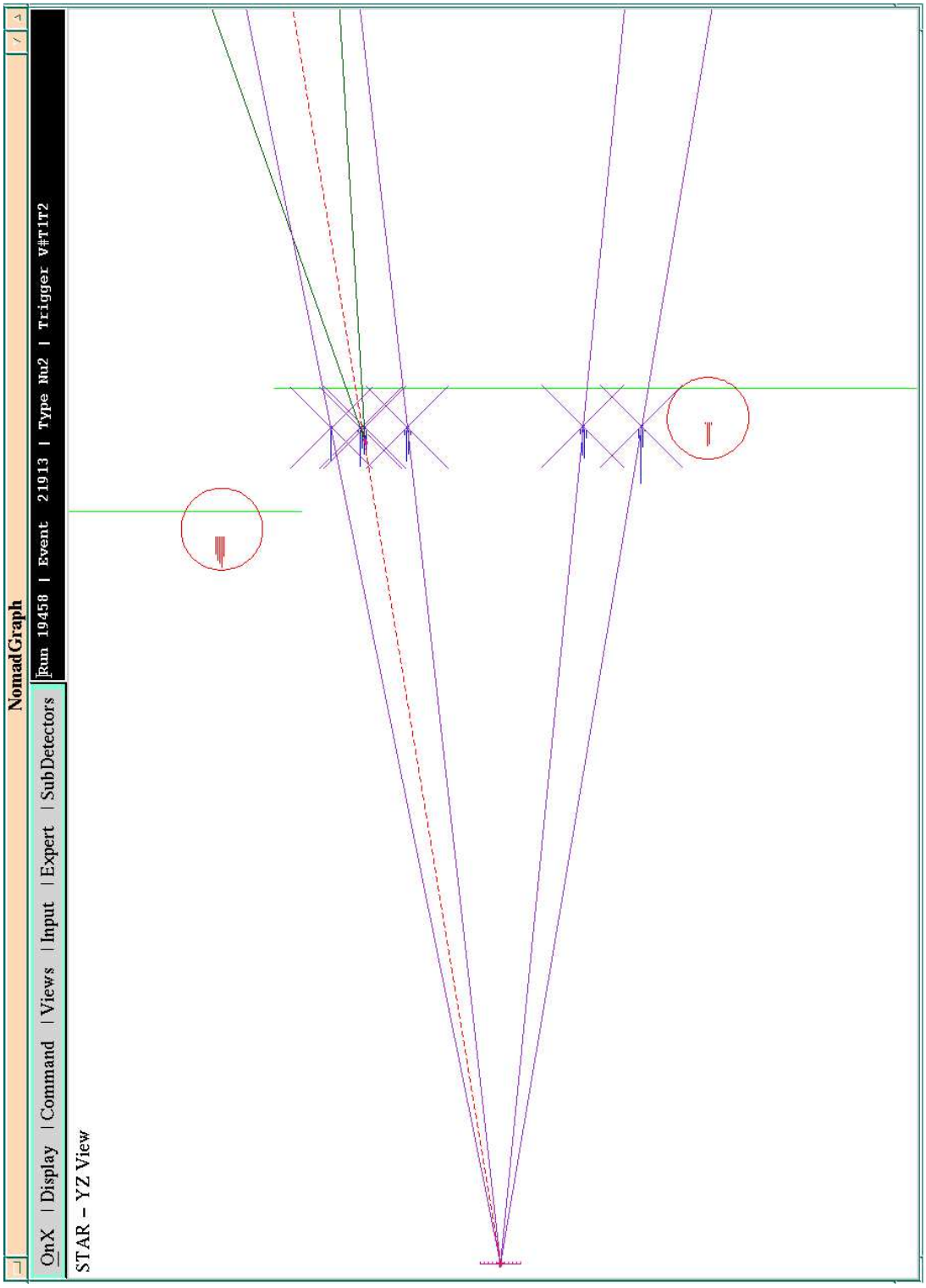

Figure 7.4: A K^0_S decay candidate from the experimental data. A highly magnified view of the primary and secondary vertices and a single silicon layer.

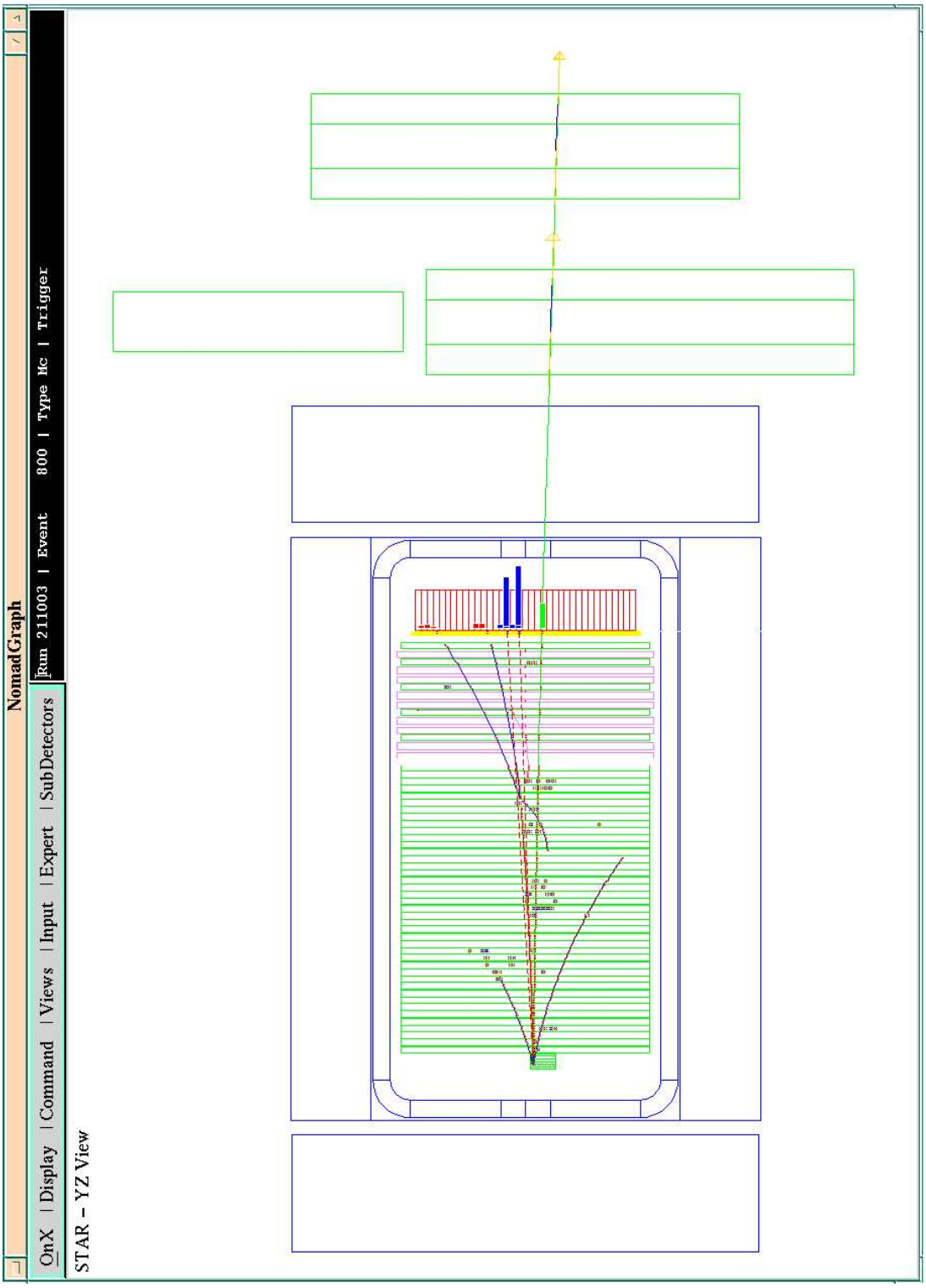

Figure 7.5: A K_S^0 decay from a ν_μ CC event in the Monte Carlo data. The whole NOMAD detector is shown.

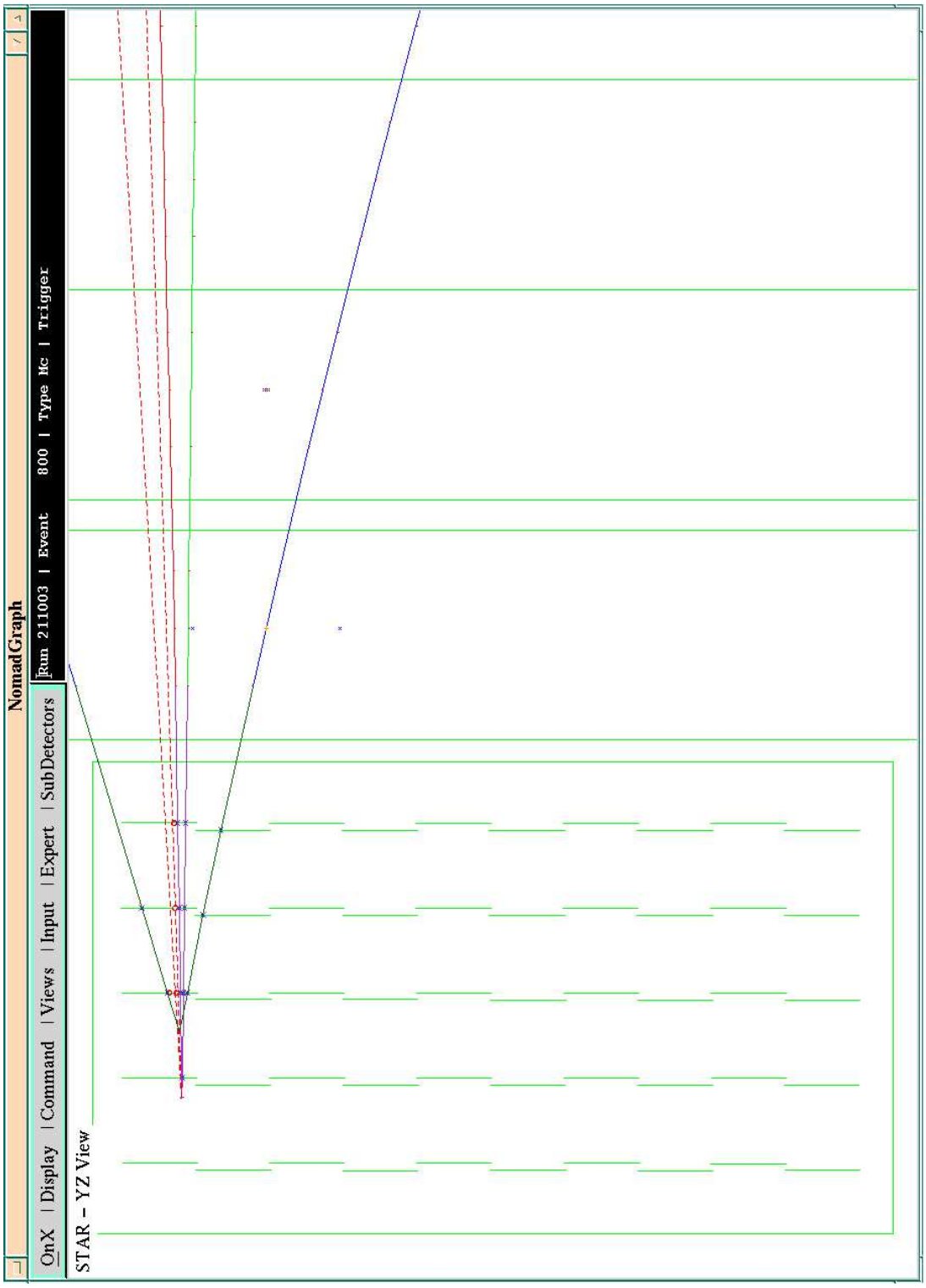

Figure 7.6: A K_S^0 decay from a ν_μ CC event in the Monte Carlo data. The whole of STAR is shown as well as some of the drift chambers.

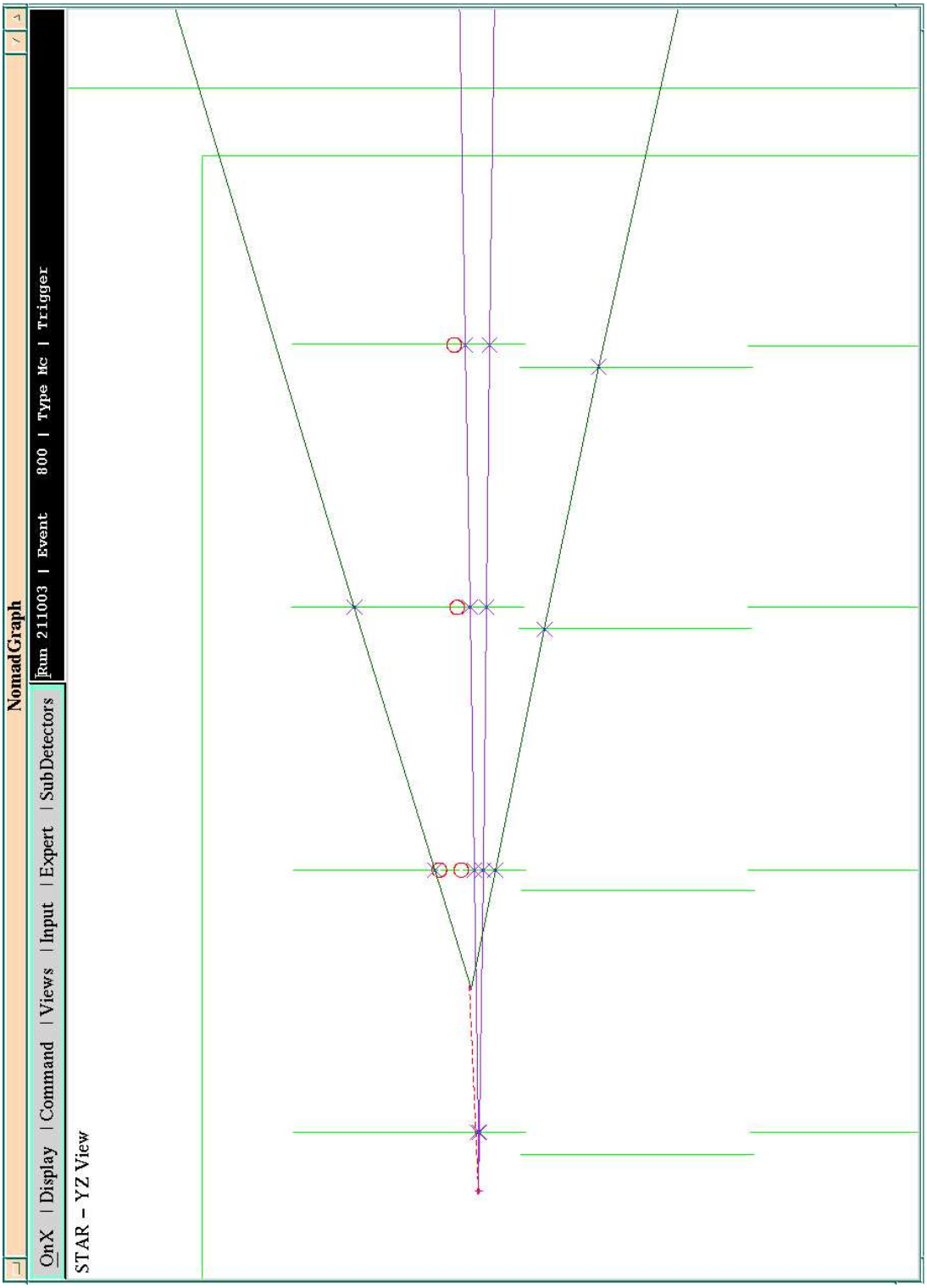

Figure 7.7: A K^0_S decay from a ν_μ CC event in the Monte Carlo data. The primary and secondary vertices are shown as well as several layers of silicon and the start of the drift chambers.

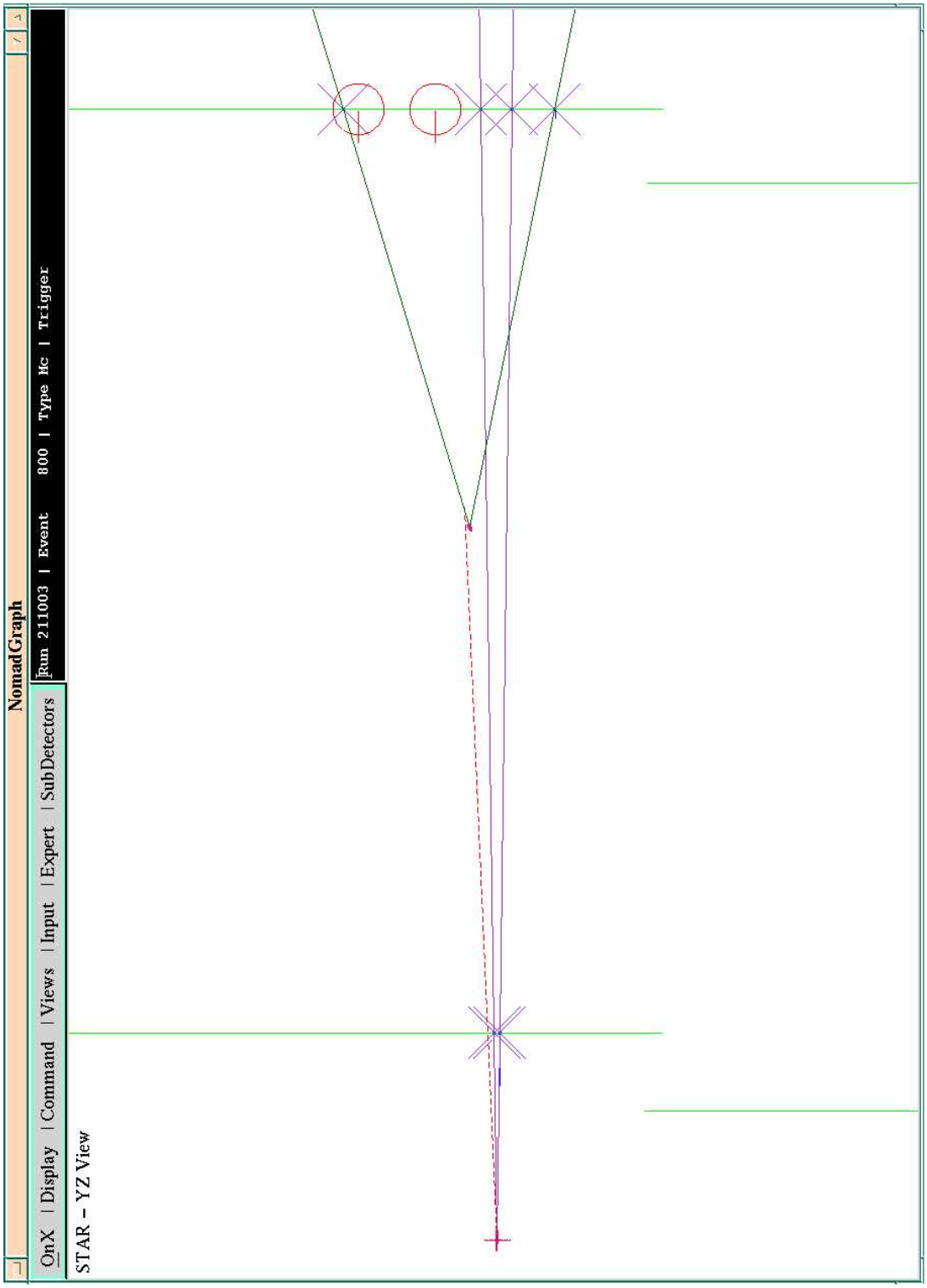

Figure 7.8: A K_S^0 decay from a ν_μ CC event in the Monte Carlo data. A highly magnified view of the primary and secondary vertices and two silicon layers.

References

[1] D.E. Groom *et al.*, "Review of particle physics", Eur. Phys. J. C 15 (2000) 1.

[2] K.V. Klapdor-Kleingrothaus, K. Zuber, "Particle astrophysics — revised edition", IOP Publ. (2000).

[3] www.slac.stanford.edu/spires/experiments/online_exp.shtml and the experiment homepages listed therein; www.hep.anl.gov/ndk/hypertext/no_acronym.

[4] B.T. Cleveland *et al.*, "Measurement of the solar electron neutrino flux with the Homestake chlorine detector", Astrophys. J. 496 (1998) 505.

[5] T.A. Kirsten, "GALLEX solar neutrino results", Prog. Part. Nucl. Phys. 40 (1998) 85.

[6] W. Hampel *et al.*, GALLEX collaboration, "GALLEX solar neutrino observations: results for GALLEX IV", Phys. Lett. B 447 (1999) 127.

[7] J.N. Abdurashitov *et al.*, "Results from SAGE (the Russian-American gallium solar neutrino experiment)", Phys. Lett. B 328 (1994) 234.

[8] Y. Fukuda *et al.*, Kamiokande collaboration, "Solar neutrino data covering solar cycle 22", Phys. Rev. Lett. 77 (1996) 1683.

[9] Y. Fukuda *et al.*, "Measurements of the solar neutrino flux from Super-Kamiokande's first 300 days", Phys. Rev. Lett. 81 (1998) 1158.

[10] J.N. Bahcall, P.I. Krastev, A.Yu. Smirnov, "Where do we stand with solar neutrino oscillations?" Phys. Rev. D 58 (1998) 096016-1.

[11] Y. Fukuda *et al.*, Super-Kamiokande collaboration, "Constraints on neutrino oscillation parameters from the measurement of day-night solar neutrino fluxes at Super-Kamiokande", Phys. Rev. Lett. 82 (1999) 1810.

[12] J. Boger *et al.*, SNO collaboration, "The Sudbury Neutrino Observatory", Nucl. Instr. and Meth. A 449 (2000) 172.

[13] Q.R. Ahmad *et al.*, SNO collaboration, "Measurement of the rate of $\nu_e + d \rightarrow p + p + e^-$ interactions produced by ^{8}B solar neutrinos at the Sudbury Neutrino Observatory", Phys. Rev. Lett. 87 (2001) 071301-1.

[14] J.N. Bahcall, M.C. Gonzalez-Garcia, C. Peña-Garay, "Global analysis of solar neutrino oscillations including SNO CC measurement", JHEP 08 (2001) 014.

[15] G. Ranucci *et al.*, Borexino collaboration, "Borexino", Nucl. Phys. B (Proc. Suppl.) 91 (2001) 58.

[16] A. Piepke for the KamLAND collaboration, "KamLAND: A reactor neutrino experiment testing the solar neutrino anomaly", Nucl. Phys. B (Proc. Suppl.) 91 (2001) 99.

[17] S. Bilenky, "Neutrino mixing", in K. Winter (ed.), "Neutrino physics — second edition", Cambridge Univ. Press (2000) 149.

[18] Y. Fukuda *et al.*, Super-Kamiokande collaboration, "Evidence for oscillation of atmospheric neutrinos", Phys. Rev. Lett. 81 (1998) 1562.

[19] M. Apollonio *et al.*, "Initial results from the CHOOZ long baseline reactor neutrino oscillation experiment", Phys. Lett. B 420 (1998) 397.

[20] M. Apollonio *et al.*, "Limits on neutrino oscillations from the CHOOZ experiment", Phys. Lett. B 466 (1999) 415.

[21] F. Boehm *et al.*, "Search for neutrino oscillations at the Palo Verde nuclear reactors", Phys. Rev. Lett. 84 (2000) 3764.

[22] F. Boehm *et al.*, "Results from the Palo Verde neutrino oscillation experiment", Phys. Rev. D 62 (2000) 072002-1.

[23] M. Abbes *et al.*, "The Bugey 3 neutrino detector", Nucl. Instr. and Meth. A 374 (1996) 164.

[24] B. Achkar *et al.*, "Search for neutrino oscillations at 15, 40 and 95 meters from a nuclear power reactor at Bugey", Nucl. Phys. B 434 (1995) 503.

[25] A. Romosan *et al.*, "High statistics search for $\nu_\mu(\overline{\nu}_\mu) \rightarrow \nu_e(\overline{\nu}_e)$ oscillations in the small mixing angle regime", Phys. Rev. Lett. 78 (1997) 2912.

[26] C. Athanassopoulos *et al.*, "The liquid scintillator neutrino detector and LAMPF neutrino source", Nucl. Instr. and Meth. A 388 (1997) 149.

[27] K. Eitel, "Compatibility analysis of the LSND evidence and the KARMEN exclusion for $\overline{\nu}_\mu \rightarrow \overline{\nu}_e$ oscillations", New J. Phys. 2 (2000) 1.1.

[28] B. Armbruster *et al.*, "New experimental limits on $\nu_e \rightarrow \nu_\tau$ oscillations in 2-ν and 3-ν mixing schemes" Phys. Rev. C 57 (1998) 3414.

[29] A.O. Bazarko for the MiniBooNE collaboration, "MiniBooNE: Status of the booster neutrino experiment", Nucl. Phys. B (Proc. Suppl.) 91 (2001) 210.

[30] E. Eskut *et al.*, CHORUS collaboration, "The CHORUS experiment to search for $\nu_\mu \rightarrow \nu_\tau$ oscillation", Nucl. Instr. and Meth. A 401 (1997) 7.

[31] E. Eskut *et al.*, CHORUS collaboration, "Search for $\nu_\mu \rightarrow \nu_\tau$ oscillation using the τ decay modes into a single charged particle", Phys. Lett. B 434 (1998) 205.

[32] S.H. Ahn *et al.*, K2K collaboration, "Detection of accelerator-produced neutrinos at a distance of 250 km", Phys. Lett. B 511 (2001) 178.

[33] S.G. Wojcicki, "Status of the MINOS experiment", Nucl. Phys. B (Proc. Suppl.) 91 (2001) 216.

[34] K. Elsener *et al.*, "The CERN neutrino beam to Gran Sasso (NGS)", CERN 98-02, INFN/AE-98-05 (1998); R. Bailey *et al.*, "The CERN neutrino beam to Gran Sasso (NGS) — addendum to report CERN 98-02, INFN/AE-98/05", CERN/SL 99-34, INFN/AE-99-05 (1999).

[35] F. Arneodo *et al.*, ICARUS collaboration, "The ICARUS experiment — a second-generation proton decay experiment and neutrino observatory at the Gran Sasso laboratory", LNGS-EXP 13/89 add. 2/01, ICARUS-TM/2001-09 (2001).

[36] M. Guler *et al.*, OPERA collaboration, "An appearance experiment to search for $\nu_\mu \leftrightarrow \nu_\tau$ oscillations in the CNGS beam — experiment proposal", CERN/SPSC 2000-028, SPSC/P318, LNGS-P25/2000 (2000); M.A. Guler *et al.*, OPERA collaboration, "Status report on the OPERA experiment", CERN/SPSC 2001-025, SPSC/M668, LNGS-EXP 30/2001 add.1/01 (2001).

[37] J. Altegoer *et al.*, NOMAD collaboration, "The NOMAD experiment at the CERN SPS", Nucl. Instr. and Meth. A 404 (1998) 96.

[38] P. Hurst, "The performance of the hadron calorimeter", NOMAD Memo 97-42 (1997).

[39] J. Altegoer *et al.*, NOMAD collaboration, "A search for $\nu_\mu \rightarrow \nu_\tau$ oscillations using the NOMAD detector", Phys. Lett. B 431 (1998) 219.

[40] P. Astier *et al.*, NOMAD collaboration, "A more sensitive search for $\nu_\mu \rightarrow \nu_\tau$ oscillations in NOMAD", Phys. Lett. B 453 (1999) 169.

[41] P. Astier *et al.*, NOMAD collaboration, "Limit on $\nu_e \rightarrow \nu_\tau$ oscillations from the NOMAD experiment", Phys. Lett. B 471 (2000) 406.

[42] P. Astier *et al.*, NOMAD collaboration, "Final NOMAD results on $\nu_\mu \rightarrow \nu_\tau$ and $\nu_e \rightarrow \nu_\tau$ oscillations including a new search for ν_τ appearance using hadronic τ decays", Nucl. Phys. B 611 (2001) 3.

[43] A. Peisert, "Silicon microstrip detectors", in F. Sauli (ed.), "Instrumentation in high energy physics", World Scientific Publ. (1992) 1.

[44] J.J. Gomez-Cadenas, J.A. Hernando, A. Bueno, "A neutrino apparatus with improved capabilities for a short baseline $\nu_\mu(\nu_e) \leftrightarrow \nu_\tau$ search", Nucl. Instr. and Meth. A 378 (1996) 196.

[45] J.J. Gomez-Cadenas, J.A. Hernando, "Search for $\nu_\mu(\nu_e) \leftrightarrow \nu_\tau$ oscillations with a detector based on a emulsion-silicon target", Nucl. Instr. and Meth. A 381 (1996) 223.

[46] P.P. Allport *et al.*, "FOXFET biassed microstrip detectors", Nucl. Instr. and Meth. A 310 (1991) 155.

[47] O. Runolfsson, "Quality assurance and testing before, during, and after construction of semiconductor tracking detectors", Nucl. Instr. and Meth. A 383 (1996) 223.

[48] R. Frühwirth, "Application of Kalman filtering to track and vertex fitting", Nucl. Instr. and Meth. A 262 (1987) 444.

[49] J. Altegoer *et al.*, "NOMAD GEANT off-line manual — version 5.12" NOMAD documentation (1996).

[50] "GEANT — detector description and simulation tool", CERN program library long writeup W5013, CERN (1994).

[51] A. Fassò, A. Ferrari, J. Ranft, P.R. Sala, "FLUKA: present status and future developments", in A. Menzione, A. Scribano (eds.), "Proceedings of the fourth international conference on calorimetry in high energy physics", La Biodola, World Scientific Publ. (1994) 493.

[52] J.-P. Meyer, A. Rubbia, "NOMAD event generator off-line manual — version 5.00", NOMAD documentation (1994).

[53] G. Ingelman, "LEPTO version 6.1 — The Lund Monte Carlo for deep inelastic lepton-nucleon scattering", in W. Buchmüller, G. Ingelman (eds.), "Physics at HERA", Hamburg, DESY (1992) 1366.

[54] T. Sjöstrand, "PYTHIA 5.7 and JETSET 7.4 physics and manual", CERN-TH.7112/93, W5035/W5044, CERN (1994).

[55] A. Cervera-Villanueva *et al.*, "Survey of the frames for STAR", NOMAD Memo 97-48 (1997).

[56] A. Cervera-Villanueva, "Alignment of the NOMAD-STAR detector", Nucl. Instr. and Meth. A 447 (2000) 100.

[57] M. Ellis, "A study of charm production by neutrinos in the NOMAD-STAR detector", Doctoral Thesis, University of Sydney (2001).

[58] S.N. Gninenko, M.M. Kirsanov, N.V. Krasnikov, V.A. Matveev, "Probing lepton flavour violation in $\nu_\mu + N \to \tau + ...$ scattering and $\mu \to \tau$ conversion on nucleons", hep-ph/0106302 (2001).

[59] K.S. McFarland, "Short-baseline opportunities and challenges at a neutrino factory", Nucl. Instr. and Meth. A 451 (2000) 218.

Abstracts of Publications I-VI

I *Performance of Long Modules of Silicon Microstrip Detectors*
This note describes the performance of modules assembled with up to 12 silicon microstrip detectors. These modules were built for the instrumented Silicon Target (STAR) that has been installed in the NOMAD spectrometer. Laboratory and test beam results are compared with model predictions. For a module of nine detectors, test beam results indicate a signal-to-noise ratio of 19, a hit-finding efficiency of 99.8 % and a spatial resolution of 6.0 μm. Laboratory measurements indicate that modules of twelve detectors exhibit a signal-to-noise ratio of the order of 16.

II *A B_4C-Silicon Target for the Detection of Neutrino Interactions*
This note describes the construction of a target for neutrino interactions composed of passive boron carbide plates interleaved with silicon microstrip detectors. The target contains four layers of passive material with a total mass of 45 kg and 600 single-sided silicon microstrip detectors with a total surface area of 1.14 m^2 distributed over five layers. It is installed in the NOMAD spectrometer at the CERN SPS neutrino beam. During the 1997 run about 8000 ν_μ charged current interactions were estimated to have occured in the target. For these events it will be possible to perform a precise measurement of both vertex and kinematical variables. This will provide invaluable experience towards the construction of a future large-scale silicon tracker for neutrino oscillation experiments.

III *Kalman Filter Tracking and Vertexing in a Silicon Detector for Neutrino Physics*
This article describes the application of Kalman filter techniques for the tracking and vertexing of particles inside the NOMAD-STAR detector, a silicon vertex detector installed in NOMAD, one of the neutrino oscillation experiments at the CERN-SPS. The use of the Kalman filter simplifies computationally the tracking and vertex procedure for NOMAD-STAR. The alignment of NOMAD-STAR is shown as an example of the application of the Kalman filter for tracking purposes. The accuracy of the method is such that one obtains alignment residuals between 9 and 12 μm. Furthermore, a preliminary measure of the impact parameter (with an RMS $\sim$ 36 μm) illustrates the vertexing capabilities of this technique.

IV *STAR Noise and Hit-Finding Efficiency*
The first part of this note describes the STAR noise. This includes descriptions of the production of the noise and the long-term behaviour of the noise. A justification for the use of day-by-day noise files is provided. The second part discusses the hit-finding efficiency, including a method for the maximisation of the hit-finding efficiency by varying the cuts used in the hit-finding on a ladder-by-ladder basis. The reasons for the differences in efficiencies are also investigated.

V *Observation of K^0_S Decays in the NOMAD Silicon TARget (STAR) Detector*
The performance of the STAR detector, installed in the NOMAD short-baseline neutrino experiment at CERN, was investigated through an analysis of K^0_S-particles. This involved selecting a sample of K^0_S-particles both produced and decaying in STAR, including decays very close to the primary vertex. The sample was then used to obtain the vertex and double vertex resolutions of the detector.

VI *A Silicon Tracker for Track Extrapolation into Nuclear Emulsions*
This paper describes the construction of a silicon tracker built to investigate how well silicon detectors can predict the position of particles in nuclear emulsions over a large area. The tracker consists of 72 single-sided silicon microstrip detectors with a total surface of 0.13 m^2 distributed over four layers, providing two x and two y coordinate measurements. The set-up was installed in a CERN PS pion beam in September 1997.